POWER DELIVERY IN SYSTEMS WITH LOSSY CABLES OR INTERCONNECTS

A Dissertation
Presented to
The Academic Faculty

By

Vinod Rajasekaran

In Partial Fulfillment
Of the Requirements for the Degree
Doctor of Philosophy
In
Electrical and Computer Engineering

Georgia Institute of Technology
November 2003

POWER DELIVERY IN SYSTEMS WITH LOSSY CABLES OR INTERCONNECTS

Approved by:

Dr. Bonnie S. Heck, Chairman

Dr. Thomas G. Habetler

Dr. David G. Taylor

Date Approved: November 24th, 2003

ACKNOWLEDGEMENT

"*Knowledge is in the end based on acknowledgement*"- Ludwig Wittgenstein

A work of this magnitude would not have been complete without the support and encouragement from various quarters. I thank my parents, sister and brother-in-law for the support and understanding they have provided and for standing by me through the vicissitudes of graduate life. Further, my extended family in the U.S. has served as an anchor for me to bridge two different cultures.

I am grateful to my advisor, Dr. Bonnie S. Heck for her guidance and vision through the course of this work. I am particularly grateful to her for providing me the motivation during those inevitable bleak periods of doctoral research and hope that it has been an enriching experience for her as it has been for me.

The members of my reading committee have freely given me their time and experience. I thank Dr. David G. Taylor and Dr. Thomas G. Habetler for their valuable suggestions and research insight. I also thank Dr. Linda M. Wills and Dr. Eric Johnson for serving on my dissertation committee.

Schlumberger, Inc. funded a significant portion of this work through the Georgia Tech Analog Consortium. I am indebted to Gary Hazen and Ramon Hernandez for their guidance and direction and to all the members of the research groups at Houston and Austin who assisted me in my work during my internships.

My time as a graduate student has been enriched by the incredibly absorbing conversations, ranging from the minute details of my research to the philosophy of life, with my fellow colleagues in the power lab. I am grateful to fellow climbers at Outdoor Recreation at Georgia Tech who have helped me take much needed time off from research. To all my other friends, faculty and staff that have helped me and influenced my time at Georgia Tech – thank you.

TABLE OF CONTENTS

LIST OF TABLES

LIST OF FIGURES

SUMMARY

Long resistive cables used in the operation of remote instrumentation impose fundamental limits on the amount of power delivered and create difficulties in voltage regulation at the remote-end (voltage at the end of the cable) with changing load conditions. This type of power delivery is used in many engineering systems such as in the operation of underwater remotely-operated vehicles, in oil drilling and mining industries, and in highly distributed systems (aircraft, submarines, and space stations, etc.). The focus of this research is to develop new approaches for power delivery in systems that have considerable voltage drops between the local and remote-ends.

Existing power conversion methods based on linear and switching regulators pose unique problems when operated at the end of long resistive cables, such as voltage jumps at startup and during load transients, startup load cycling, and restrictions on the power delivered to the loads stably. Two novel methods of power delivery based on state feedback control and parallel operation of switching and linear regulators to enhance stability and increase the power delivered at the remote-end are developed and validated experimentally. These methods do not achieve voltage regulation at the remote-end.

Fast regulation of the remote-end voltage is imperative to boost efficiency and reduce the risk of operating the loads beyond the safe operating region. Feeding back the remote-end voltage is precluded due to either the absence of communication links or large time delays in the links between the remote and local-ends. A system-level approach is developed to control the remote-end voltage for changing load conditions through the usage of a model inversion technique at the local-end along with a feedback of the local-end variables. Simplified real-time models of the transmission line cable needed for the model inversion are developed and verified experimentally. An example application of oilfield logging is used to validate the open loop model inversion control method experimentally. An algorithm for the adaptation of the cable model to changes in temperature and other environmental conditions using remote-end voltage measurements obtained through a slow telemetry link is also developed

.

CHAPTER 1

INTRODUCTION

1.1. Problem Statement

1.1.1. Power delivery in systems with lossy cables

The usage of distributed power systems is proliferating due to the increased performance demands of current electronic loads. Distributed power systems are more reliable, modular, redundant and capable of better point-of-load regulation and noise decoupling than centralized power systems leading to their increased usage in high-performance power systems [1]. Aircraft, spacecraft, ships and submarines, industrial power electronic systems and remote power equipment are some of the critical areas for application of distributed power systems [1]-[5]. These applications are usually DC power systems and often have relatively long cables from a local-end (or supply-side) in order to deliver power to remote-ends. As a result, power transmission in these types of systems often results in a significant voltage drop between the local-end and the remote-end due to the relatively high resistance in the cables. Recent trends toward all-electrical systems in place of mechanical, hydraulic and pneumatic systems are leading to increased cabling, thereby exacerbating the problem. Moreover, the growth in power-hungry electronic loads is leading to increased power requirements at the remote-ends [3], [5].

An example where this is critical is in delivering power through long resistive cables to remote equipment in the oil well industry. In this application, a single cable is used between the remote and local-ends to deliver power to the loads at the remote-end. The cables are specifically designed more for tensile strength than electrical characteristics leading to large resistances. Coupling this factor with the length of the cable (that can be of the order of thousands of feet), the resistance of the power delivery path between the local and remote-ends can be large [4]. For example in the oilfield logging industry, cables are of the order of 30,000 ft. and have a loop resistance of

approximately 600Ω. Also, the harsh environment in most of these applications where temperatures can routinely reach 200°C leads to further increase in the cable resistance [3].

The large voltage drop between the remote and the local-ends imposes fundamental limits on the amount of power delivered irrespective of the type of converters used at the remote-end. The optimal regulated remote-end voltage to deliver the maximum power at full-load is half the maximum local voltage as required by the maximum power transfer theorem. However, in many systems, it is not possible to maintain the remote-end voltage at the optimal voltage due to concerns about the high voltage insulation capability of the cables and the effect of corona and electrical noise on sensitive loads. The maintenance of the remote-end voltage at a lower than optimal level influences the distribution of power at the remote-end. With linear regulators, the losses in the system are increased due to the higher current levels required to transmit the same power while in switching converters, the stability region of the system is reduced. These topics have been addressed in the case of AC power systems for generators feeding a constant load [6]. Power delivery in the aforementioned applications differs from that of AC power systems due primarily to the non-negligible cable resistance. Though, these topics are recently being addressed [7]-[14], the general emphasis has been more on the effect of the inductances and capacitances in the system than on the resistances of the cables or losses in the system.

1.1.2. Remote end voltage control

The increased power losses in the cable necessitate high efficiency in the power conversion structure. However, the remote-end voltage is usually uncontrolled due to the assumption of negligible voltage drops between the remote and local-end. When uncontrolled, the remote-end voltage exhibits a large variation from no-load to full-load, which drastically affects the efficiency of the front-end converter. Hence, the regulation of the remote-end voltage is imperative to boost the efficiency and increase the power delivered to the loads. The regulation of the remote-end voltage for changing load conditions is not a straight-forward task. System-level approaches have been proposed in AC excitation systems to control the high-side voltage to account for reactive power

changes. The main approaches proposed such as line drop compensators [15] and link control methods [16] are effective for reactive power control and implemented by neglecting the series resistance of the line. The difficulties involved in this approach in power delivery to remote instrumentation as compared to AC power systems are high cable resistances instead of inductance or capacitance of the line, access restrictions to intermediate points along the cable, transmission line effects on control loop behavior, absence of fast dedicated communication links resulting in large transport delays in the monitoring link between the local and remote-ends.

Feedback methods based on monitoring the remote-end voltage are dependent on the speed of the monitoring link connecting the local-end with the monitors on the remote-end. In general, it is difficult to stabilize the system by the usual feedback methods when the delays involved in the monitoring link are considerable and the usage of predictive methods based on estimated models is required [17]-[19]. Feed-forward methods based on system knowledge and current and voltage monitoring at the local-end can be used to control the remote-end voltage. Model inversion concepts have been used earlier in the feed-forward control of systems where the variables to be controlled are not available for feedback [21]-[24]. The sensitivity of the feed-forward/open loop model inversion methods to changes in the system is the main drawback of these methods, though they have the advantage of being independent of the delays involved in the monitoring link.

1.2. Objective of Research

The objective of this work is to develop new approaches for power delivery in systems that have considerable voltage drops between the local and remote-ends. The primary problems in existing power delivery methods are two-fold: first, the existing remote-end power conversion methods are deficient either from stability or efficiency perspectives and, secondly, the current control methods available for regulating the remote-end voltage are ineffective due to reasons mentioned earlier.

The specific goals of the present research to alleviate the limitations of existing power delivery methods are:

- Comprehensive study of power delivery to remote instrumentation.

- Assessment of limitations of existing remote power conversion methods.
- Development of new remote power conversion methods based on state feedback control and integrated combination of switching regulator and linear regulator that are more efficient and increase the power delivered to the remote-end.
- Development of efficient and accurate transmission line models for usage in local-end control.
- Development of open and closed loop model inversion controllers for fast regulation of remote-end voltage.

1.3. Thesis Outline

A brief introduction and overview of the thesis contents has been provided in this section. To familiarize the reader with the operation of remote instrumentation, Chapter 2 provides a review of power delivery to remote instrumentation and the inherent system limitations. The current research in this area is also summarized in this chapter.

Chapter 3 presents an in-depth study of the operation of existing remote power conversion methods. Linear and switching regulators are primarily examined and their limitations are assessed. Also, previously unreported phenomena such as load cycling during startup and voltage jump phenomena at startup with the usage of switching regulators are examined in detail both from theoretical and experimental standpoints.

Chapter 4 presents the new remote power conversion methods that increase the power delivered stably to the remote-end. The new methods based on state feedback and integrated combination of linear and switching regulators are studied and verified by simulations and experimental results.

In Chapter 5, transmission line modeling methods that are essential for remote-end voltage control are developed. Problems of pre-existing modeling methods are illustrated through experimental results. A new modeling method based on two-port Y parameters is introduced and supported by numerous experimental results.

Chapter 6 presents the new remote-end voltage regulation method based on open loop model inversion control. The method is validated through simulation and experimental results for a typical oilfield logging remote instrumentation system. A closed loop model inversion method to account for variations in cable impedance due to

temperature changes is also developed and validated through simulations. This method involves the combination of open loop model inversion controller with a model update using feedback of the remote-end variables through a slow telemetry link (that is, delays involved in the monitoring link are considerable compared to the dynamics of the system).

Chapter 7 presents the conclusions and contributions of this work and provides recommendations for future work in this area.

CHAPTER 2

BACKGROUND OF POWER DELIVERY IN LOSSY SYSTEMS

For a better understanding of power delivery in remote instrumentation systems, an example application of oilfield logging is briefly discussed in this chapter. An overview of the system limitations pertaining to maximum power delivered is performed in this chapter. AC transmission necessitates the usage of a rectification or power factor correction unit at the remote-end to transform AC into DC. The influence of the capacitive and inductive rectification methods on power delivery limits is analyzed. In addition, existing work on existing work on remote power conversion methods and remote-end voltage control has been reviewed in this chapter.

2.1. An example system

A typical remote instrumentation system used in oilfield logging is shown in Figure 1. In the oilfield logging system shown, oil detection sensors at the end of the oil-well are delivered power from a local-end through a long resistive cable that is 30,000 to 40,000 ft. in length. The cables are specifically designed more for tensile strength than electrical characteristics leading to large resistances of the order of 600-800 Ω. The operation of the power delivery system is manual in nature and is controlled by an operator at the local-end either in a supply truck or oil rig. At startup, the local-end voltage is ramped up by the operator until the remote-end voltage reaches a pre-determined reference voltage. The remote-end voltage is obtained either through a slow telemetry link in the case of DC power delivery or through the dynamics of the capacitive rectification method in the case of AC power delivery. During load changes, the remote-end voltage cannot be maintained at the reference voltage until the operator gets the information through the telemetry link and then corrects for the change in the remote-end

voltage. In summary, a slow operator-controlled system is used to regulate the remote-end voltage.

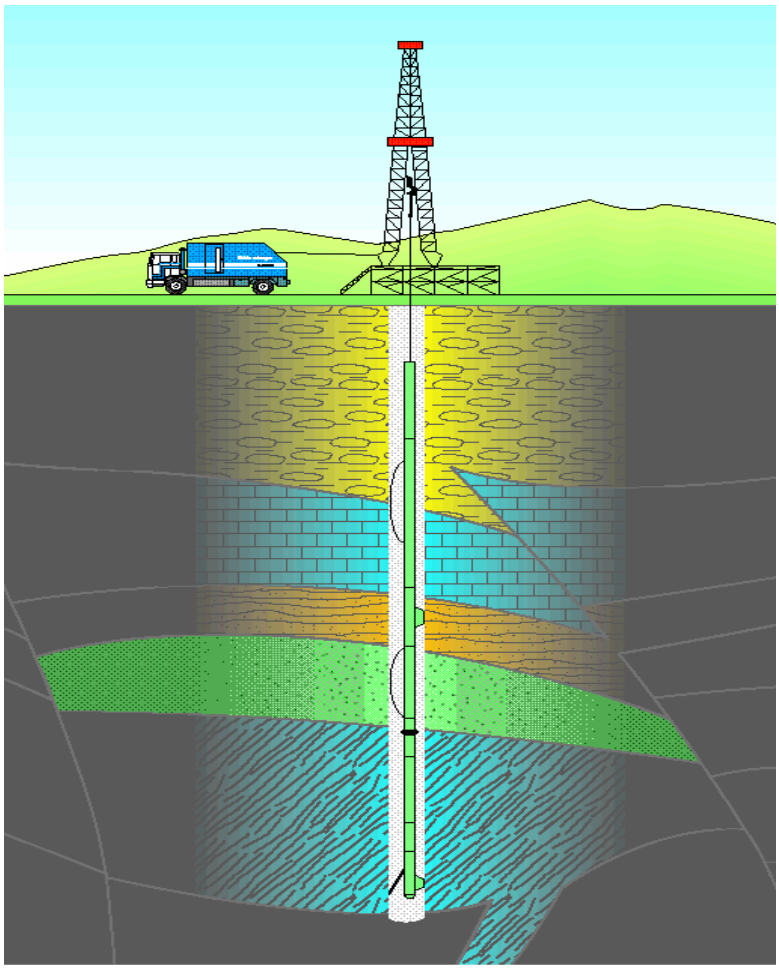

Figure 1: Oilfield logging system
Courtesy: Gary Hazen, Schlumberger, Inc.

2.2. System limitations

Consider the simplified model of a distributed power system shown in Figure 2, with the cable used for power delivery to the remote-end represented by a lumped model with resistance R_C, inductance L and capacitance C. The power transmitted to the remote-end at steady state is given by Equation (1) where V_L and I_L represent the values of the local-end voltage and current, and V_R and I_R represent the remote-end voltage and current respectively.

$$P_{remote} = V_R I_R = V_L I_R - I_R{}^2 R_C = V_L\left(\frac{V_L - V_R}{R_C}\right) - \left(\frac{V_L - V_R}{R_C}\right)^2 R_C$$
$$= \frac{V_L^2}{4R_C} - \frac{\left(\frac{V_L}{2} - V_R\right)^2}{R_C} \quad . \tag{1}$$

As can be seen from this expression, the power delivered to the remote-end is maximized when the remote-end voltage is half the local-end voltage maximum, that is, $V_R = V_{L,max}/2$ which is equivalent in a resistive load to having the load-end resistance match the cable resistance. With this substitution, the maximum power delivered to the remote-end is

$$P_{remote,\max} = \frac{V_{L,\max}^2}{4R_C} . \tag{2}$$

As was stated earlier in the introductory chapter, the remote-end voltage is regulated in order to increase the efficiency of the remote-end power converter and thus improve the maximum power delivered in a practical application. In the analysis above, the impact of the power conversion method at the remote-end on the maximum power limit has not been considered.

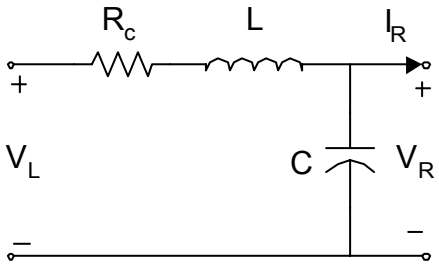

Figure 2: Simplified distribution system model

2.3. AC versus DC transmission

The analysis of system power delivery limits performed in the previous section applies only for a DC system. In actual practice, the system may be AC with a rectification or a power factor correction unit to rectify the AC remote-end voltage. Though a power factor correction unit minimizes the harmonics in the system and

behaves as an ideal resistive load, it leads to reduced power delivery as compared to a rectifier when the remote-end voltage is maintained at a preset value less than the optimal value, which is half the maximum local-end voltage. The reduced power delivery in the power factor corrected case is due to the delivery of power at the RMS (AC) voltage. Power is delivered at the peak voltage (DC) in the case of capacitive rectified systems. In the following sections, the impact of capacitive and inductive rectification methods on the maximum power delivery limits is analyzed.

2.3.1. Capacitive Rectifier Filter

In most AC power delivery systems, the loads at the remote-end are supplied through power converters that obtain their input from the output of a bridge rectifier at the remote-end. The bridge rectifier capacitive filter shown in Figure 3 introduces harmonics into the system, which can reduce the power supplied to the loads and degrade the quality of power supplied at the local-end. Further, an increase in the system harmonics leads to a poor power factor, more losses in the cable and also lesser power input at the surface, that is, the system current limit would be reached earlier.

An effective characterization of the capacitive filter rectifier is difficult due to the transcendental equations involved in its analysis. The capacitive rectifier filter can be simulated, and its DC characteristics obtained for different load ratios. An examination of the simulation results of the capacitive rectifier filter at varying loads performed by the authors of [25] shows that the load DC voltage is dependent primarily on the ratio of the cable to load resistance ratio for $\omega C R_L \geq 20$. The maximum power delivered to the remote-end for various load resistance to cable resistance ratios (at a fixed local-end voltage) is shown in Figure 4. The corresponding remote-end voltages for the same load resistance to cable resistance ratios are shown in Figure 5.

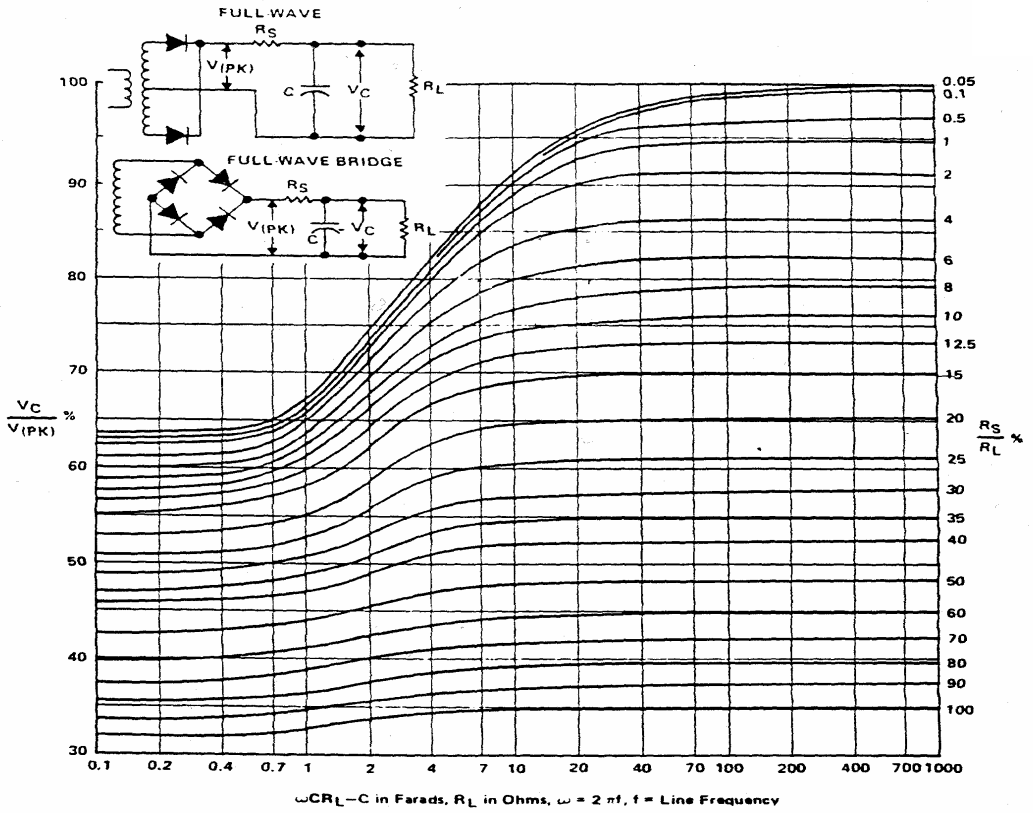

Figure 3: DC characteristics of full wave capacitive rectifiers [25]

It is clear from Figure 4 and Figure 5 that the capacitive rectification method leads to a modulation of the cable resistance to a higher value, and maximum power delivery is achieved when the load resistance to cable resistance ratio is 1.33 (as compared to 1.0 for an ideal resistive load). Also, it is clear from Figure 4 that the AC-DC conversion results in a reduction of the maximum power transferred to the load. The maximum power obtained with a capacitive rectifier is reduced by 7% to the ideal case of a resistive load. The remote-end voltage for the capacitive rectifier case is also less due to the increased effective cable resistance arising from the AC-DC conversion process.

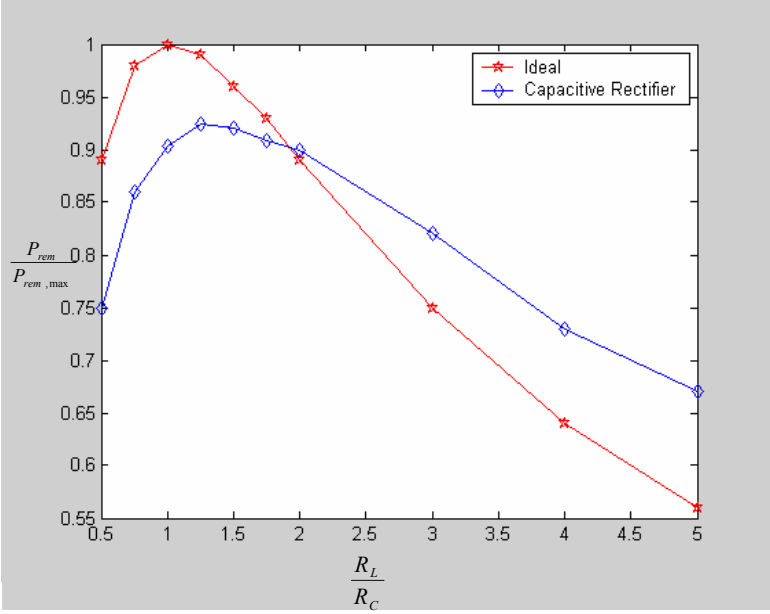

Figure 4: Comparison of power supplied to the remote-end for a capacitive rectifier and ideal resistive load (Fixed local-end voltage)

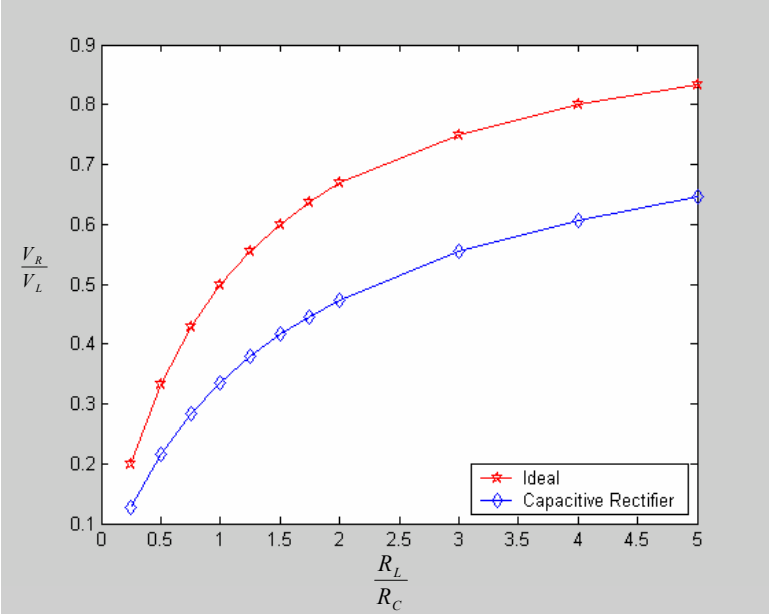

Figure 5: Comparison of remote-end voltage for a capacitive rectifier and ideal resistive load (Fixed local-end voltage)

The AC-DC capacitive rectification system shown in Figure 6 is difficult to use for predicting the system behavior such as the power delivered to the remote-end without

resorting to extensive simulations. An easier procedure involving an equivalent DC model is outlined here. The DC characteristics of the rectifier shown in Figure 3, shows that the load DC voltage is dependent entirely on the ratio of the cable to load resistance ratio when the output filter dynamics satisfy the relation: $\omega C R_L \geq 20$. With the assumption that the above relation is satisfied, a DC equivalent model could be constructed to approximate the rectification process. The DC model is represented in terms of the peak input local-end voltage, the equivalent cable resistance and the load resistance. The actual system and its equivalent are shown in Figure 6.

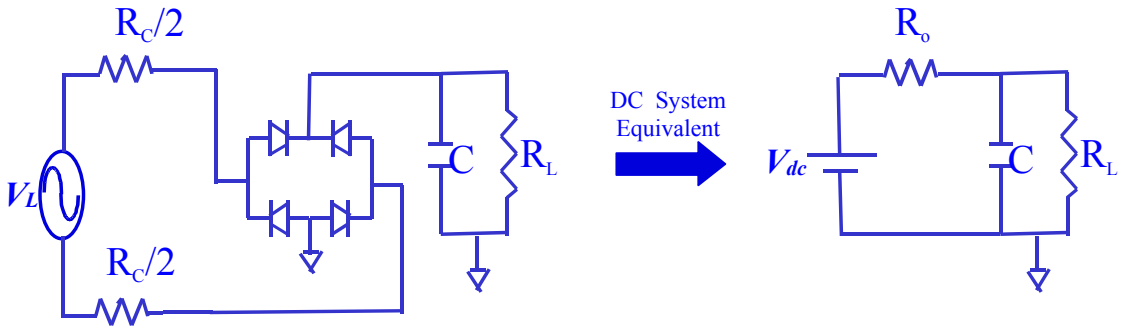

Figure 6: Actual AC-DC System and its DC equivalent

The equivalent cable resistance (R_o) is obtained from a sensitivity analysis of the DC characteristics of the rectifier. The equivalent cable resistance would be a load dependent quantity. Consider the DC equivalent shown in Figure 6. The remote-end voltage for the DC equivalent can be evaluated as:

$$V_R = V_{dc} \frac{R_L}{R_o + R_L}. \tag{3}$$

With an assumption that the DC equivalent voltage does not vary very much for incremental changes in the load resistance, the equivalent cable resistance can be estimated through a sensitivity analysis as:

$$S_{R_L}^{V_R} = \frac{\frac{\delta V_R}{V_R}}{\frac{\delta R_L}{R_L}} = \frac{R_L}{V_o}\frac{dV_R}{dR_L} = \frac{R_o}{R_o + R_L} \Rightarrow \frac{R_o}{R_c} = \frac{R_L}{R_c}\frac{S_{R_L}^{V_R}}{1 - S_{R_L}^{V_R}}. \tag{4}$$

The equivalent DC voltage V_R can be obtained from Equation (4) with the value of R_o calculated by using Equation (5). The equivalent cable resistance R_o and DC voltage V_{dc} evaluated for various load ratios are shown in Figure 7 and Figure 8 respectively. V_{dc} and R_o can be determined from Figure 7 and Figure 8 for any specific load resistance leading to an easy determination of V_R using Equation (4).

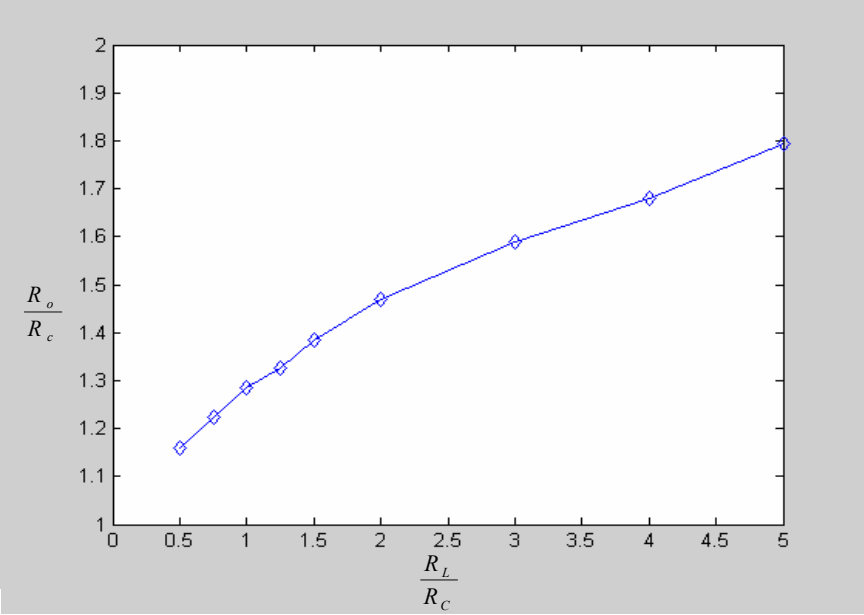

Figure 7: Variation of equivalent cable resistance with load resistance

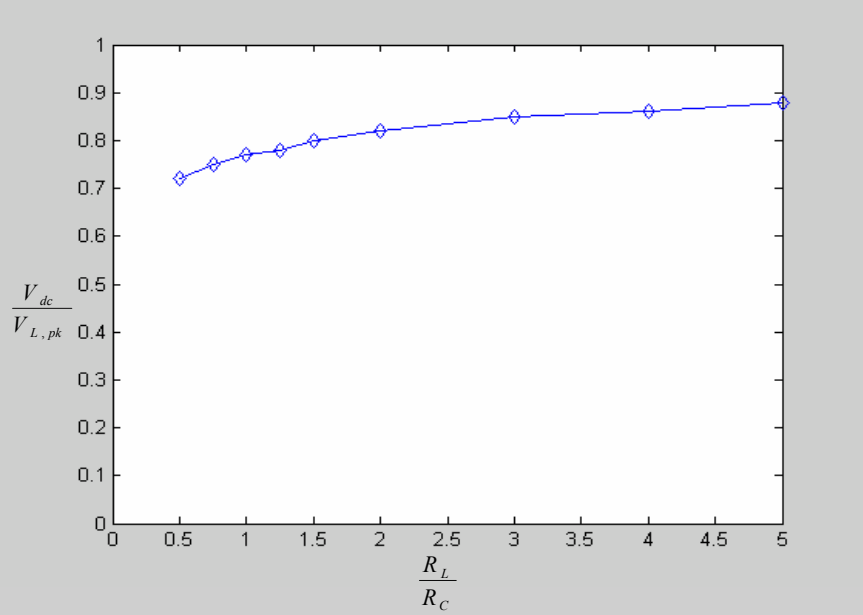

Figure 8: Variation of equivalent DC voltage with load resistance

2.3.2. Inductive Rectifier Filter

Capacitive rectifier filter require large values of load capacitors with high current loads. Further, high peak currents flow through the rectifier during normal operation of the rectifier. Alternatively, the inductive rectifier may be used to overcome these drawbacks. The impact of the inductive rectifier filter method on power delivery limits, if any, is investigated in this section. The inductive rectifier filter system is shown in Figure 9.

The inductive rectifier filter reduces both the peak and RMS values of the current and also the ripple voltage. The inductive filter ideally allows the flow of only DC current to the load and rejects all other frequencies. The inductance is chosen such that the rectifiers conduct over the entire cycle to maximize the benefits obtained with inductive rectifier filters. It can be shown that the choice of the inductance as given by Equation (5) ensures the operation of the rectifiers through the entire cycle where f_r corresponds to the ripple frequency of twice the fundamental frequency [25].

$$L = \frac{2}{3\pi f_r} R_L = \frac{R_L}{565} \tag{5}$$

For 1% ripple in the load voltage [25], the load capacitance can be calculated using Equation (6) as:

$$C = \frac{47.2}{4\pi^2 f_r^2 L} = \frac{4.69 \times 10^{-2}}{R_L} F \tag{6}$$

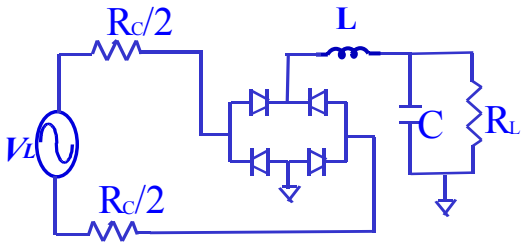

Figure 9: Inductive rectifier filter

The inductive rectifier produces an output voltage that is the DC value of the full wave rectified sine wave (as a first approximation neglecting the filtering dynamics).

$$V_O = \frac{2}{\pi} V_{R,pk} \tag{7}$$

It is important to note that when the remote-end voltage is maintained at a certain voltage, the DC output voltage of the inductive rectifier is only 0.637 times the peak of the remote-end voltage. Thus, to produce the same output voltage, the inductive rectifier filter would require a much higher input voltage than the capacitive input rectifier. The power delivered by the inductive rectifier for a fixed local-end voltage at various load ratios is shown in Figure 10. The simulations were performed with inductance and capacitance values satisfying Equations (6) and (7). For comparison, power delivered by an ideal resistive load and capacitive rectifier load are also shown.

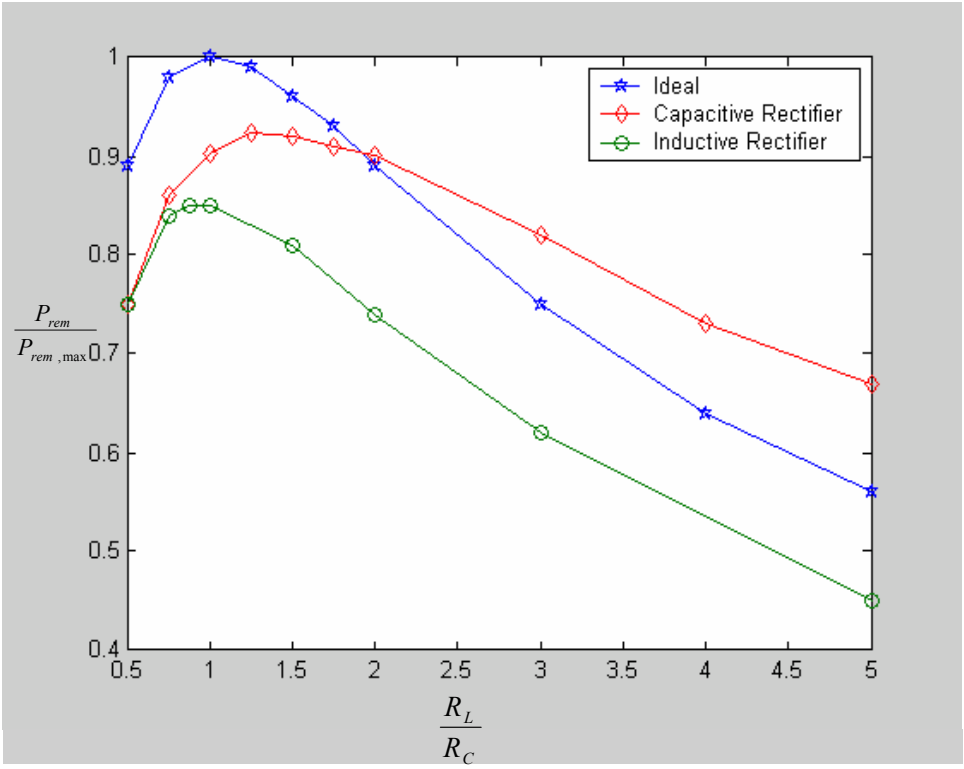

Figure 10: Comparison of power delivered by an inductive rectifier to an ideal resistive load (Fixed local-end voltage)

It can be seen that the inductive rectifier always delivers less power than the ideal resistive load or the capacitive rectifier irrespective of the loading. Further, it can also be observed that the maximum power delivered by the inductive rectifier is only 86% of the maximum power that can be delivered by an ideal load. This is worse than the capacitive rectifier, which can deliver 93% of the maximum power deliverable by an ideal load. Further, the results confirm that the maximum power transfer point has been displaced to a load resistance less than the cable resistance. While the maximum transfer of power for a capacitive rectifier occurs when the load resistance is greater than the cable resistance, the maximum power transfer for the inductive rectifier occurs with a load resistance less than the cable resistance. Hence, the inductive rectifier is inferior to the capacitive rectifier in terms of the maximum power delivered to the remote-end but has the advantage of lesser peak currents.

2.4. Remote-end power conversion methods

Due to the large resistance between the local and remote-ends, the voltage stability of the system is an important consideration that has not been addressed in detail in the literature. The maximum power limit of the system is dependent on the remote-end power conversion method. Since most large power systems are AC, most works in the literature are related to AC networks (refer to [6] for citations). In direct contrast to AC power systems where the line inductances and capacitances play a major role in the stability of the system, remote instrumentation system limits are constrained by the cable resistance. Though the underlying causes are different, the phenomenon of voltage collapse and sags is similar in both large-scale AC systems and remote instrumentation systems.

Switching regulators pose unique problems when operated at the end of long resistive cables due to their constant power load behavior and high efficiency. The interaction of switching regulators with input filters has been studied for a long time and occurs due to the interaction of the output impedance of the filter with the input impedance of the converter [9],[10]. In most cases, the interaction occurs around the crossover frequency of the voltage and current loops. In the case of power delivery to remote instrumentation, the cable resistance (which can be treated as an input filter to the remote-end power converter) dominates the other passive elements and thus leads to instability under certain conditions. Since, the cable is resistive, the instability translates into restrictions on the maximum power that can be delivered stably and is not altered by the dynamics of the inductors and capacitors in the circuit.

Recent works on undersea and spacecraft power systems have sought to address this issue of voltage instability in the operation of constant power loads (switching converters) at the end of long resistive cables [11]- [14]. In [12], a stability evaluation is performed for switching converters supplied from a highly resistive source, but the general emphasis of the paper was on constraining the source resistance and analyzing the interaction due to the filter elements. A good discussion of the stability limits for remote instrumentation systems is provided in [14]. In these systems, maximum power delivery occurs when the load resistance is matched to the cable resistance (assuming that

the transmission line can be approximated by a resistance) i.e. the remote-end voltage is half the local-end voltage [14]. In practical situations, the remote-end voltage may be constrained to a certain maximum value due to noise, corona discharge and other mitigating factors such as input voltage regulation range and high voltage electronics at significantly high temperatures [4]. In such cases, the maximum power delivery limit of a switching converter operated at the end of a long cable is constrained by the maximum remote-end voltage and not by the local-end voltage. The implications of those limits on the design of the remote-end power converter and remote instrumentation system have not been addressed in the literature. Further, the operation of remote-end power converters at the end of long resistive cables also contributes to diverse phenomena such as remote-end voltage jumps and load cycling at startup. These phenomena have previously not been reported in the literature. In Chapter 3, existing remote power conversion methods are reviewed and these unreported phenomena are discussed in detail.

2.5. Remote-end voltage control

The previous sections dealt with a brief background of power delivery to remote instrumentation and review of existing work on remote power conversion methods. In all of these methods, it is evident that the remote-end voltage cannot be maintained during load changes except by controlling the local-end voltage. The remote-end voltage, if uncontrolled, exhibits a large variation during load changes and system components need to be over-designed, thus compromising the efficiency. Therefore, it becomes important to not only consider the remote-end power distribution but also use a global, system-level approach in regulating the remote-end voltage.

For illustrative purposes, consider a simplified system with a power converter at the remote-end (treated as a constant power load *P*) and the cable represented as a simple resistance R_C of 600 Ω (though in actuality it is a transmission line). Consider the case when the system is operating at 150 W and a nominal remote-end voltage of 300 V. The corresponding local-end voltage is 600 V and the system is at the maximum power point (as can be inferred using Equation (2): $P_{remote,\max} = \frac{V_{L,\max}^2}{4R_C} = 150$ W). When the load at the

remote-end now switches off and goes into the low power mode of 5 W, the remote-end voltage will rise to almost 600 V as the drop across the cable is almost negligible now. In order to maintain the remote-end voltage of 300 V, the local-end voltage must be decreased to a little over 300 V.

As can be seen from the above example, the power converter at the remote-end would need to be rated for twice the nominal voltage to accommodate full power to zero power transitions. With such a wide range of operation, the efficiency of the converter is an issue; also, the increased device stresses lead to reliability concerns. In applications such as the oilfield logging industry, high temperatures reduce the safe operating regions of semiconductor devices so that it is imperative to reduce device stresses due to load changes. It is clear now that these issues would be moot if we can control the local-end voltage to keep a constant remote-end voltage in a short period of time.

System-level approaches have been proposed in AC excitation systems to regulate the high-side voltage to account for reactive power changes. The main approaches proposed such as line drop compensators [15] and link control methods [16] are effective for reactive power control and implemented by neglecting the series resistance of the line. There are many constraints and difficulties involved in this approach in power delivery to remote instrumentation as compared to AC systems, such as high cable resistance, access restrictions to intermediate points along the cable, transmission line effects on control loop behavior, absence of fast dedicated communication links, large transport delays in the monitoring link between the local and remote-ends, system model characterization etc. In the following sections, prior work on feedback and feed-forward based methods is reviewed.

2.5.1. Feedback methodologies

Feedback methods based on voltage and current monitoring at the remote-end can be used to maintain the remote-end voltage constant if a monitoring link is present and the time delays involved are small compared to the system dynamics. Consider the block diagram of a simple feedback method as shown in Figure 11. The feedback controller could be as simple as a PI controller for systems with negligible transmission line effects or much more complicated in systems with transmission line effects in the frequencies of

interest. When the delays involved in the monitoring link are not negligible compared to the system dynamics, the controllability of the system is difficult [17]. The maximum possible bandwidth of a system is influenced by the time delays involved in the feedback loop [18]-[19].

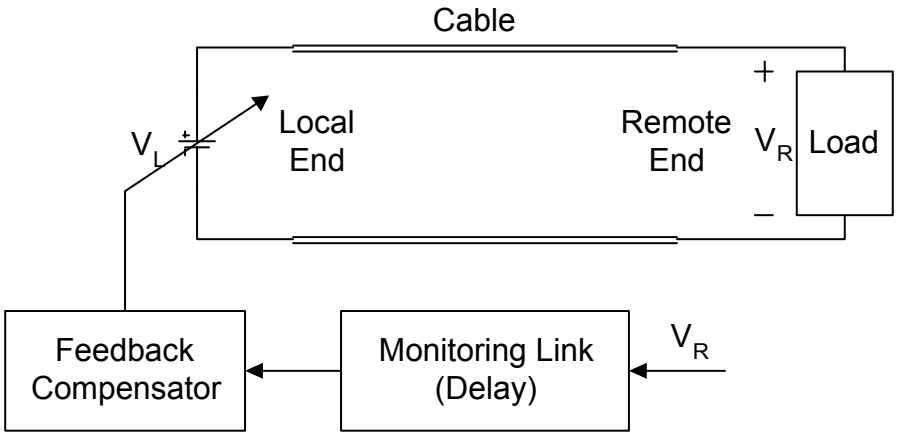

Figure 11: Feedback system approach

In practice, data might be transmitted along the same power lines or in the same cable bundle in most of the applications with long cables. The size of the power and data line cables might be determined in such cases to reduce interference and cross-talk in the data lines contributing to high cable resistances and large transport delays [3]. Feedback approaches in the case of long delays lead to stability problems due to the transport delay time. This may be remedied by modifying the controller, generally to include a system model (in this application, this would require knowledge of the characteristics of the cable). Model predictive approaches such as Smith predictors have been proposed in controlling systems with long time delays [17]-[20]. In practice, the choice of a particular model predictive approach is not intuitive and a trial-and-error approach may be required in the choice of a particular model predictor. Further, in some applications, a monitoring link may not be present and the only recourse would be to consider feed-forward approaches discussed in the next section.

2.5.2. Feed-forward methodologies

Feed-forward approaches based on regulating the remote-end voltage depending on the local-end current are highly useful in the absence of a monitoring link or long time delays. Feed-forward methods need complete knowledge of the system characteristics since the local-end voltage is pre-compensated to account for the voltage drop in the cable to maintain the remote-end voltage constant. Since they are dependent only on the system variables at the local-end, the system compensation is fast and is independent of the monitoring link. Feed-forward *line drop compensators* have been proposed in the high side voltage regulation of AC power systems to control the flow of reactive power.

The operation of feed-forward control methods can be better understood from a control theorist perspective using *model inversion* [21]-[24]. Since the remote-end state variables are not readily available to control the system (or are available only after a long time delay), a model of the cable can be used to synthesize the solution by inverting the system. This method presupposes a complete knowledge of the system and a bounded input-output stable problem formulation.

The feed-forward case is illustrated here for the simple case of a system with a purely resistive cable feeding the remote loads. In this case, the local-end voltage can be controlled by a simple feed-forward control law given by Equation (8) where V_L and I_L refer to the local-end voltage and current, R_C to the cable resistance, $V_{R,ref}$ to the remote-end voltage reference and ω_p to the pole introduced in the feed-forward path. The control law is based on feeding back the cable voltage drop (by sensing the local-end current and knowledge of the cable resistance) and computing the appropriate local-end voltage for a particular reference remote-end voltage. The pole is introduced in the feed-forward path to restrict the bandwidth of the system and prevent high frequency oscillations.

$$V_L = V_{R,ref} + \frac{I_L R_C}{1 + \frac{s}{\omega_p}} \tag{8}$$

SPICE simulation results are used to illustrate the effectiveness of this approach when the system parameters are known accurately. The cable is assumed to be a resistance of 600 Ω and the load is switched between 650 Ω and 3000 Ω. The remote-end voltage is maintained at 200 V by the feed-forward controller through the adjustment of

the local-end voltage with the bandwidth of the system limited to 1 kHz. Further, it has been assumed that the resistance of the cable is available to the feed-forward controller. The local-end voltage rises from approximately 220 V at a light load of 3000 Ω to almost 400 V with a load of 650 Ω almost matched to the cable resistance of 600 Ω. Note that the terminology of light and heavy loads refers to remote-end load currents that in turn correspond to high and low remote-end load resistances respectively. The results of the SPICE simulation are shown in Figure 12. Note that there is some transient behavior in the remote-end voltage as the load is switched, but it then is regulated close to 200 V.

Effective control of the feed-forward method is dependent on the modeling of the transmission line characteristics of the cable. A basic feed-forward method using the short-circuit impedance of the transmission line was reported in [26]. Though there are many transmission line models that deal with simulation of transients, the usage of a model in a feedback/feed-forward loop has not been undertaken [27]-[33]. Development of models that can be used for transient simulation of the system as well as for use in the implementation of the feed-forward controller is discussed in detail in Chapter 5.

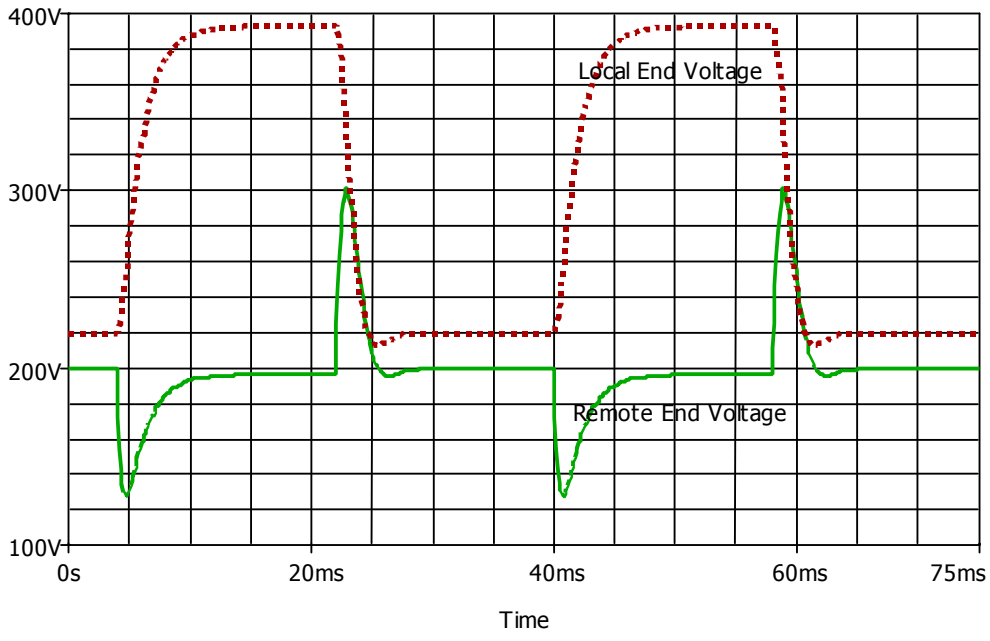

Figure 12: Feed-forward system approach simulation results

2.6. Conclusions

This chapter has reviewed the fundamentals of power delivery in remote instrumentation. The impact of remote-end power conversion methods on the power delivery limits was discussed and prior work on these methods was reviewed. Finally, the need for remote-end voltage control and the feedback and feed-forward methods currently used were discussed. In Chapter 3 the existing remote-end power conversion methods will be studied and analyzed from both theoretical and experimental fronts to assess their limitations.

CHAPTER 3

ANALYSIS OF EXISTING REMOTE POWER DELIVERY METHODS

In this chapter, the impact of the remote power conversion method on the power delivery limits is studied. The operation of the two main remote power conversion methods, namely linear and switching converters is studied in detail and previously unreported phenomena such as load cycling and voltage jumps at startup with switching regulators are reported. The drawbacks of other commonly used remote power conversion methods are also assessed in this chapter.

3.1. Linear Regulators

The series linear regulator is the most common way of transferring power from the remote-end to the loads at lower regulated voltages using a pass element. The usage of linear regulators at high remote-end voltages necessitates the usage of DC-DC step-down converters or DC-AC inverters followed by rectification stages, resulting in disadvantages of the large resulting size and low efficiency of the converters. The simplicity, low electromagnetic interference (EMI), and stability of this method are its advantages over the switching regulators. The operation of linear regulators at the end of a long cable between the local and remote-end will be illustrated in the following sections.

3.1.1. Startup Effects

Consider the highly simplified model shown in Figure 13 of a linear regulator supplied by a DC source at the end of a long cable. The cable has been represented by an equivalent R-C lumped model. The linear regulator acts like a resistive load to the system at start-up. When the local-end voltage is increased, the load at the remote-end is equivalent to the resistance of the load at power-up (assuming that the drop across the

pass element can be neglected). Once the linear regulator has enough input voltage (greater than the output voltage) to start regulating, the output current is maintained constant and the linear regulator behaves as a current sink. For increases in the load, the remote-end voltage drops and the local-end voltage would need to be increased to maintain the remote-end voltage. The dropout voltage of the linear regulator for the maximum load condition determines the minimum remote-end voltage that must be maintained for the system to be regulating.

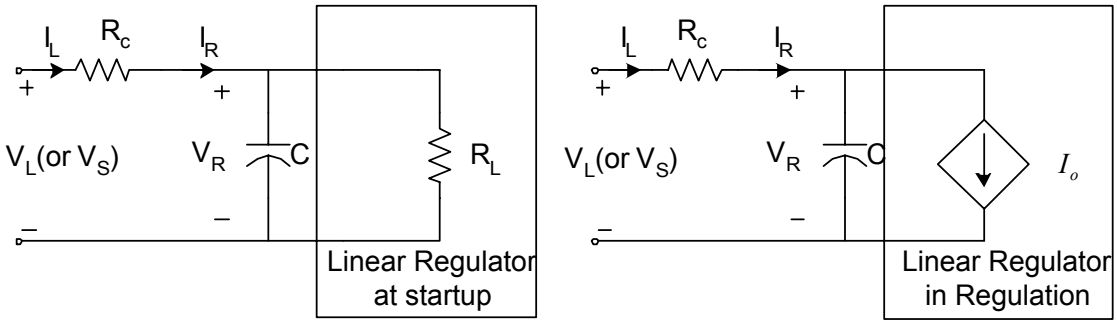

(a) (b)

Figure 13(a): Linear regulator in unregulated mode; (b): in regulated mode

The load curves for the operation of the linear regulator system with a cable resistance of 800Ω, nominal remote-end voltage of 330 V, and a regulating minimum voltage of 250 V at the remote-end are shown in Figure 14. The system operating point is determined by the intersection of the regulator load line and the system load line (which is dependent on the local-end voltage and the cable resistance). It can be seen that for each particular load current requirement (below the system capacity) there exists a unique local-end voltage, which can maintain the remote-end voltage.

Figure 15 shows the variation in remote-end voltage with local-end voltage (the only variable being controlled during startup) for varying load ratios. For quick reference, the cases of the infinite load (at 45°), matched load (at 60°) have also been shown along with the system voltage limit of 1556V. The remote-end voltage increases with increasing local-end voltage with the dynamics dependent on the load resistance until the regulator gets into the regulation mode. In this region, the linear regulator acts as a

current source. Hence for any increases of the local-end voltage beyond the voltage regulation point, the remote-end voltage increases by the same amount maintaining the output voltage constant (that is, the regulator behaves now as a constant current source). The system startup is hence very smooth for this type of regulator.

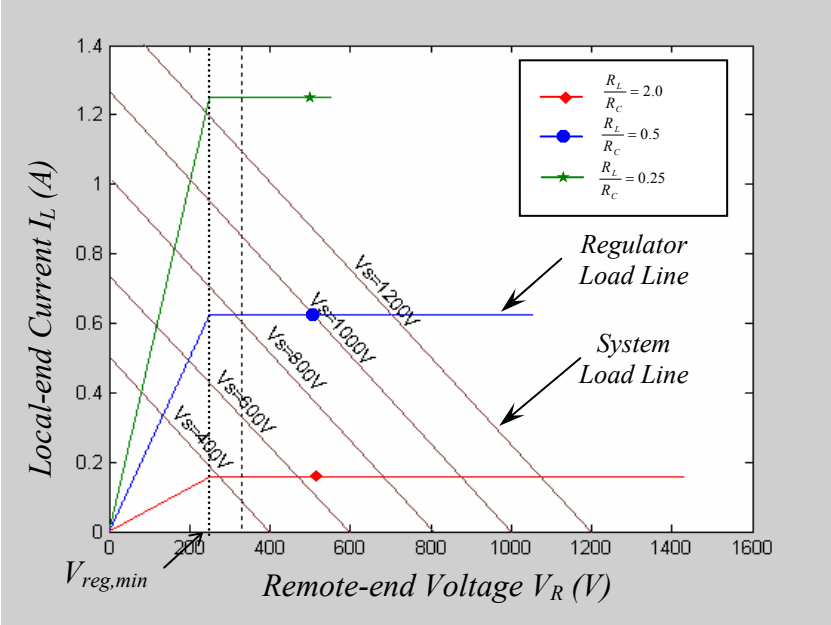

Figure 14: V-I characteristics of linear regulator

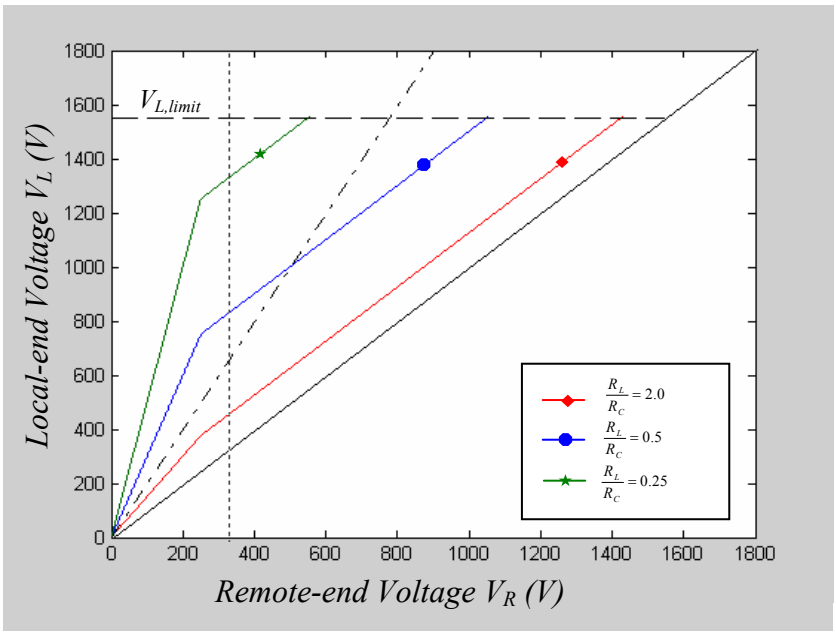

Figure 15: Variation of remote-end voltage with local-end voltage

3.1.2. Load cycling effects

In practice, the loads are turned on only after the remote-end voltage has increased beyond a certain knee voltage during startup to reduce the risk of damaging the loads. This can in turn cause oscillations in the system during startup irrespective of the type of converter being used at the remote-end and is being reported for the first time here. Consider the case of loads being turned on when the remote-end voltage crosses 100 V and turned off when the voltage goes below 75 V with the load to cable resistance ratio equal to one (a hysteresis window of 25V has been assumed for clarity in plots though it may be smaller in practice). The system behavior is shown in Figure 16 and Figure 17. The remote-end voltage keeps increasing with the local-end voltage until it just crosses 100 V at which point the load turns itself on. But for sustaining the load, the remote-end voltage would need to be at 150 V. Since the local-end voltage is only at 100 V, the remote-end voltage would fall to 75 V when the load again turns itself off. The load turnoff leads to an increase in the remote-end voltage and the load cycles on and off. This behavior continues until the local-end voltage is increased to 150V, beyond which, the remote-end voltage continues along the resistive curve defined by the load resistance.

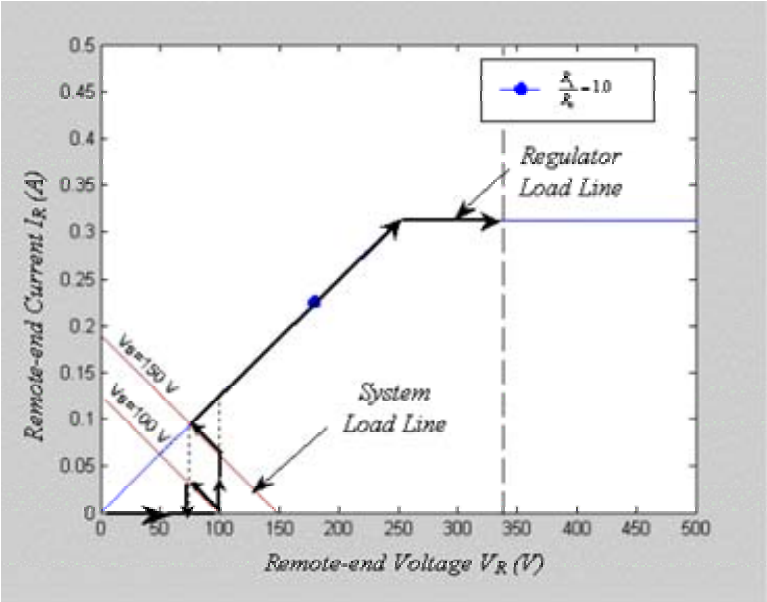

Figure 16: Startup load cycling (Remote-end)

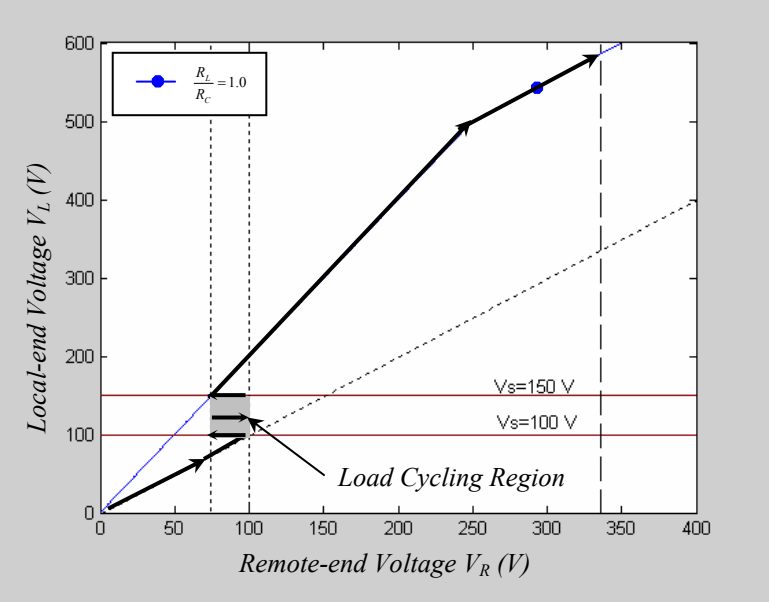

Figure 17: Startup load cycling (Local-end)

3.1.3. Impact of load changes

The remote-end voltage is normally controlled by manual adjustment of the local-end voltage. Any abrupt load changes can lead to large changes in the remote-end voltage. Consider the example of a gradual load change in the system from 400Ω (272 W nominally) to 1600Ω (68W nominally) as illustrated in Figure 18 and Figure 19. The system operates at a local-end voltage of 800 V to maintain 272 W output at the remote-end nominal voltage of 330 V. If the load now starts operating in the low power mode and reduces its power intake to 68 W, the remote-end voltage will rise to almost 660 V. The remote-end voltage would need to be brought back to 330 V nominal by the operator who must reduce the local-end voltage to 450 V.

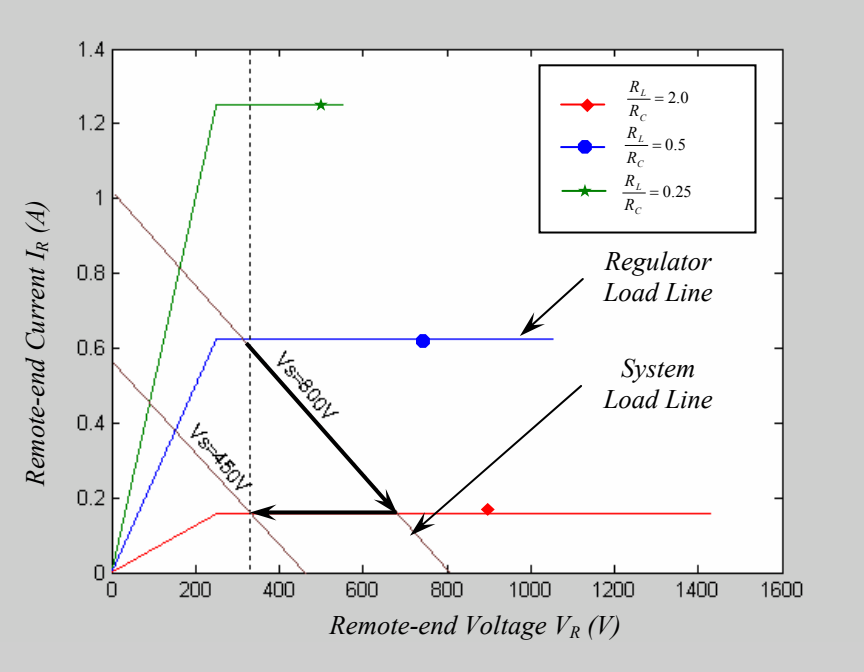

Figure 18: Load change transient behavior (Remote-end)

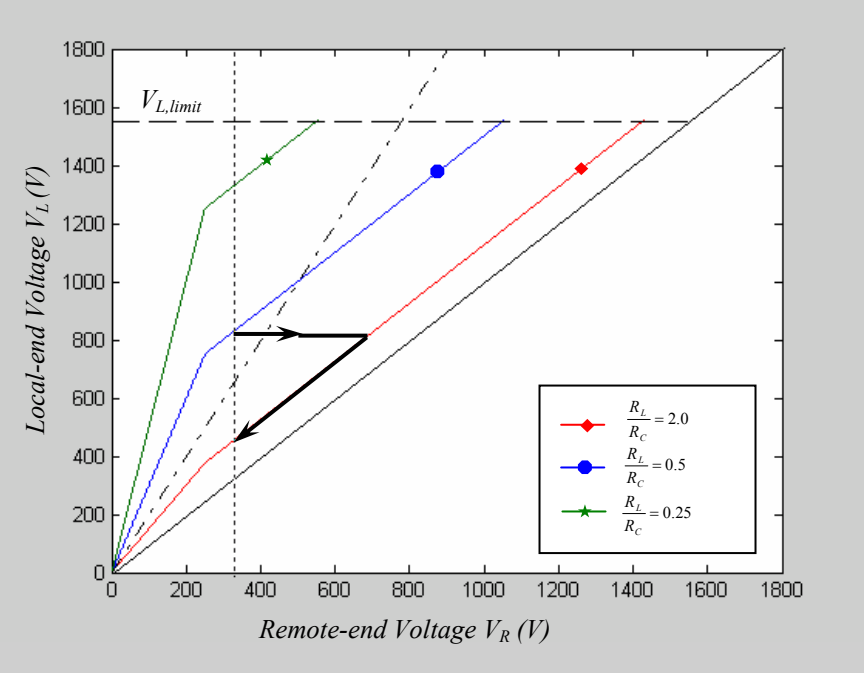

Figure 19: Load change transient behavior (Local-end)

Though the remote-end voltage is operated nominally at 330V, all components at the remote-end need to be rated for the maximum local-end voltage. Further, note that if the load power increases, the load would get out of regulation and the local-end voltage would need to be increased before it gets back into regulation. The above analysis was performed with the assumption of ideal dynamics. In practice, filter dynamics and other passive elements in the system also influence the actual dynamics. The load change transients cannot be avoided unless the impending connection or disconnection of loads is known apriori at the local-end and the local-end voltage can be controlled to reduce the remote-end voltage transients.

3.2. Switching regulators

Switching regulators, in contrast to linear regulators, are highly efficient due to the usage of energy storage elements such as inductors and capacitors. However, switching regulators suffer from disadvantages such as high EMI due to the switching action and operation in unstable modes. Few references exist in the current literature on the operation of switching regulators at the end of long resistive cables; those that do exist deal mainly with the influence of the L-C elements of the cable or source impedance on the stability of the system [9]-[11]. Similar results in the operation of constant power loads with current limited sources and solar arrays have been reported in the literature [34]. Though a good discussion of the stability limits for remote instrumentation systems is provided in [12]-[14], the implications of these limits on the operation of the system have not been assessed. For example, the jump phenomenon during startup in the operation of the switching regulator at the end of a long cable is not considered in these references. This phenomenon is analyzed for the first time in this thesis.

The switching regulator is a nonlinear load and has different characteristics in regulated and unregulated modes. During start-up, the switching regulator is out of regulation and supplies the entire input power to the load with no energy storage; hence, it has a resistive characteristic governed by the load resistance during the start-up process. The switching regulator resembles a constant power load when in regulation. The equivalent systems during these two modes are shown in Figure 20 where R_{start} refers to the resistance seen at the input of the regulator in the unregulated mode (usually occurs

during start-up) and *P* refers to the power supplied in the regulated mode. For simplicity, the local-end voltage has been assumed to be DC and the cable has been represented by an equivalent R-C lumped model.

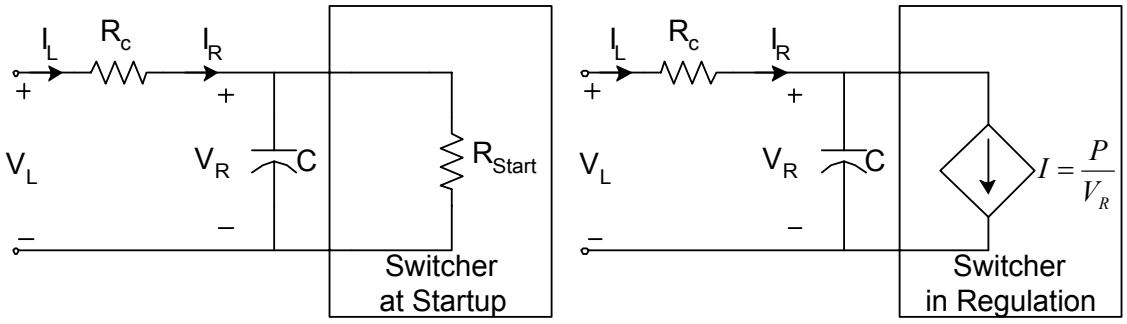

(a) (b)

Figure 20(a): Switcher in unregulated mode; (b): Switcher in regulated mode

The intersection of the system load line with the switching regulator characteristic determines the equilibrium point of the system. During startup, when the local-end voltage (V_L or V_S) is increased, the system can have one, two or three equilibrium points depending on the mode of operation as is evident from Figure 21. Since the constant power load maintains a constant *vi* product, the interchanging of *v* and *i* does not alter the situation. Intuitively it can be seen that the constant power load system will have two equilibrium points one at high remote-end voltage (and low load current) and another at lower remote-end voltage (and higher load current). Further, the startup resistance can influence the behavior of the system and determine whether the system is regulating for a particular local-end voltage i.e. the startup resistance determines whether the constant power behavior is reachable for a particular local-end voltage. It can be seen multiple number of cases can arise depending on the start-up resistance and the power demanded by the load.

The dynamics of the system can be represented by a first order differential equation governing the remote-end voltage where $g(v_R)$ represents the current drawn by the switcher during the different modes as:

$$\frac{dv_R}{dt} = \frac{1}{C}\left(\frac{V_L - v_R}{R_C} - g(v_R)\right) \tag{9}$$

The current drawn by the switcher for particular starting resistances R_{start} and regulator power P for a cable of resistance 800 Ω is shown in Figure 21. The intersection of the system load lines with the regulator curves defines the equilibrium points of the system as given by (9). For a better understanding, Figure 22 shows the load and system curves as a function of the local-end voltage. The dotted line at 60° indicates the matched load case where the load is matched to the cable resistance.

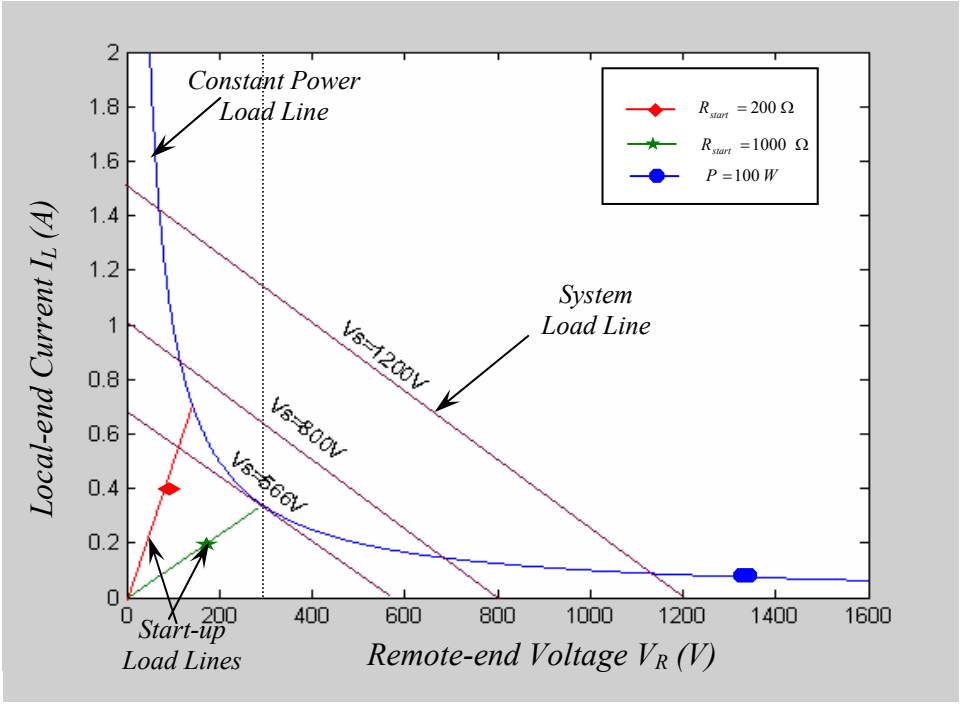

Figure 21: V-I Characteristic of switcher

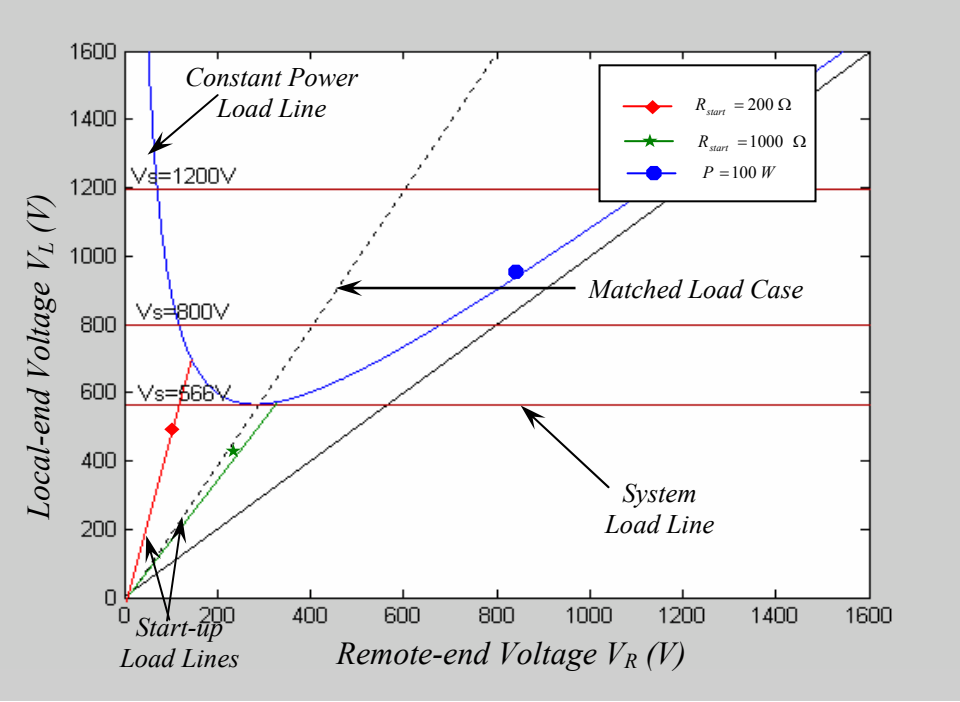

Figure 22: System characteristic with constant power load

3.2.1. Startup Effects

Consider a typical system of a switcher operated with a cable resistance of 800Ω, a startup resistance of 200Ω and a regulating power of 100W. It can be clearly seen from Figure 23 that a local-end voltage of 500 V is insufficient for the converter to start regulating and hence the only equilibrium point is on the startup resistive curve. As the local-end voltage is increased to 570 V, the system load line intersects the constant power line at one point and the resistive startup line at another point. However, since the converter can only start regulating when the remote-end voltage has increased to 141 V, the system remains on the startup curve though this voltage is sufficient to operate the converter in regulation. As the local-end voltage of 707 V is reached, there are two possible remote-end voltage equilibrium points on the constant power load curve, one at 566 V and the other at 141 V. It will be shown later that the equilibrium at the lower remote-end voltage is unstable and hence, the remote-end voltage would suddenly jump from the lower voltage of 141 V to the stable equilibrium of 566 V for an incremental change in the local-end voltage. A simple explanation for this behavior is that the system

equilibrium at a remote-end voltage of 566 V corresponds to the maximum duty cycle at startup while the stable equilibrium remote-end voltage of 141 V corresponds to the steady state duty cycle of the switching regulator. The local-end voltage would now need to be brought down by the operator to 570 V to maintain the remote-end voltage at the nominal voltage of 300 V.

The start up resistance determines the stable operation of the converter and the voltage required at the local-end for the switching converter to start regulating. In most PWM converters, the duty cycle saturates to the maximum allowed value during startup, leading to a small resistance seen at the input of the converter. Though it is possible to limit the duty cycle to reduce voltage jumps at the remote-end, this approach is not practical due to the necessity of operation with varying startup loads. Further, the above analysis is static in nature, and the jumps could be higher in practice due to the dynamic characteristics of the circuit. These transient voltage jumps could be catastrophic for the other linear regulators placed in parallel supplying other sensors and tools.

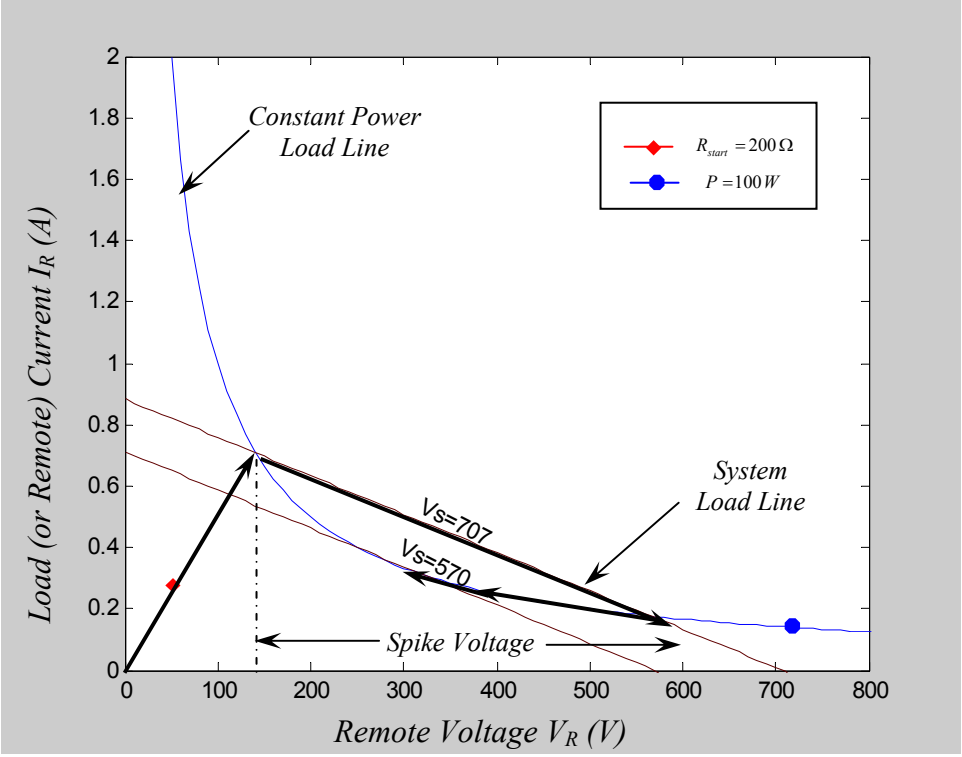

Figure 23: Voltage jump phenomenon in switching regulators

3.2.2. Startup behavioral analysis

In this section, a quantitative analysis of the voltage jump phenomenon discussed in the previous section is performed. The voltage jump can be estimated for a given regulating power P and a startup resistance R_S (which is smaller than the cable resistance R_C). When the load startup resistance is greater than the cable resistance, there is no voltage jump at startup and the switcher gets into regulation smoothly. Further, it has been assumed that the regulating power level is less than the maximum power that can be delivered to the remote-end. The voltage V_1 at the intersection point of the resistive and constant power curves is given by Equation (10).

$$V_1 = \sqrt{PR_{start}} \tag{10}$$

The local-end voltage $V_{L,i}$ at the intersection point is defined by Equation (11).

$$V_{L,i} = V_1\left(1 + \frac{R_C}{R_{start}}\right) \tag{11}$$

For simplicity, define a dimensionless quantity α given by Equation (12) that relates the local-end voltage at the intersection and the regulator power, where A.M. and G.M. refer to the arithmetic and geometric means of the quantities.

$$\alpha \equiv \frac{4PR_C}{V_{L,i}^2} \equiv \frac{4R_C R_{start}}{\left(R_C + R_{start}\right)^2} \equiv \left(\frac{GM\left(R_C, R_{start}\right)}{AM\left(R_C, R_{start}\right)}\right)^2 \leq 1 \tag{12}$$

The stable equilibrium point V_2 defined by the intersection of the system load line given by the local-end voltage and the constant power load curve can be represented in terms of α as:

$$V_2 = \sqrt{\frac{PR_C}{\alpha}}\left(1 + \sqrt{1-\alpha}\right). \tag{13}$$

The voltage jump at startup can be obtained as the difference of V_1 and V_2 as:

$$V_{jump} = V_2 - V_1 = \sqrt{\frac{PR_C}{\alpha}}\left(1 + \sqrt{1-\alpha} - \sqrt{\frac{\alpha R_{st}}{R_C}}\right). \tag{14}$$

The implication of the above criterion is that the voltage jump can be reduced by an increase in the startup resistance of the switching converter. This can be achieved practically by either starting up the system at no-load/reduced load or by specifying a

maximum limit on the duty cycle of the switching converter at start-up. Practical adaptation of any of these two methods leads to a very slow dynamic performance at startup and reduced power delivery. Further, this may be undesirable as the remote-end voltage required for regulation at maximum power at the load end may be too high when started up at very low loads. Ideally, the startup resistance should match the cable resistance as soon as possible for maximum power transfer and this cannot be performed effectively for varying startup and load conditions except by controlling the local-end voltage.

3.2.3. Maximum power delivery

As was earlier remarked, the constant power load at the remote-end leads to two equilibrium points for the same local-end voltage. The stability of the two equilibrium points is investigated. The equation governing the dynamics of the system with a constant power load as stated earlier is given by:.

$$\frac{dv_R}{dt} = \frac{1}{C}\left(\frac{V_L - v_R}{R_C} - \frac{P}{v_R}\right) \tag{15}$$

The equilibrium points determined by equating the right hand side of Equation (15) to zero are given by Equation (16).

$$V_R = \frac{V_L}{2} \pm \sqrt{\frac{V_L^2}{4} - PR_C} \tag{16}$$

The remote-end voltage equilibria for varying values of the constant power load supplied is shown in Figure 24. It can be seen that there is no solution for a remote-end voltage when the power demanded by the load exceeds the system capacity as stated in Chapter 2. The system would collapse during this condition and the remote-end switching converter would get out of regulation. Further, it can be noticed that at the limiting point, the remote-end voltage is half the local-end voltage and the load is matched to the cable resistance.

The system dynamic defined by Equation (15) is nonlinear in nature. The local stability of the equilibrium points of a nonlinear system can be determined by examining the eigenvalues of the linearized system [19]. The eigenvalues of the system can be given in terms of the equilibrium remote-end voltage V_R as:

$$\lambda = \left.\frac{d\left(\frac{dv_R}{dt}\right)}{dv_R}\right|_{v_R=V_R} = \frac{1}{R_C C}\left(\frac{PR_C}{V_R^2} - 1\right). \tag{17}$$

From (17) it is seen that the system is locally stable if

$$\lambda < 0 \;\Rightarrow\; V_R > \sqrt{PR_C}. \tag{18}$$

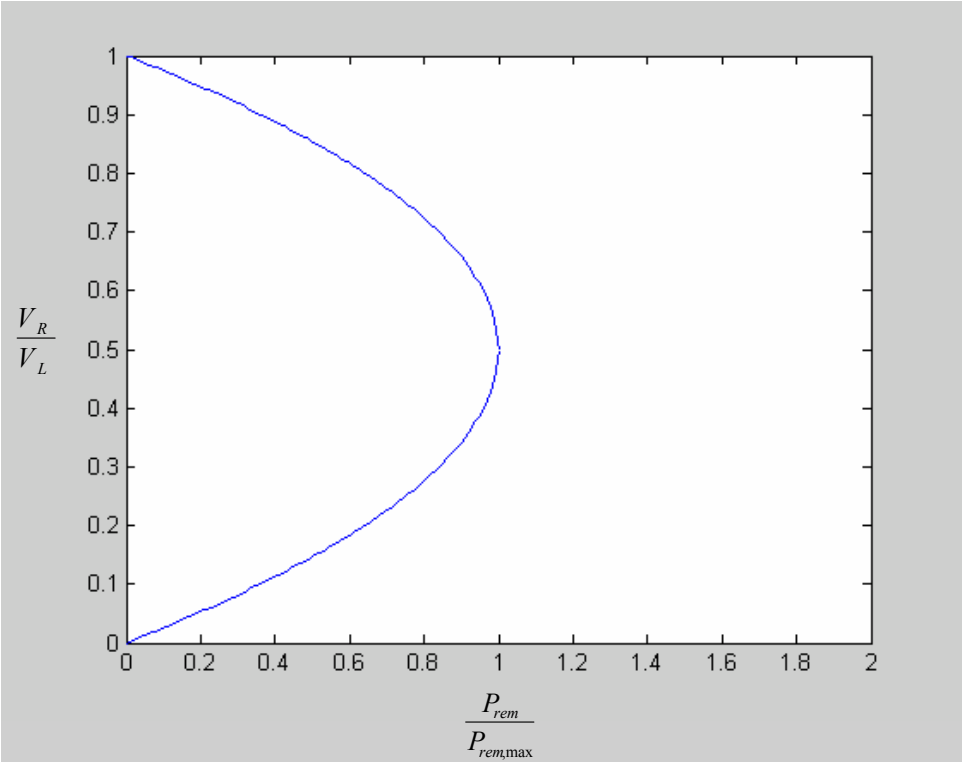

Figure 24: Remote-end voltage equilibria for constant power loads

A simple examination of the stability of the remote-end voltage equilibrium points given by Equation (18) leads to the conclusion that the equilibrium at higher remote-end voltage and lower remote-end current is stable whereas the other equilibrium at low remote-end voltage is unstable. This can also easily be observed by looking at the behavior of the system in the state plane using Figure 25. For clarity, the Y-axis has been scaled to include the capacitance and cable resistance (800 Ω).

Consider a small decrease in the remote-end voltage when the system is at the equilibrium at low remote-end voltage and high remote-end current. Any decrease in

remote-end voltage leads to a negative derivative of the remote-end voltage. But, any decrease in the remote-end voltage derivative would lead to a further decrease in the remote-end voltage leading to instability. On the other hand a small increase in the remote-end voltage would keep increasing the remote-end voltage until the stable equilibrium is reached. The repelling behavior of this equilibrium coupled with the attractive behavior of the other equilibrium point is the reason for voltage jumps at startup. Hence it is clear that the equilibrium at low remote-end voltage is a non-attracting unstable equilibrium. The other equilibrium can be analyzed in a similar manner and is found to be locally stable in the region where the remote-end voltage is greater than the unstable point.

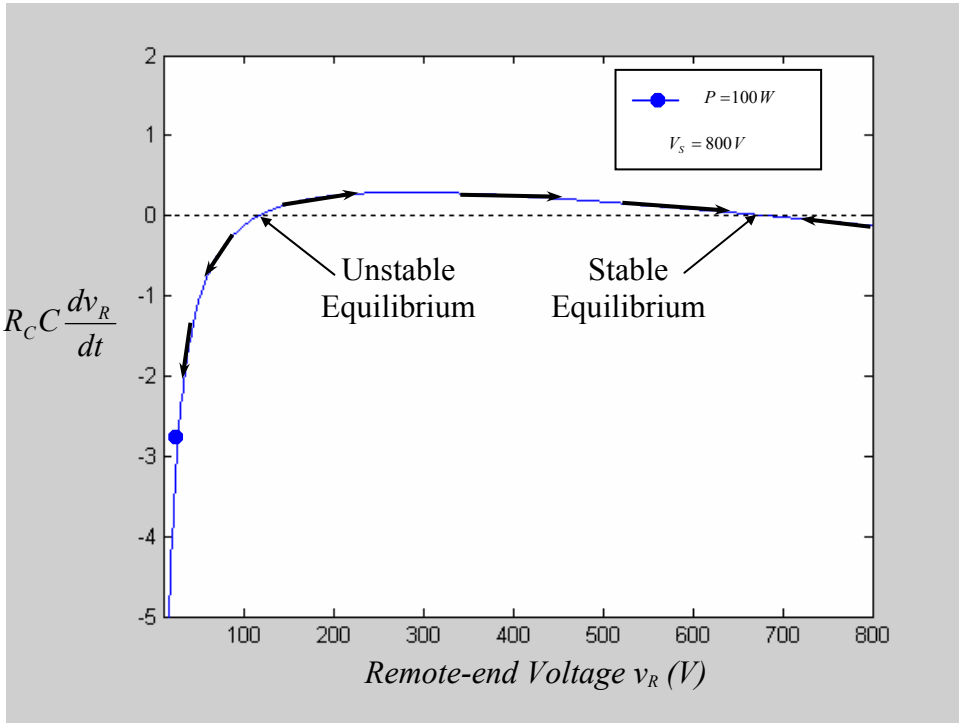

Figure 25: State plane diagram of constant power load system

The power limit for a typical example DC source system used in the oil drilling industry with an ideal switcher can be determined in this case as given in Equation (11). For example, suppose a cable resistance of 800Ω, a local-end voltage limit of 1000 V, cable current limit of 1 A and a remote-end voltage of 330 V, then

$$P_{\max} = \frac{V_{R,nom}^2}{R_C} = 136\ W. \tag{19}$$

It can be seen clearly that the ideal switcher greatly diminishes the power that can be delivered to the loads when the remote-end voltage needs to be maintained constant at lower than optimal levels. Note that this power level is similar to that which can be obtained from a linear regulator method with an efficiency of 40% (132 W @ 330V, 1A input at the remote-end).

3.2.4. Load Change Transients

As with the linear regulators, the load change transient analysis has been performed assuming ideal constant power load behavior. Consider a gradual load change in the system from 100 W to 50 W (see Figure 26 and Figure 27). The system operates at a local-end voltage of 575 V to maintain 100 W output at the remote-end at a nominal voltage of 330 V. When for example if the load at the remote-end goes into the low power operating mode and reduces its power output to 50 W, the remote-end voltage rises to almost 494 V. The remote-end voltage needs to be brought back to 330 V nominal by the operator with a reduction in the local-end voltage to 452 V.

Further, it can be seen that for a load change from 50 W to 100 W when the system is operating at the nominal voltage, the system can no longer operate as a constant power load. The switcher gets out of regulation and follows the resistive startup line. The system voltage would need to be increased until the resistive startup line hits the constant power curve corresponding to 100 W beyond which the switcher starts regulating. Hence, the remote-end voltage is susceptible to voltage transients and spikes during load changes as was the case with linear regulators.

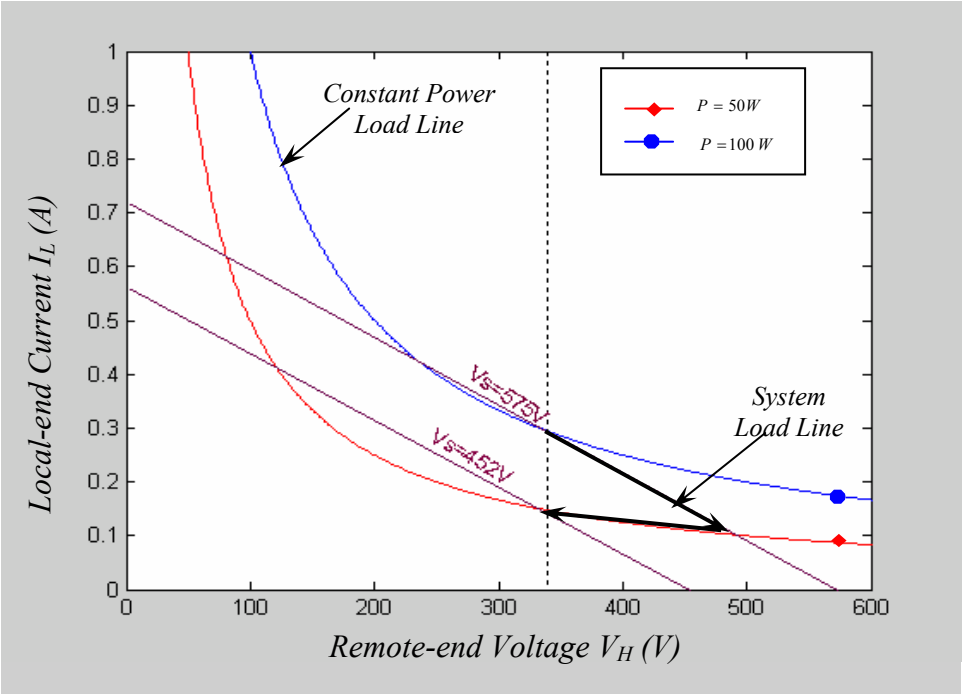

Figure 26: Load change transient behavior (Remote-end)

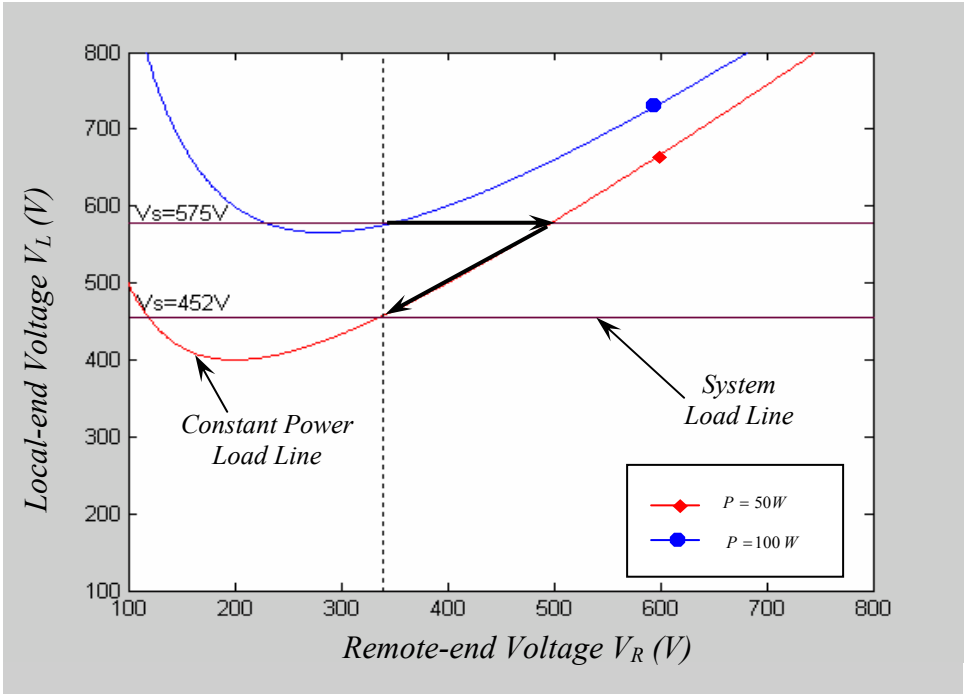

Figure 27: Load change transient behavior (Local-end)

3.2.5. Experimental verification

3.2.5.1. Experimental details and results

The jump phenomenon during startup and maximum power delivery limit for a switcher operated at the remote-end were verified with a high voltage power system (HVPS) using the facilities provided by Schlumberger, Inc., Houston. The HVPS converter, shown in block diagram form in Figure 28, consists of a half bridge converter modulated at a switching frequency of 150-200 kHz while the output voltage is regulated at a frequency of 5 kHz. The HVPS system was connected to an adjustable AC power supply at the local-end and the operation of the converter for different loads was studied.

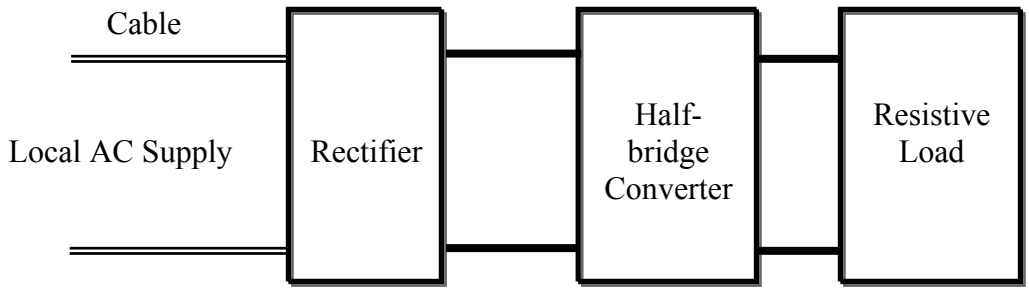

Figure 28: HVPS system

The setup was tested on a cable of length 18000 ft (corresponding to a resistance of 400Ω). The startup behavior was first observed for a regulating load power of 31W. It should be noted that this corresponds to the power delivered at the DC output end and is not the power input to the switcher. The efficiency of the converter measured was approximately 80% during the entire operation. A sample of the local-end voltage and current waveforms with the remote-end voltage waveform is shown in Figure 29. All measurements were made in terms of peak-to-peak values as the waveforms are distorted as can be seen from Figure 29. The distortion in the waveforms is due to the effect of the capacitive rectification unit at the remote-end.

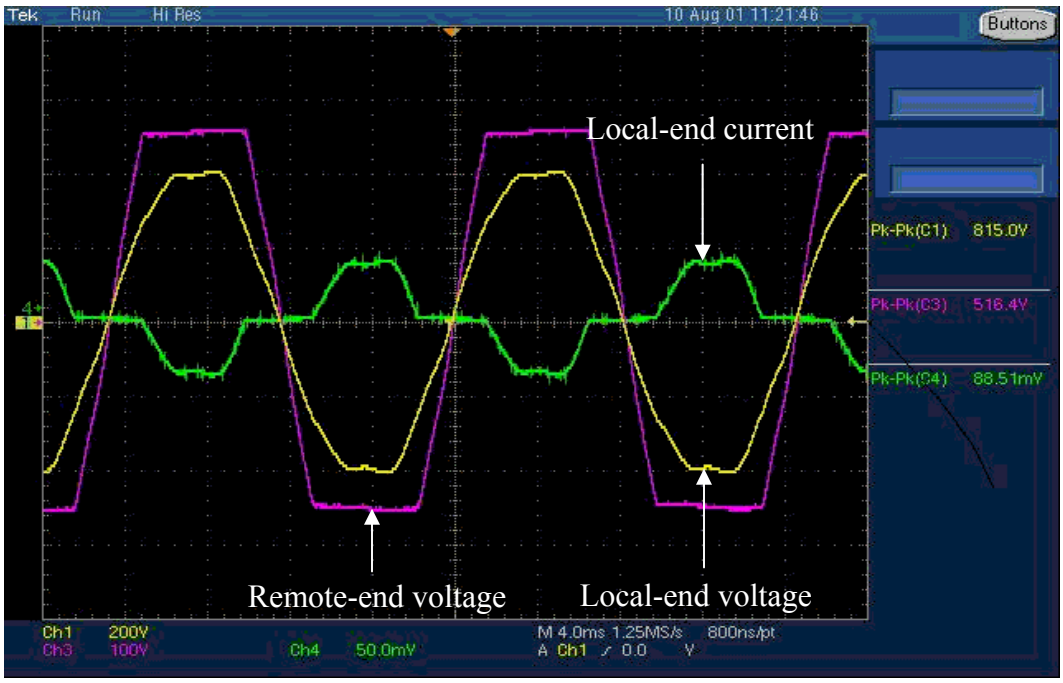

Figure 29: Sample waveforms in HVPS system

The time waveforms illustrating the startup and jump phenomenon are shown in Figure 30 and Figure 31. The remote-end voltage jumps from approximately 193 $V_{pk\text{-}pk}$ to 530 $V_{pk\text{-}pk}$ when the remote-end voltage is increased incrementally beyond 790 $V_{pk\text{-}pk}$. A better understanding of the experimental results can be obtained from Figure 32 and Figure 33 where only the peak values of the remote-end voltage and local-end voltage and current have been plotted respectively. The remote-end voltage jump for an incremental change in local-end voltage is clearly visible in Figure 32. Also, the drop in switcher input current from 1.6 $A_{pk\text{-}pk}$ to 1 $A_{pk\text{-}pk}$ when it goes into regulation can be observed in Figure 33. Also, as the local-end voltage is decreased after the switcher starts regulating, the system remains in regulation until the remote-end voltage falls to approximately 300 $V_{pk\text{-}pk}$ when the system again jumps onto the resistive startup curve. This would correspond to the minimum remote-end voltage that is necessary to sustain the load power in this case of 31 W.

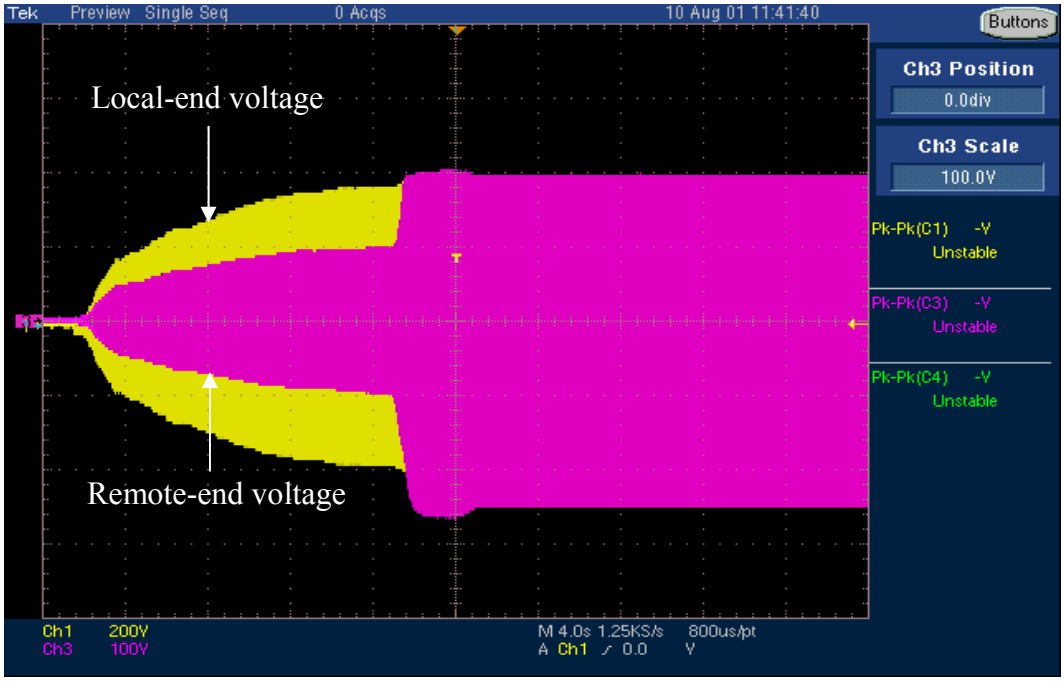

Figure 30: Jump phenomenon in switching regulators

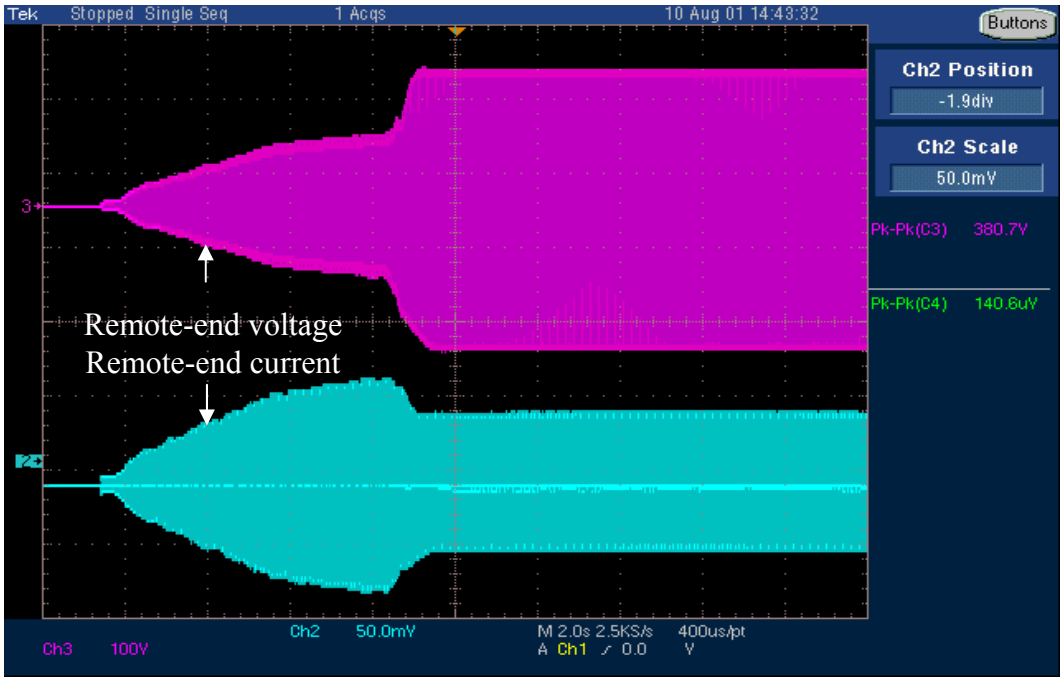

Figure 31: Jump phenomenon in switching regulators

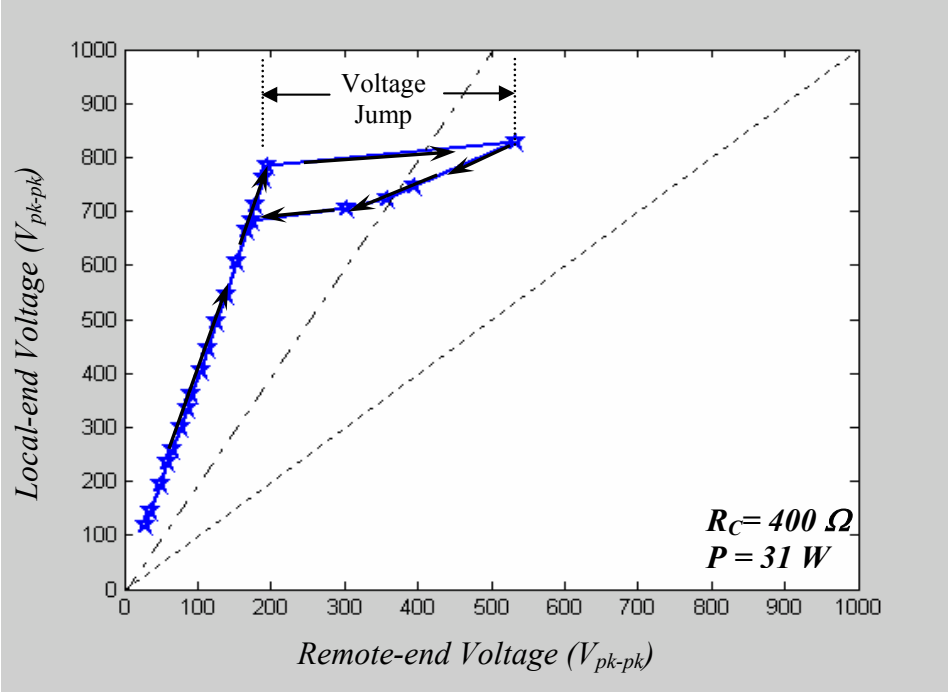

Figure 32: Startup behavior (Local-end)

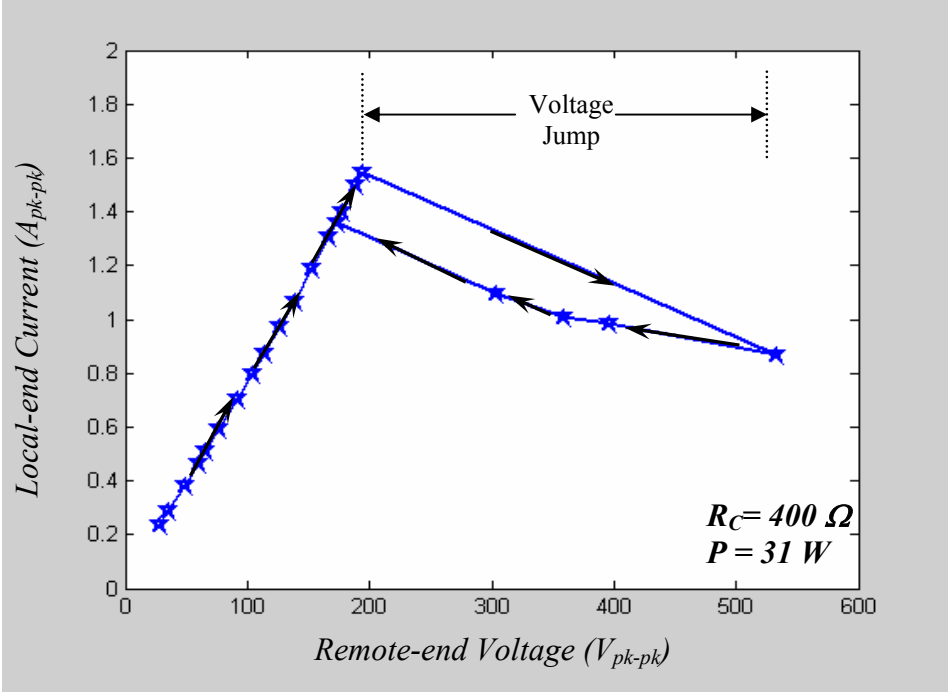

Figure 33: Startup behavior (Remote-end)

The behavior of the system for load changes was also studied. The transient behavior of the remote and local-end voltages for a load change from 30W to 48W for the system is shown in Figure 34. The remote-end voltage drops from 705 $V_{pk\text{-}pk}$ to 455 $V_{pk\text{-}pk}$ after the load change. It can be found that if the load was changed to 75W, the local-end voltage available cannot maintain regulation and the system will once again get into the startup resistive mode and a complete startup cycle would need to be done again.

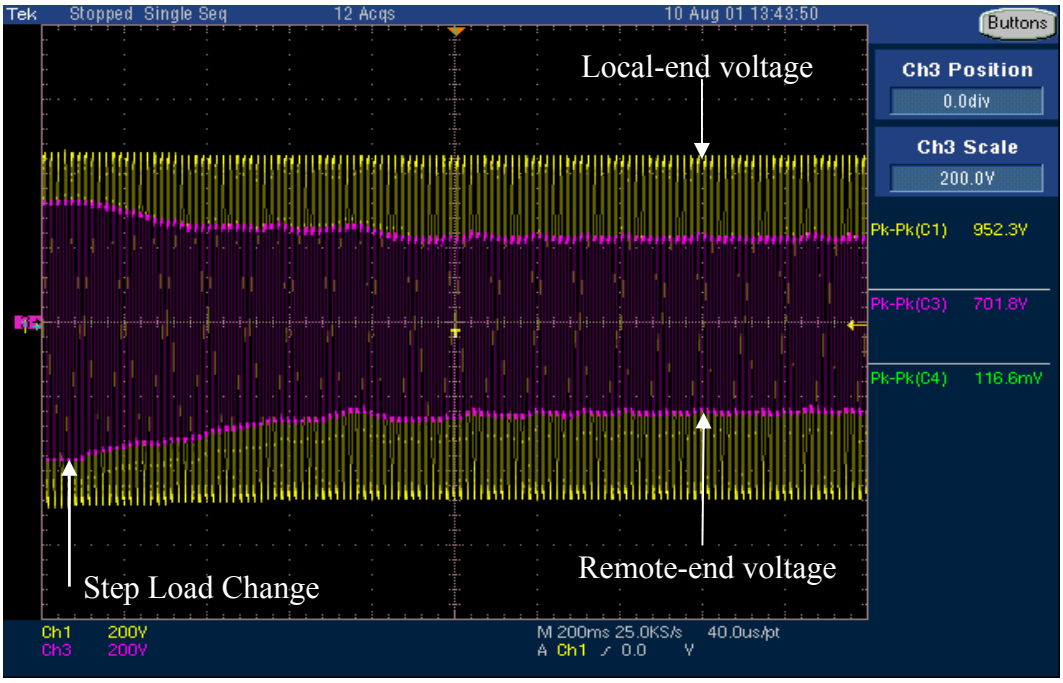

Figure 34: Load transient waveforms in HVPS system

3.2.5.2. Verification of theoretical analysis

Consider an AC system with a cable resistance (R_C) of 400Ω, a startup resistance (R_{start}) of 120Ω and a regulating power (P) of 31 W. Since the system under consideration is an AC system with a rectifier front-end, the predictions reported earlier need to be modified taking into account the capacitive rectifier characteristics. The minimum remote-end voltage required for output voltage regulation is easy to determine by just considering the capacitive rectifier characteristics. It was noted earlier that the capacitive rectifier modulates the input cable resistance to a higher value leading to a

lower power output. At maximum deliverable load power, the ratio of the cable resistance to the load resistance was found to be around 1.33 (see Chapter 2). The minimum peak remote-end voltage required for output voltage regulation in this case can be calculated by modifying the cable resistance to 1.33 times its actual value and using the actual power delivered taking into account the efficiency of the system to be:

$$V_{R,\min} = \sqrt{\frac{1.33PR_C}{\eta}} = \sqrt{\frac{1.33\times 31\times 400}{0.8}} = 143.5V\ (\approx 287\ V_{pk-pk}). \qquad (20)$$

The predicted value agrees well with the experimental value of 300 $V_{pk\text{-}pk}$.

It is not easy to determine the jump voltage for a capacitive rectifier front end. Rather, the accuracy of the DC system prediction as compared to experimental results is examined. The jump in remote-end voltage during startup can be estimated by using Equation (14) to be:

$$V_{jump} = \sqrt{\frac{PR_C}{\eta\alpha}}\left(1+\sqrt{1-\alpha}-\sqrt{\frac{\alpha R_{st}}{R_C}}\right);\ \Rightarrow\ V_{jump} = 162\ V\ \left(\approx 324 V_{pk-pk}\right). \qquad (21)$$

In the experiments, the remote-end voltage jumped from 193 $V_{pk\text{-}pk}$ to 530 $V_{pk\text{-}pk}$ corresponding to a jump voltage of 337 $V_{pk\text{-}pk}$ which agrees with the theoretical prediction.

The startup behavior was also studied experimentally for other rated load powers of 17W and 60 W. The startup resistance was approximately constant at 120Ω through the entire experiment. It should be noted that this is an approximation, with the assumption that the remote-end voltage and current are sinusoidal, though in practice both waveforms are distorted. The experimental results and the theoretical predictions for minimum remote-end voltage for regulation and the jump voltage during startup have been compared for the above stated load powers in Table 1. In all cases the match between the theoretical and experimental predictions was within 15%. The match was better at higher load powers indicating the validity of the ideal theoretical calculations.

Table 1: Comparison of experimental results and theoretical predictions

Load Power (W)	*Minimum remote-end voltage for regulation (V_{pk-pk})*		*Remote-end voltage jump at startup (V_{pk-pk})*	
	Prediction	*Experimental Result*	*Prediction*	*Experimental Result*
17	213	240	231	205
31	287	300	324	337
60	400	421	445	470

3.3. Other remote power conversion methods and their limitations

The earlier sections dealt with issues related to the primary power distribution methods, namely linear and switching regulators. A brief comparison highlighting the advantages and disadvantages of secondary power distribution methods is performed in this section.

3.3.1. Fixed duty ratio switcher

A switching regulator can be operated in open loop with a fixed duty ratio as a front end converter and a load end post-regulator can be used to regulate the voltage. The switching regulator in open loop operation behaves like a resistive load as the output voltage is not regulated. Though, the stability problems of the switching regulator are eliminated by this method, remote-end voltage transients due to load changes cannot be avoided. Further, the improvement in efficiency is only marginal as compared to the linear regulator since the wide variation in line and load conditions (coupled with the unregulated output of the switcher) lead to a post-regulator that needs to be over-designed.

3.3.2. Shunt regulator-switcher parallel method

A shunt regulator can be used to regulate the remote-end voltage with the local-end voltage set at the maximum allowable voltage. The shunt regulator maintains the remote-end voltage by compensating for the switcher current and the combined load in

this case resembles a constant current sink. The shunt regulator system is shown in Figure 35. For the sake of clarity, the input rectifier and filter have been neglected.

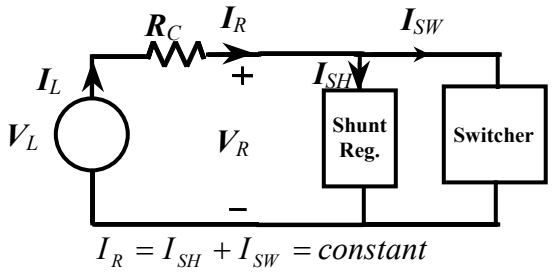

Figure 35: Shunt regulator-switcher system

The voltage jumps during startup and load changes are eliminated with reasonable efficiency of power transfer due to the switcher. The main drawback of this method is the requirement of increased power dissipation capability when the switcher is processing minimal power. In this case, the shunt regulator would need to dissipate the entire maximum current. Also, in this method the power delivered to the remote-end is constant with maximum dissipation in the cable and hence is not efficient from a local-end point of view.

3.3.3. Cascaded Conversion Method

Cascaded converters at the remote-end would be an effective and user friendly method of delivering the maximum power to the load. The front-end converter would regulate the remote-end voltage to the corresponding reference voltage while the load-end converter would regulate the load voltage. The local-end voltage can be ramped up during startup to its maximum voltage and maintained at the high voltage. Thus, by this method power levels of up to the system capacity can be sustained with minimal dissipation in the cable. In this case, though the remote-end voltage would vary with load changes.

A SPICE simulation of the cascaded system approach (averaged model) has been shown in Figure 36. The cascaded system was implemented with a DC source and buck converters in cascade. The load end converter was turned on only when the front-end converter output voltage was more than 280V. The load end converter has a startup load

of 100 W and a load change to 225 W was introduced at 7.5 sec. It can be seen that the converter output voltages are almost insensitive to the load changes while the local-end voltage varies.

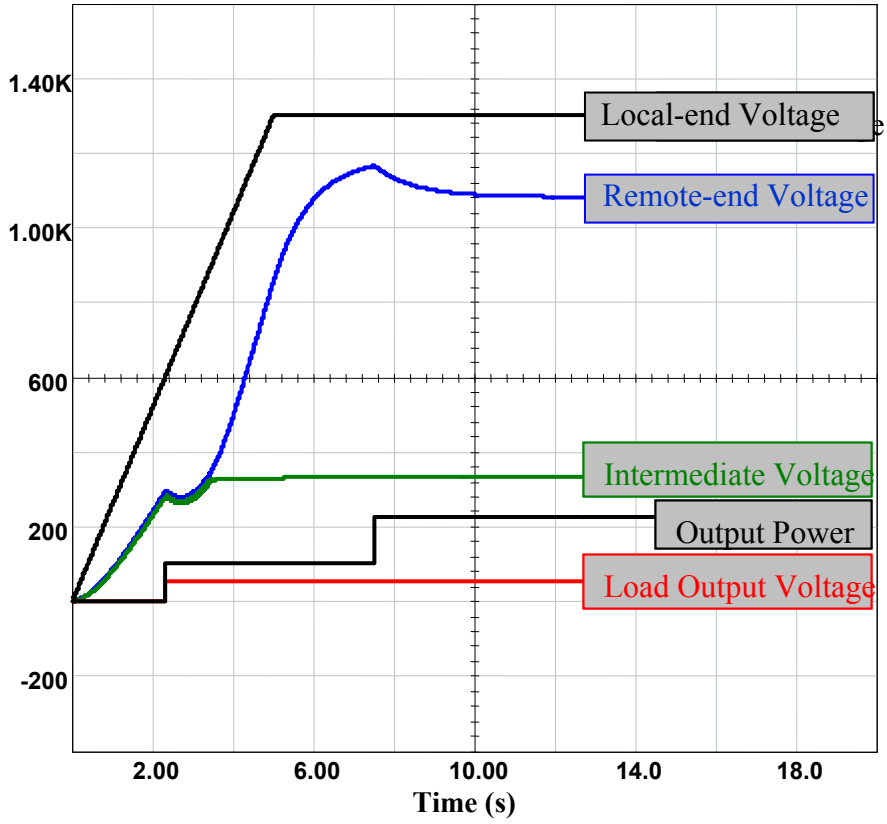

Figure 36: Cascaded system simulation results

The main disadvantage of this method is that the front-end converter would need to be rated for full load and maximum local-end voltage to account for maximum to minimum load transitions. The high voltage electronics required coupled with the high temperature specifications can lead to a reduction in the maximum local-end voltage available for safe operation. Also, the increased component count of this method would be a liability from a practical standpoint. Further, the wide regulation capability required for the front-end converter might not be possible from a practical standpoint necessitating additional converters for post-regulation leading to a reduction in overall system efficiency.

For a quick comparison, information about the power delivery, efficiency, advantages and disadvantages of the various secondary power distribution methods discussed above have been provided below in a tabular form.

Table 2: Comparison of power delivery methods

Method	*Features/Advantages*	*Disadvantages*
Shunt Regulator - Switcher Parallel Combination	▪ Increased power output ▪ Stable at all operating conditions	▪ Bulky ▪ Dissipation capability of shunt regulator should be full load ▪ Load changes lead to remote-end voltage jumps
Fixed Duty Ratio Switcher	▪ Stable at all operating conditions	▪ Inefficient due to insufficient regulation ▪ Post regulator needs large dissipation capabilities ▪ Load changes lead to remote-end voltage jumps
Cascaded Method	▪ Increased power output ▪ No voltage jumps at startup for regulated remote-end voltage ▪ Load changes do not affect the remote-end voltage ▪ Operator handling is minimized	▪ First stage has to regulate over a wide input range ▪ Strict control of the remote-end voltage might be difficult due to the wide input range ▪ Ratings of first stage coupled with the high temperature requirements may be too high for existing power devices ▪ Increased component count

3.4. Conclusions

In this chapter, the existing remote power conversion methods were analyzed from both theoretical and experimental standpoints. Previously unreported phenomena such as load cycling during startup voltage jumps during startup with switching converters were analyzed and validated experimentally. The two main solutions to the power delivery problem, namely the linear and switching regulators and the problems associated with each of these solutions were discussed in detail. The linear regulator is inefficient and bulky but is easy to operate and is always stable. The switching regulator on the other hand, is prone to voltage spikes during startup and reduces the maximum

power delivered to the remote-ends when the system is operated at a sub-optimal remote-end voltage (that is, a remote-end voltage less than the maximum local-end voltage). New remote power conversion methods that alleviate some of these problems are developed and validated in the next chapter.

.

CHAPTER 4

NEW REMOTE POWER CONVERSION METHODS

The previous chapter illustrated the difficulties involved in the operation of the current remote power conversion methods. Ideally, the remote instrumentation system should be operated at a reference remote-end voltage that is half the maximum local-end voltage for optimal power delivery. But in practice, the remote-end voltage may be constrained to a certain maximum value independent of the local-end voltage limits due to noise, corona discharge and other mitigating factors such as input voltage regulation range and high voltage electronics at significantly high temperatures. In such a situation, the maximum power delivery limit of a switching converter operated at the end of a long resistive cable is limited by the maximum reference remote-end voltage and not by the local-end voltage as was illustrated in the previous chapter. In this chapter, two novel remote power conversion methods are proposed that increase the power delivered to the remote-end even when operated in sub-optimal conditions compared to the methods illustrated in the previous chapter. The state feedback based voltage follower method is based on feedback of the remote-end voltage along with the converter state variables to control the system while the series regulator-switcher parallel combination is based on a novel feedback that integrates the series regulator and switcher into a single unit.

4.1. State feedback based voltage follower

As seen in the previous section, controlling the output power by strictly controlling the output voltage of the switcher leads to instability problems, and hence, a relaxation of the control severity can increase the power delivered. Rather than controlling the output voltage strictly, state feedback without integral action can be used to control the switching regulator. In this method, the remote-end voltage is also used as a feedback variable along with the state variables of the switching regulator so that for an increase or decrease in output power beyond the nominal operating condition, the output

voltage of the switcher is not regulated and "*follows*" the remote-end voltage. For example, an increase in the output power would lead to a decrease in the remote-end voltage that in turn leads to a decrease in the output voltage of the converter. By allowing the output voltage of the switcher to vary in a range, the system can deliver power beyond the stability limit of a pure switcher. For a nominal output voltage and output power, the system can be stabilized to obtain a good regulation. The block diagram of the control method is shown in Figure 37.

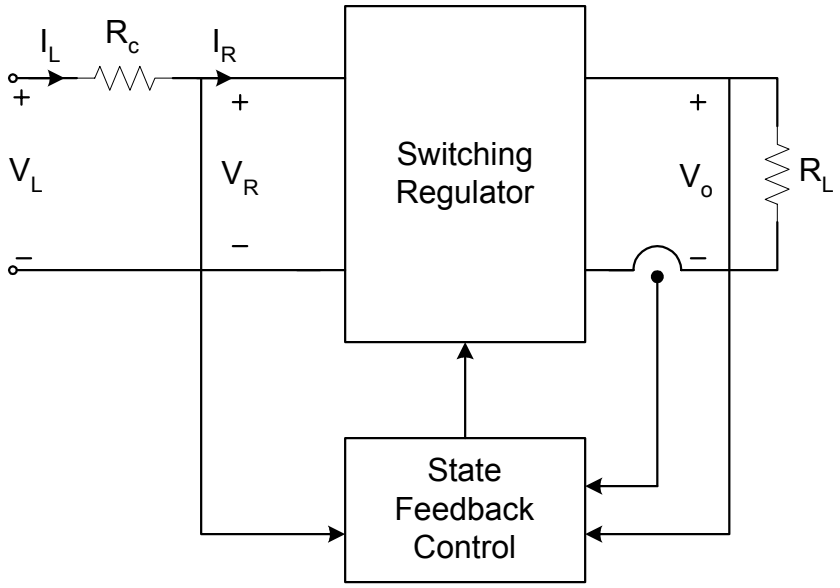

Figure 37: Integrated state feedback based voltage follower method

The duty ratio of the switching converter (d) is based on a feedback of the remote-end voltage (v_R) and the output load voltage (v_o) as given below:

$$d = k_1 V_{o,ref} + k_2 \left(v_o - V_{o,ref} \right) + k_3 \left(v_R - V_{R,ref} \right) \tag{22}$$

where k_1, k_2, and k_3 are control gains and $V_{o,ref}$ and $V_{R,ref}$ refer to the reference output and remote-end voltages respectively. Note that when the remote-end voltage is approximately equal to the reference remote-end voltage, the state feedback converter operates as a regular switching power supply. When the remote-end voltage is higher or lower than the reference remote-end voltage, the duty ratio of the state feedback

converter is appropriately increased or lowered leading to an increase or decrease in the load output voltage. The control gain k_3 controls the rate at which the output voltage "*follows*" the remote-end voltage changes. Also, as the control gain k_2 multiplying the difference of the load output voltage and the reference output voltage is increased, the regulation is improved. But as the regulation improves with the increase in control gain k_2, the stability of the system is impaired at power levels beyond the maximum power limit of a pure switcher and the system may no longer be stabilized. A trade-off between the stability at higher power levels and the output voltage regulation is hence an inherent characteristic of this method.

4.1.1. Simulation analysis

The state feedback method was simulated using SPICE for a test converter with a nominal output voltage of 130 V at a load resistance of 75 Ω and a cable resistance of 800 Ω. The nominal remote-end voltage was 330 V with a local-end voltage limit of 1000 V. The power limit of a pure switcher for these voltage conditions corresponds to:

$$P_{ideal,\max} = \frac{V_R^2}{R_C} = \frac{330^2}{800} = 136\,W \tag{23}$$

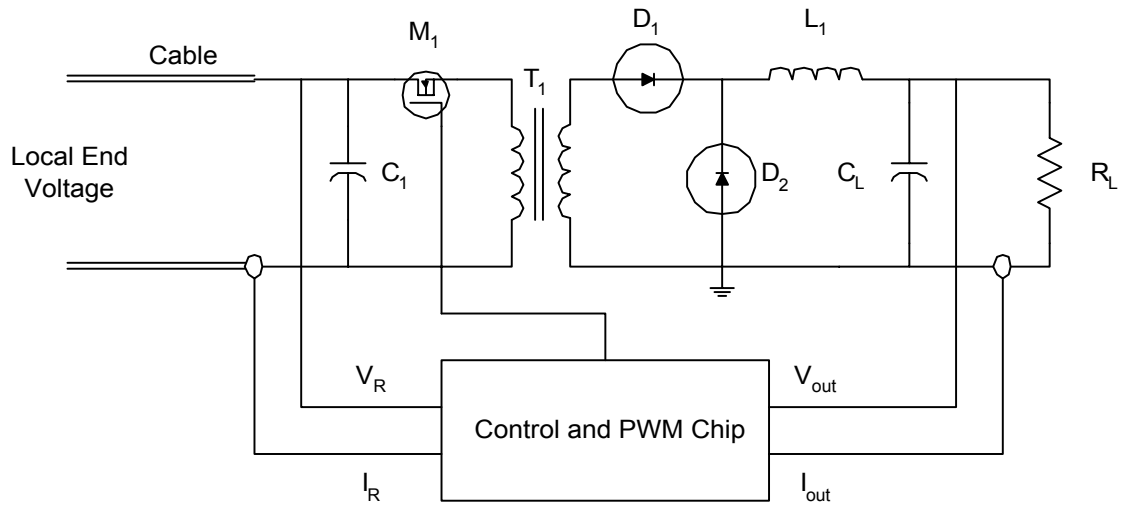

Figure 38: Simulation setup for state feedback based voltage follower method

The simulation setup shown in Figure 38 consists of a forward converter as the remote-end front-end converter that provides a nominal output voltage of 130 V at an input remote-end voltage of 330 V. The duty ratio of the converter was obtained by state feedback of the input variables to the converter (namely the remote-end voltage and current) and the output variables of the converter (load current and voltage) as in Equation (22). The control gains k_1, k_2, and k_3 were appropriately chosen to provide good regulation and stability behavior. The results of the simulation are shown in Figure 39. The remote-end voltage was stabilized at 320 V at a local-end voltage of 840 V. It can be seen that the output voltage is stabilized at around 123 V with a load power of 202 W. This is definitely an improvement over the maximum power delivered by a pure switcher. When the load resistance is increased to 150 Ω, the output voltage and remote-end voltage both increase to 469 V and 179 V respectively. At this point, the system is actually supplying more power than is required by the load and the extra energy will need to be dissipated as heat by the post regulators. When the remote-end voltage is brought down to 336 V, the output voltage decreases to 133 V and the output power stabilizes to 118 W.

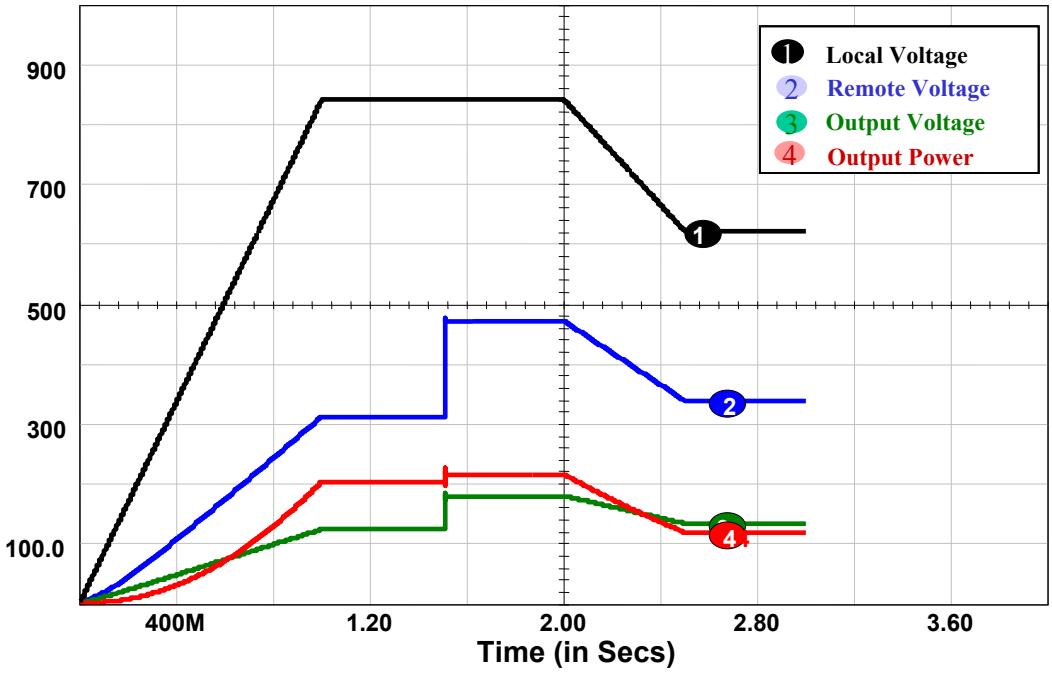

Figure 39: State feedback based voltage follower results

4.1.2. Experimental setup

The state feedback voltage follower method was implemented in a remote instrumentation system prototype with the remote-end voltage maintained at 20 V, an output voltage of 8 V and a cable resistance of 100 Ω. Note that the power limit for this system for an ideal switching converter at the remote end as explained in Chapter 3 is given by:

$$P_{ideal,\max} = \frac{V_R^2}{R_C} = \frac{20^2}{100} = 4W \tag{24}$$

A buck converter was used as the remote-end power converter. The buck regulator was operated at a switching frequency of approximately 12 kHz using the Unitrode UC3824 PWM voltage mode control IC. The duty ratio of the converter was obtained by state feedback of the remote-end voltage (v_R) and the output load voltage (v_o) as in Equation

(22). The control gains k_1, k_2, and k_3 were appropriately chosen to provide good regulation and stability behavior. The output load voltage reference $V_{o,ref}$ and the remote-end reference voltage $V_{R,ref}$ were set to 8V and 20V respectively. The local-end voltage supply was a variable Hewlett Packard power supply with a 70 V voltage limit. The experimental setup is shown in Figure 40.

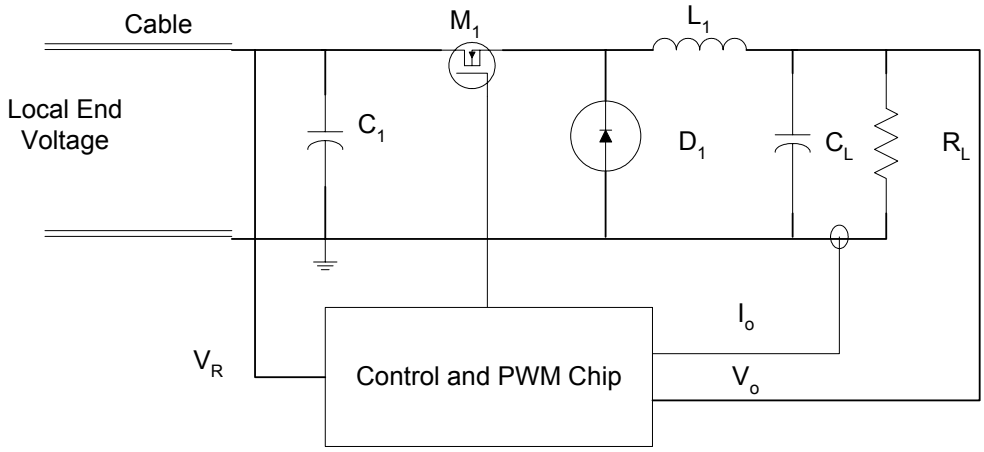

Figure 40: Experimental setup for state feedback based voltage follower method

4.1.3. Experimental results

The experimental results for the operation of the switching regulator and the overall system are shown in Figure 41. The load voltage was stabilized at 8 V for an output current level of 0.5A corresponding to a power level of 4 W (which corresponds to the power limit of an ideal switcher). It can be seen that the average value of the inductor current in Figure 41 is 0.5 A corresponding to the load current and has a ripple current of approximately 0.4 A.

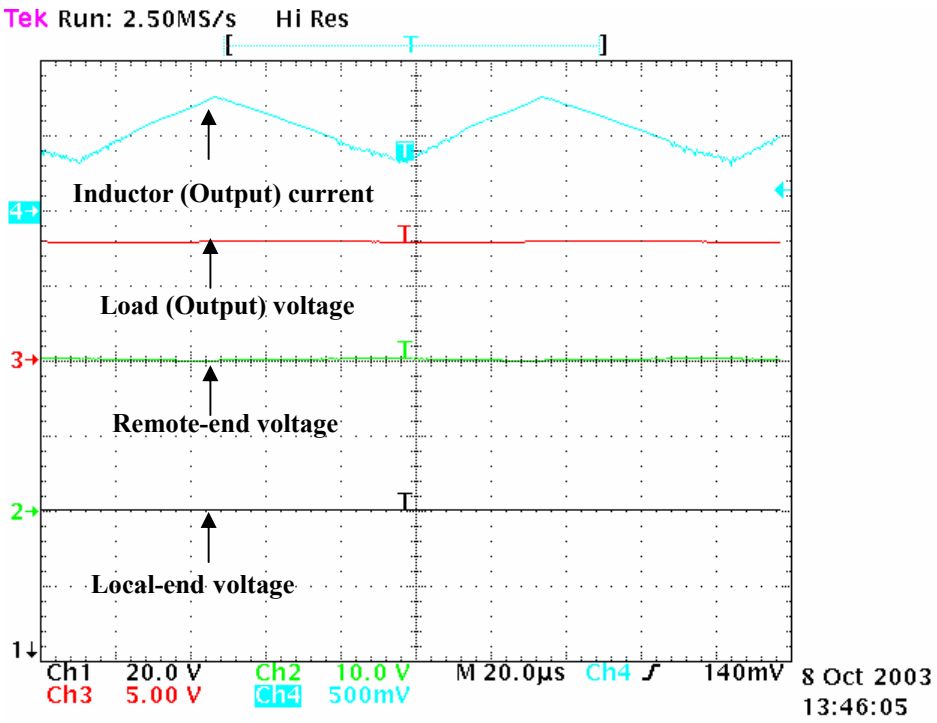

Figure 41: State feedback based voltage follower results (4W power level)

The system behavior is illustrated in Figure 42-Figure 44 for three different startup power levels and load transitions. Figure 42 shows the startup of the system at a power level of 2 W (below the system power limit of 4 W). The main difference in the startup of the state feedback based voltage follower to the switching regulator is the smoothness of the change in remote-end voltage with increases in local-end voltage (that is, there are no voltage jumps in the system behavior as compared to the startup of a switching regulator as can be seen from Figure 32). At time t=22s, the output power demand is changed to 4.5 W from the previous level of 2 W. Since the local-end voltage is insufficient to maintain this load current, the remote-end voltage that was stabilized at 20 V drops down to 10 V. The load output voltage follows the remote-end voltage and drops out of regulation to 5 V. As the local-end voltage is increased and the remote-end voltage re-stabilized at 20 V, it can be seen from the results that the load voltage also stabilizes to approximately 8V. At this juncture, the system has been stabilized at a load power level of 4.5 W. In this case, it is clear that we are able to deliver power beyond the power limits of an ideal switching converter (which is 4 W as given by Equation (24)).

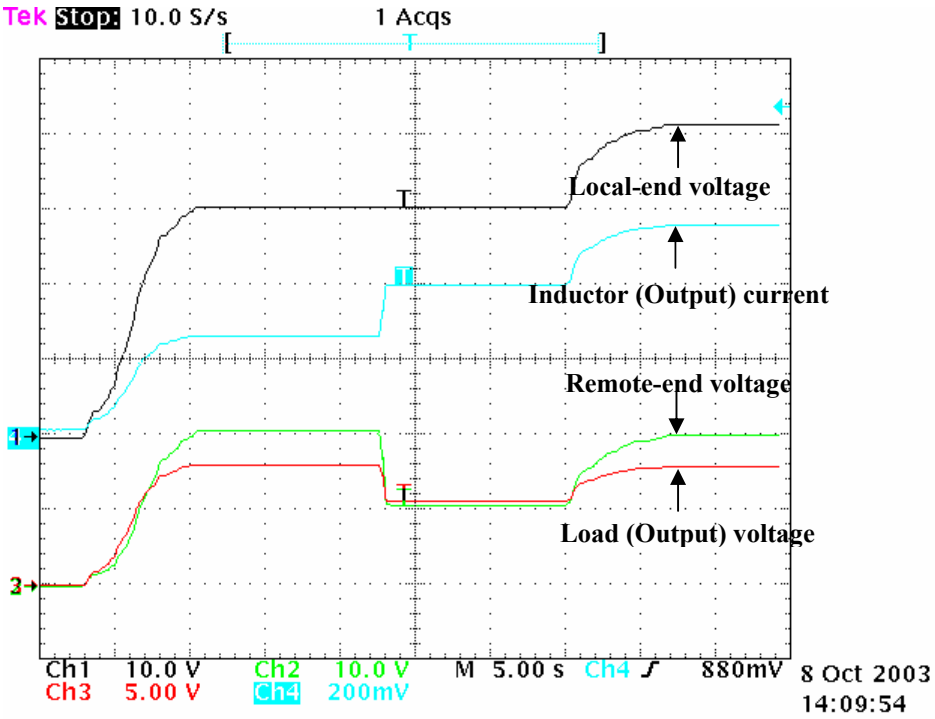

Figure 42: Voltage follower results (2W to 4.5 W transition)

Figure 43 shows a similar startup behavior but now with the system started up at a power level of 4 W and the load demand is changed to 8 W at time t=22s. The local-end voltage is at 60 V for the load power level of 8 W with the remote-end voltage maintained at 20 V. It is clear from the experimental results that in this case the new method is capable of delivering twice the ideal switcher power limit.

Figure 44 shows the behavior of the system with a startup power level of 8 W and a load change transition to 4 W at t=22 s. A smooth startup without voltage jumps is observed from the experimental results. After the load change, it can be seen that due to the excessive local-end voltage available, the remote-end voltage rises to 30 V leading to the switching converter output voltage also increasing to 10 V from its nominal value of 8 V. At this juncture, the power being delivered to the loads is more than the power demanded and in a practical system, a post regulator would be needed to dissipate the excess energy. Once the local-end voltage is reduced to bring down the remote-end voltage to 20 V, the load output voltage is regulated at 8 V.

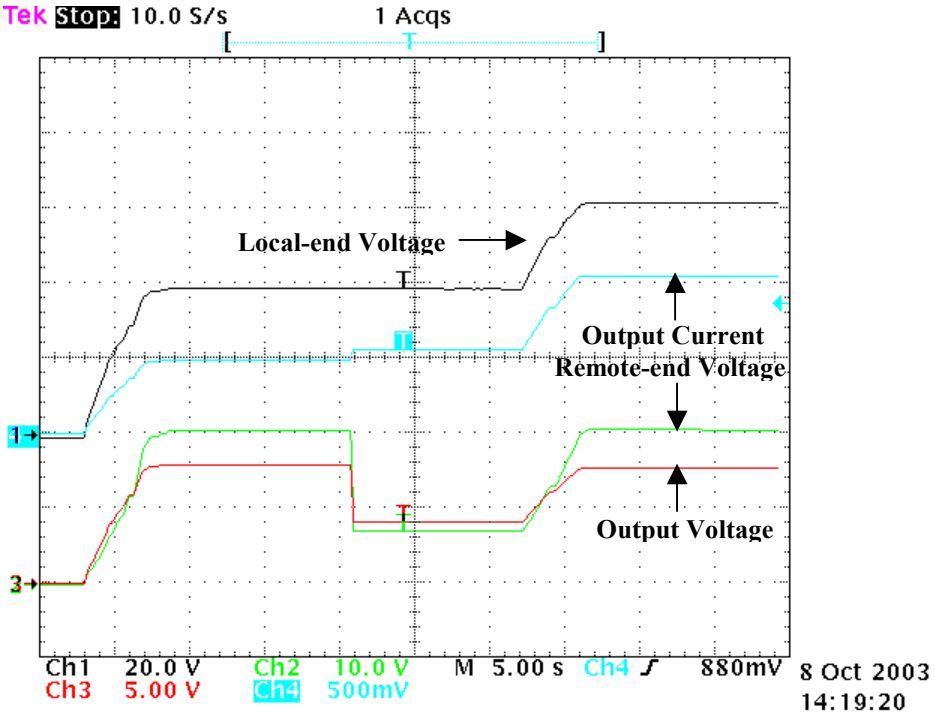

Figure 43: Voltage follower results (4W to 8 W transition)

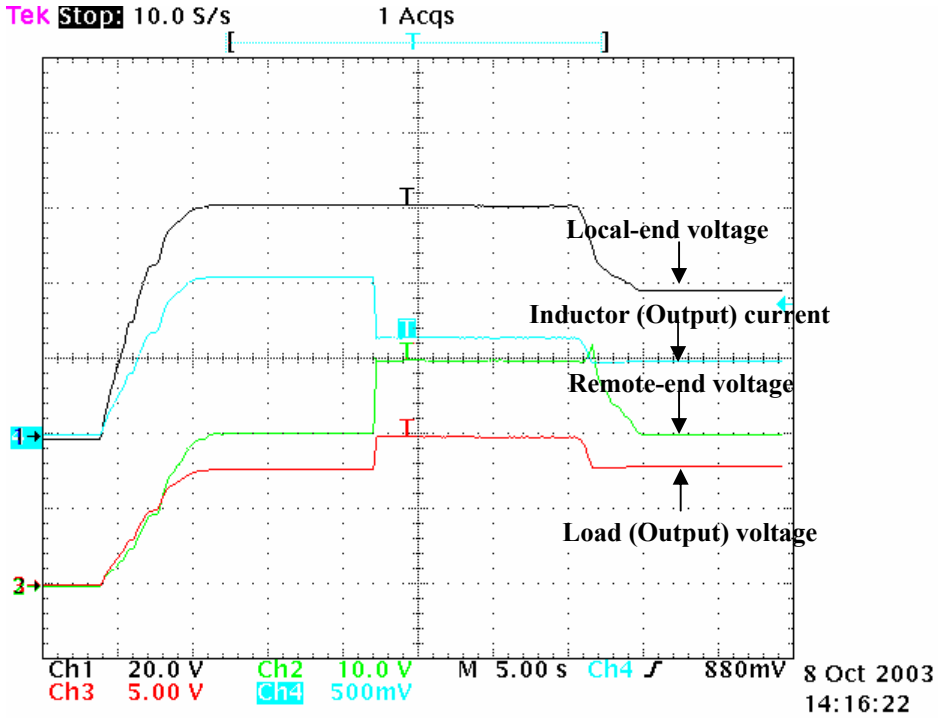

Figure 44: Voltage follower results (8 W to 4 W transition)

From the simulation and experimental results it is evident that an improvement in the power delivered and the elimination of remote-end voltage jumps during startup are the advantages of this method at the expense of the tight regulation of the output voltage. It can also be seen that load transients lead to jumps not only in the remote-end voltage but also in the output voltage. The power delivered during the load transient can be greater than the power demanded by the load when a significant portion of the load is turned off and the excess energy has to be dissipated as heat. This translates into requirements for higher voltage ratings for the post regulator.

4.2. Series regulator-switcher parallel operation with integrated control

A linear regulator has good stability properties while a switching regulator has high efficiency of operation. Operating these converters in parallel across the remote-end has the potential of achieving both properties simultaneously as shown in Figure 45. The series linear regulator appears as a resistive load across the remote-end voltage and reduces the effect of the constant power load behavior of the switcher. The parallel combination of series regulators and switching regulators has been used before in the design of high-efficiency audio amplifiers [35]. In these audio applications, the linear regulator is used to increase the fidelity of the amplifier, while the switcher is used to improve the efficiency of the system. In remote instrumentation applications with long cables, the linear regulator will be shown to improve the stability of the system, while the switching regulator ensures a high efficiency.

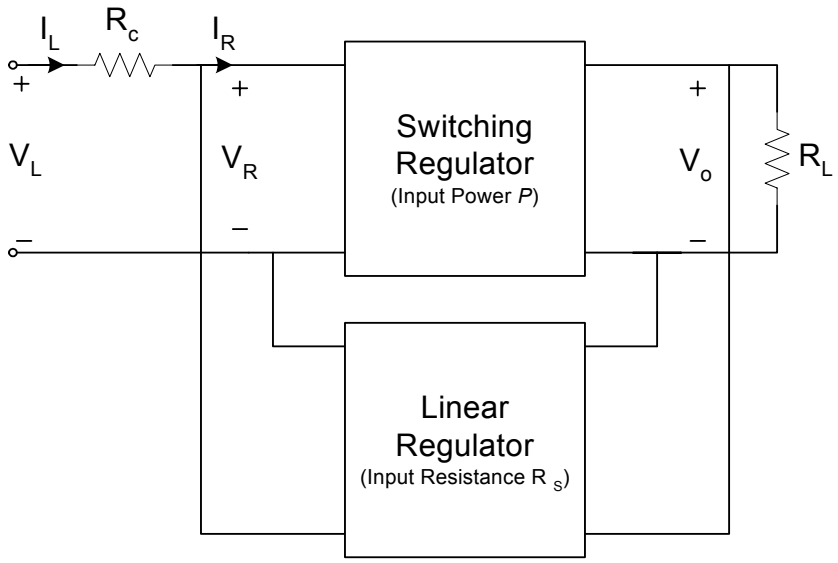

Figure 45: Series regulator-switcher parallel combination

4.2.1. Analysis

Consider, the method as shown in Figure 45 with R_S representing the series regulator input resistance and P the switcher power. The equation governing the dynamics of the system with a constant power load as stated earlier is given by:

$$\frac{dv_R}{dt} = \frac{1}{C}\left(\frac{V_L - v_R}{R_C} - \frac{P}{v_R} - \frac{v_R}{R_S}\right). \tag{25}$$

The stability of the system is ensured, when the criterion given by Equation (26) is satisfied by the remote-end voltage.

$$V_R > \sqrt{P\left(\frac{R_C R_S}{R_C + R_S}\right)} \text{ or } P < \frac{V_R^2}{\left(\frac{R_C R_S}{R_C + R_S}\right)} \tag{26}$$

It can be seen clearly that the series regulator stabilizes the system by modulating the cable resistance to a lower value thus enhancing the stable operating region of the system. The above criterion can be viewed as the corresponding remote-end voltage minimum with a pseudo-cable resistance that is the parallel combination of the linear regulator resistance and the actual cable resistance. Alternatively, Equation (26) can be rewritten to provide more insight into this solution.

$$P < \frac{V_R^2}{R_C} + \frac{V_R^2}{R_S} \tag{27}$$

It can be seen that beyond the stability limit of a pure switcher alone (see Equation (17)), which corresponds to the first term in the expression in Equation (27), for every watt input into the linear regulator, an additional watt can be input into the switcher. Hence, the switcher alone can be operated until the stability limit and then used in conjunction with the linear regulator leading to a reasonably high efficiency. As long as sufficient stability margin is ensured and voltage collapse is prevented by delivering power through the linear regulator, the system is stable and the transient response is not worsened.

The system curves for varying switcher powers and a linear regulator power of 75 W for an 800 Ω cable instrumentation system with a reference remote-end voltage of 330 V are shown in Figure 46. It can be seen that the minimum remote-end voltage required for each power level has been displaced from that of the ideal switcher (that is for a particular reference remote-end voltage, the power delivered through the switcher by the parallel combination is more than that of an ideal switcher operated alone). With an input power of 75W in the linear regulator, the switcher can now be operated at 200 W input power, which is a major improvement compared to that of a switcher alone (136 W). Note that the output power delivered would be the sum of the switcher and linear regulator powers scaled by their efficiencies.

The efficiency of the method will always be between the efficiencies of a pure switching regulator and a pure linear regulator. The efficiency of the combined method beyond the power delivery limit of an ideal switcher can be derived in terms of the power delivered (P_{out}) and the efficiencies of the switcher ($=\eta_S$) and the linear regulator ($=\eta_L$) as Equation (28).

$$\eta_{eff} = \left(\frac{\eta_L + \eta_S}{2}\right) \frac{1}{1 - \frac{V_R^2}{P_{out} R_C}\left(\frac{\eta_S - \eta_L}{2}\right)} \tag{28}$$

Hence, the parallel combination improves the power delivering capacity of the system at reasonably high efficiency (between those of a switcher and a linear regulator). Further, the variation of the remote-end voltage with the local-end voltage during system operation has been reduced as can be seen from Figure 46, which would lead to smaller

voltage jumps at startup. The remote-end voltage jumps at startup could also be eliminated by operating the linear regulator during startup and gradually transferring the power to the switcher.

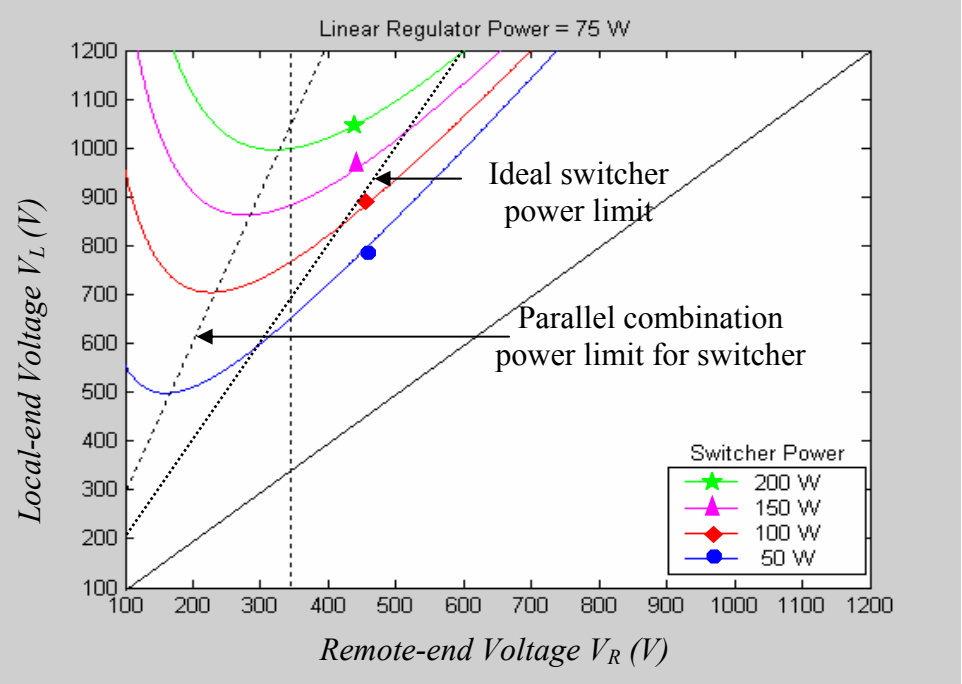

Figure 46: Variation of remote-end voltage with local-end voltage with series regulator-switcher parallel combination

The operation of the series and switching regulators in parallel is highly dependent on the distribution of power between them. It is not practical to have the two converters in parallel with their outputs unconnected delivering power to pre-determined loads. Not only does this lead to difficulties in practical implementation but also leads to increased component sizes. An integrated control method is developed to distribute the power between the series and switching regulator for optimal power delivery. In this method, the output voltage is controlled through the linear regulator while the allocation of power between the two parallel stages is controlled by the switcher. The switcher is operated under peak current mode control with the reference current being set to a known fraction of the load current. In practice, a micro-controller or a digital signal processor would be used to obtain the optimal fraction to ensure stability and high efficiency. This

implementation is recommended as an area for future work and more details are provided in Chapter VII. This method has the advantages of good and fast regulation with ripple free output voltage (as the output voltage is regulated by the linear regulator) leading to a decrease in the size of the filter elements in the switching regulator.

4.2.2. Simulation Results

An example system with a cable resistance of 800 Ω was simulated with SPICE with the control method explained above for illustrative purposes. The switcher and linear regulator were designed for an output power of 100 W each at a nominal output voltage of 50 V. The remote-end voltage was maintained near the nominal voltage of 300 V with a suitable choice of the local-end voltage. The linear regulator was used at start-up to avoid voltage jumps and the switching regulator was turned on at 75ms, after which, the power is shared between the two paralleled regulators. The load current delivered by the switcher was regulated by the peak current control method. The local-end voltage was ramped at an extremely fast rate during startup (35 V/ms) due to the varied time scales in the operation of the switching regulator (determined by the switching frequency) and the operation of the overall system. In practice, the local-end voltage would be ramped at much lower rates. The results obtained with this control method are shown in Figure 47. Further, the turning on of the switcher at time t=75 ms is smooth and does not lead to output current or voltage transients. Beyond time t= 75 ms, the switcher output ripple current is cancelled by the linear regulator current leading to a constant DC output current and almost ripple–free output voltage.

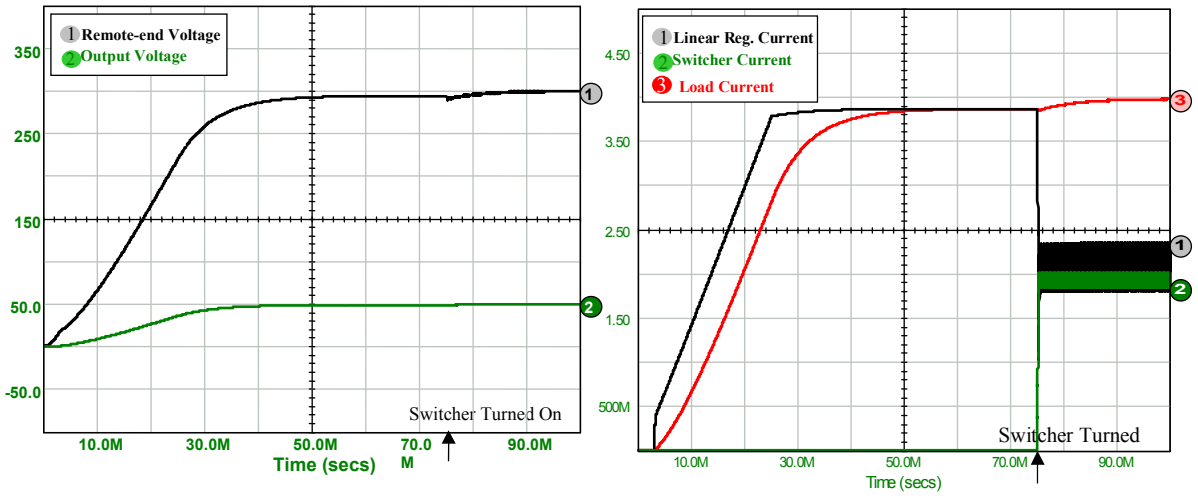

Figure 47: SPICE simulation results of linear regulator-switcher parallel method

4.2.3. Experimental setup

The linear regulator-switcher parallel method was implemented in a remote instrumentation system prototype with the remote-end voltage maintained at 20 V, an output voltage of 8 V and a cable resistance of 100 Ω. Note that the power limit for this system for an ideal switching converter at the remote end as explained in Chapter 3 would be given by:

$$P_{ideal,\max} = \frac{V_R^2}{R_C} = \frac{20^2}{100} = 4W \tag{29}$$

A buck converter operated under peak current mode control was used as the remote-end power converter. UC3524 current mode control IC was used to generate the PWM signals for controlling the converter. A pre-determined fraction of the load current based on the current capability of the cable is used to set the reference current level for the peak-current mode control of the inductor current. The series linear regulator implemented using a pass element was used to control the output voltage to 8V and also used at start-up to avoid voltage jumps. The proposed experimental setup for the verification of the series regulator-switcher parallel combination is shown in Figure 48.

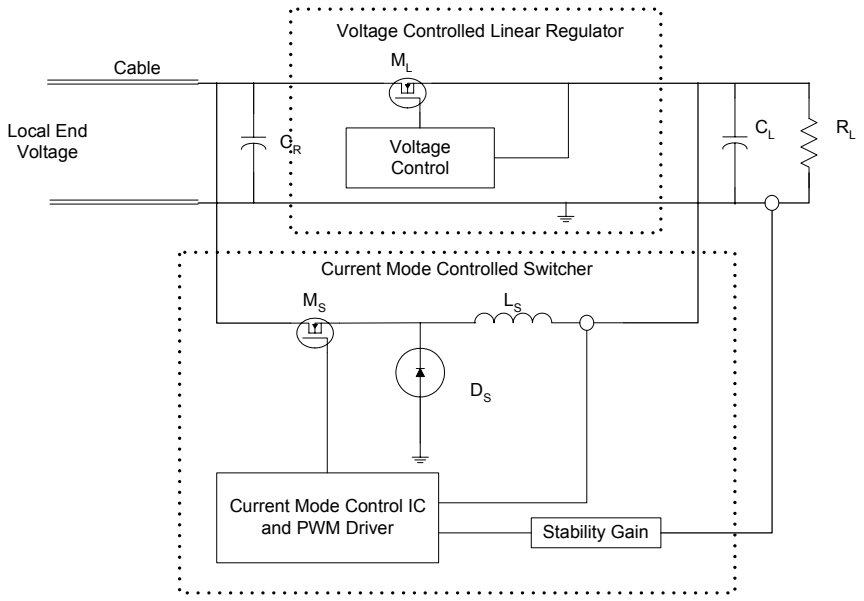

Figure 48: Experimental setup for linear regulator-switcher parallel method

4.2.4. Experimental results

The system behavior is illustrated in Figure 49-Figure 52 for different startup power levels and power distribution between the switching and linear regulator. Figure 49 shows the system startup behavior at a power level of 4 W. The system is started up with only the linear regulator leading to a smooth increase in remote-end voltage. The load voltage was stabilized at 8 V for an output current level of 0.5A corresponding to a power level of 4 W (which corresponds to the power limit of an ideal switcher). At time t=12s, the switching regulator is switched in with a current demand that results in almost equal sharing of power delivered between the linear and switching regulator. It is clear that there are no extraneous transients during the transfer of power between the two parallel units and the system is well regulated at an output voltage of 8 V. The equal sharing of power was done primarily to illustrate the ripple cancellation capability of this method. Figure 47 shows that the linear regulator compensates for the ripple current in the switcher and ensures a ripple-free and well-regulated output voltage. This is a key feature of this method as it leads to reduced component sizes for the inductor and capacitor in the switching circuit.

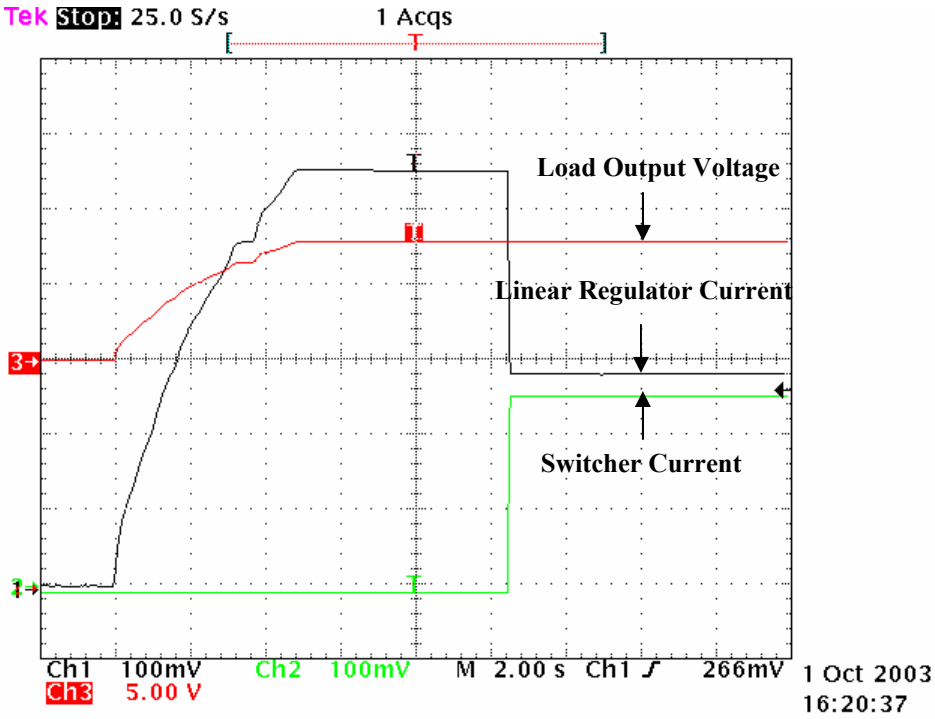

Figure 49: Linear regulator-switcher parallel method results

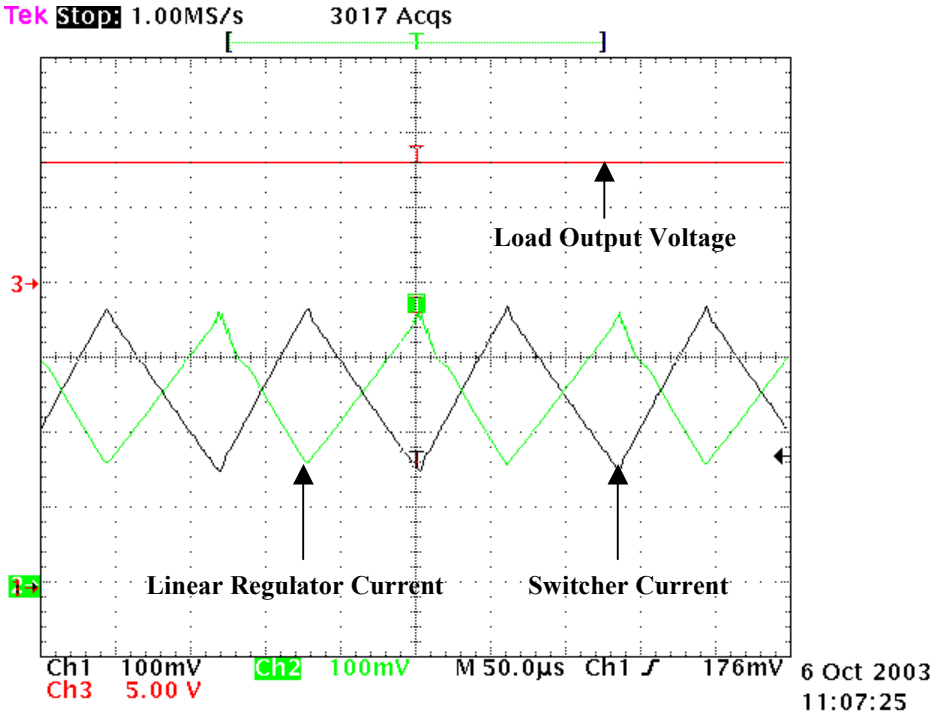

Figure 50: Linear regulator-switcher parallel method results (Load power = 4 W)

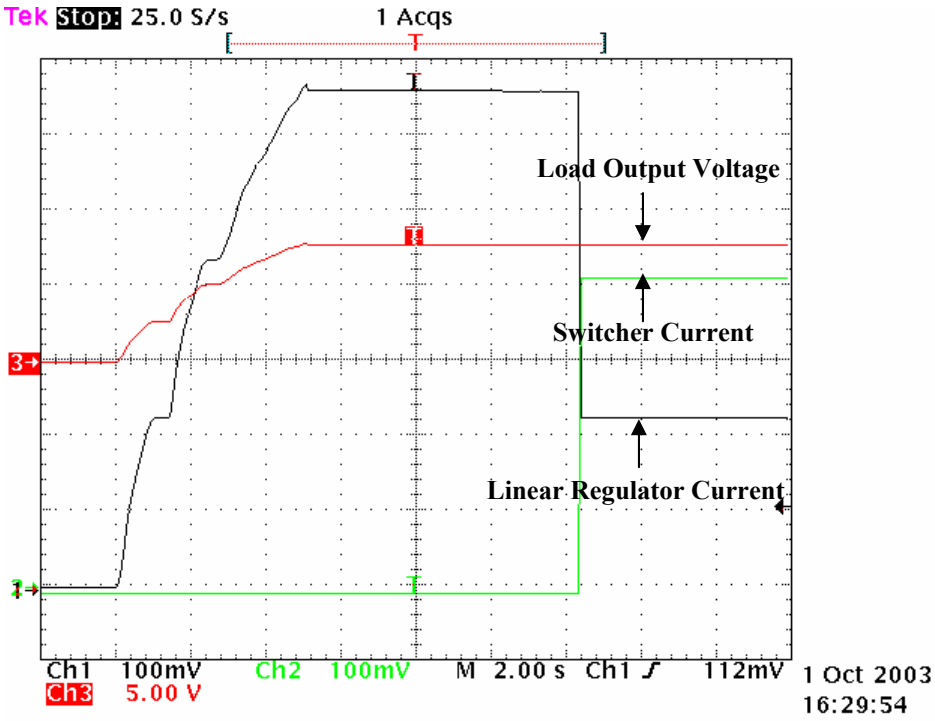

Figure 51: Linear regulator-switcher parallel method results (Load Power = 6 W)

The experiments were repeated now with an output power level of 6 W (which is beyond the 4 W maximum power limit of an ideal switcher). Figure 51 and Figure 52 show the startup behavior with two different power allocations once the switching regulator is turned on. From the experimental results it is clear that the system starts up for an output current level of 0.75A and an output voltage of 8V corresponding to a power level of 6W. The switching regulator was turned on at 14s, after which, the power is shared between the two paralleled regulators. Notice that beyond time t=14s in Figure 52, the bulk of the power is being delivered through the switching regulator and the linear regulator only compensates for the ripple current through the switching regulator. The system has been stabilized in this case at a power level of 6W that is beyond the maximum power limit of an ideal switcher (4W for this prototype system) retaining high efficiency.

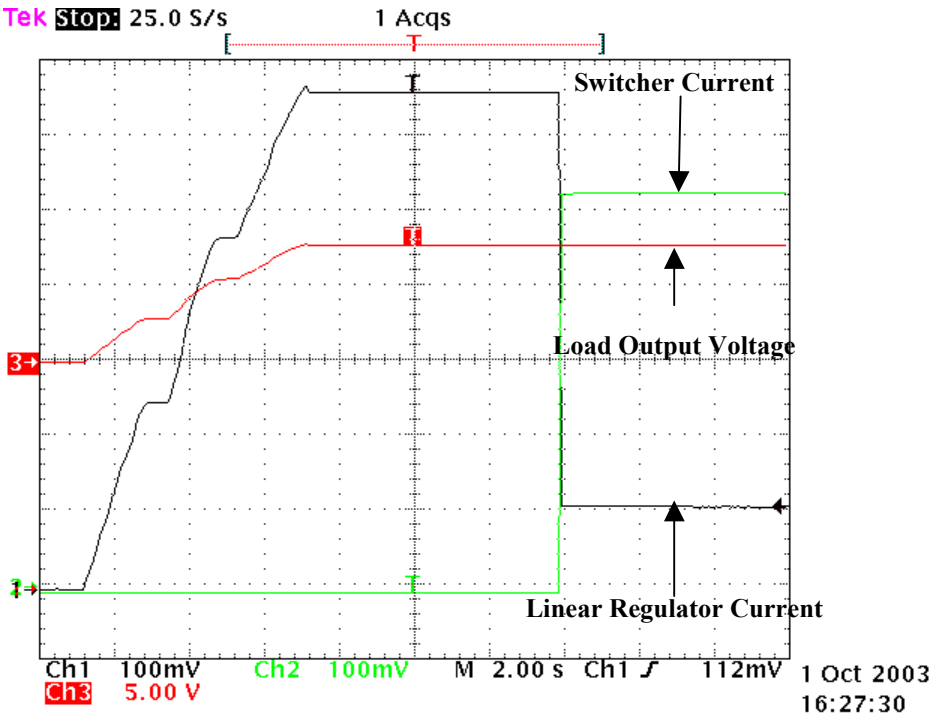

Figure 52: Linear regulator-switcher parallel method results (Load Power = 6 W)

The impact of load changes on the output voltage regulation was also studied. Figure 53 shows the system waveforms for a load change from 8 W to 4 W. Only the load current, that is the sum of the switcher and linear regulator currents, is shown for clarity. It is clear that the output voltage is regulated at 8 V while the remote-end voltage rises above 20 V when the load is changed from 8 W to 4 W at time t=22s. Unlike the state feedback based voltage follower method where the output voltage "*follows*" the remote-end voltage, the load voltage is regulated even during load changes.

The above experiments were performed for a given cable, and a simple feedback of a fraction of the load current as the reference current for the switching regulator was performed. To optimize the efficiency of the system for a given cable, a lookup table can be used to determine the appropriate power allocation between the two parallel units. With the above mentioned lookup table like approach, the number of current sensors can be reduced to one in the absence of protection units thus bringing down the cost of the unit. For universal usage with different cable lengths, a microprocessor-based or digital signal processor-based control is essential for implementation of this method. The

parallel combination method is superior with respect to the state feedback based voltage follower method in terms of the voltage regulation capability and sizing of switching converter filter components. The main disadvantage of this method is the increase in components due to the additional linear regulator.

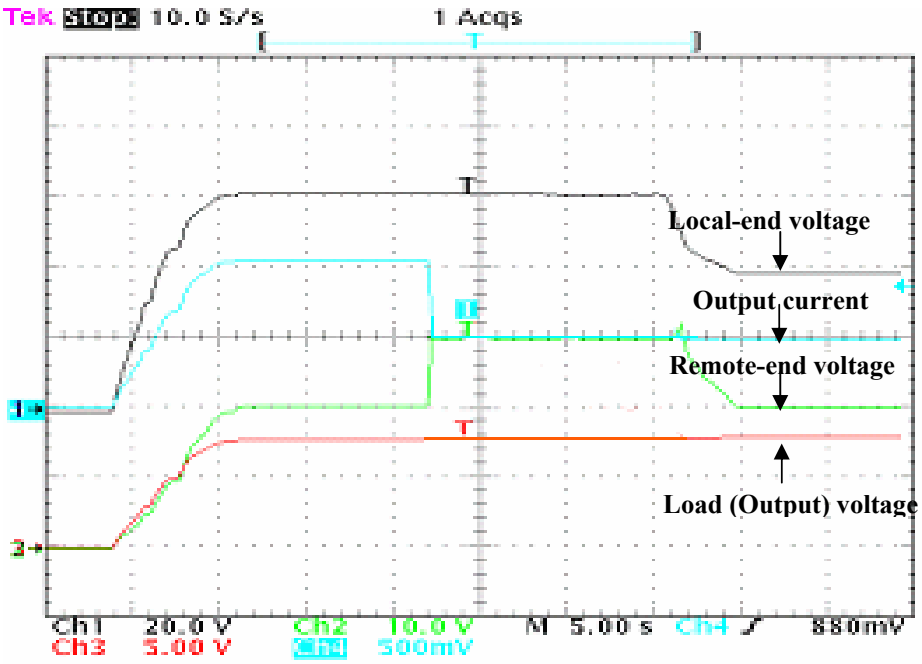

Figure 53: Linear regulator-switcher parallel method load change results

4.3. Conclusions

In this chapter, two new remote power conversion methods that alleviate the drawbacks of the current primary methods namely, linear and switching regulators were developed, analyzed and validated experimentally. The two new methods are based on voltage followers using state feedback and integrated parallel combination of linear and switching regulators with integrated control. The trade-offs between the two methods lie in the increased component count of the parallel method to the reduced regulation capability of the voltage follower method. Both methods were theoretically analyzed and experimentally proven to be capable of delivering power beyond the maximum limits of an ideal switcher when the system is operated at sub-optimal (that is, less than half the maximum local-end voltage limit) remote-end voltages.

CHAPTER 5

TRANSMISSION LINE MODELING

As mentioned in Chapter 2, simple but accurate cable models are required for the real-time control of the system. Previous transmission line models have been primarily oriented towards accurate simulation of voltage transients and not towards the generation of a model for real-time control [27]- [33]. Most of these methods are based on extensive computations and are not suitable for usage in real-time control of the remote-end voltage. This chapter reviews a model based on a Padé approximation of the transmission line solution. Due to the unsuitability of this approach, a modeling approach based on an s-domain rational approximation of two-port transfer functions is developed that leads to a simpler model and retains the accuracy of the previous approaches.

5.1. Transmission Line Basics

The general transmission line equations can be given by:

$$\begin{aligned} \frac{\partial}{\partial x}\mathbf{v}(x,t) &= -R\mathbf{i}(x,t) - L\frac{\partial}{\partial t}\mathbf{i}(x,t) \\ \frac{\partial}{\partial x}\mathbf{i}(x,t) &= -G\mathbf{v}(x,t) - C\frac{\partial}{\partial t}\mathbf{v}(x,t) \end{aligned} \tag{30}$$

where v refers to the voltage at any point along the line, i refers to the current through that point on the line, R the per-unit resistance of the line, L the per-unit inductance of the line, G the per-unit conductance of the line and C the per-unit capacitance of the line. Note that at this point we have not made a distinction to whether the per-unit parameters are constant or frequency dependent. The solution of the transmission line equation in the frequency domain can be obtained by integrating with respect to x the partial differential equation as shown below:

$$\begin{bmatrix} \mathbf{V}_R(s) \\ -\mathbf{I}_R(s) \end{bmatrix} = e^{\begin{bmatrix} 0 & -(R(s)+sL(s)) \\ -(G(s)+sC(s)) & 0 \end{bmatrix} l} \begin{bmatrix} \mathbf{V}_L(s) \\ \mathbf{I}_L(s) \end{bmatrix} \tag{31}$$

where l refers to the length of the line, V_L and I_L refer to the voltage and current at the local-end (input end) of the cable, and V_R and I_R refer to the voltage and current at the remote-end (output end) of the cable. Note that the upper case letters are used for Laplace transformed variables and smaller case letters are used for instantaneous time values. Figure 54 shows the conventions used for the directions of voltage and current respectively.

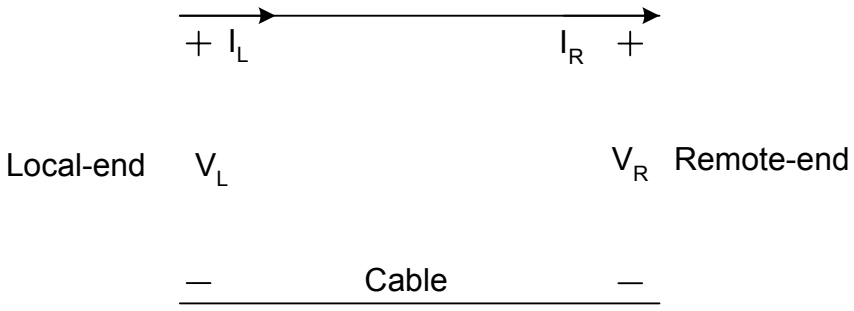

Figure 54: Transmission Line

There are two possible avenues of modeling the system based on Equation (31). In previous approaches [27], the exponential in the equation has been expanded through Padé approximations and the transmission line can be sectioned into segments. This method will be explored through simulations and experiments in the next section. Alternatively, the exponential could be computed from the data at each frequency point and the resulting data could be approximated by s-domain transfer functions. This forms the basis for the new model developed and will be analyzed in detail later in this chapter.

5.2. Padé Approximant modeling

The solution to the transmission line Equation (31) can be evaluated by approximating the R-L-G-C parameters by rational s-domain functions from the experimental data and then approximating the resulting exponential by Padé approximations [28]. This approach was evaluated due to the ease of translating the system into SPICE for transient analysis.

First, the series (R+sL) and parallel (G+sC) impedances are approximated as rational functions in the s-domain from the experimental data. It is assumed that the per-unit impedances can be obtained through short and open-circuit tests or impulse function

tests [33]. Second, the exponential function is approximated by Padé rational functions. Padé functions are simple rational expansions of the exponential function. For example, a simple first order expansion of e^{-z} can be given to be:

$$e^{-z} = \frac{1-\frac{z}{2}}{1+\frac{z}{2}} \tag{32}$$

For better accuracy, the N[th] order Padé approximation given below is used.

$$\begin{aligned} &P_N(z)e^z = Q_N(z); N > 0; \\ &P_N(z) = \sum_{j=0}^{N} \frac{(2N-j)!N!}{(2N)!\, j!(N-j)!}(-z)^j \;\; ; \;\; Q_N(z) = \sum_{j=0}^{N} \frac{(2N-j)!N!}{(2N)!\, j!(N-j)!}(z)^j \end{aligned} \tag{33}$$

Notice that the zeros of P_n are the negative of the zeros of Q_n giving a special structure to the approximation so that it can be split into sub-sections comprising either complex pole-zero pairs when N is even, or complex and real pole-zero pairs when N is odd.

A circuit equivalent for each subsection can now be determined easily. For the case when N is even, the transmission line sub-section can be approximated as in Figure 55. The values of the parameters involved in the transmission line sub-section are dependent on the number of sections (which determines the poles and zeros in the Padé approximation) and the R-L-G-C parameters of the transmission line. For a particular pole $(x+jy)$ in the Padé approximation and an even Padé order, the values of the internal elements in the Padé sub-section are given as:

$$\begin{aligned} &R_1 = \frac{l}{x}R; L_1 = \frac{l}{x}L; R_g = \frac{x^2+y^2}{xl}\frac{1}{G}; C_g = \frac{xl}{x^2+y^2}C; \\ &C_a = -\frac{l}{4x}C; C_b = C_c = \frac{l}{2x}C; \\ &R_{a1} = -\frac{4xl}{x^2+y^2}R; R_{a2} = \frac{2xl}{x^2+y^2}R; L_a = \frac{4xl}{x^2+y^2}L \end{aligned} \tag{34}$$

where R is the per-unit resistance of the line, L the per-unit inductance of the line, G the per-unit conductance of the line, C the per-unit capacitance of the line and l the length of the line.

The case when N is odd is more complex as it leads to a real pole in addition to complex poles. More information on this modeling procedure and can be obtained from

[28]. Note that this procedure in developing the sub-sections is different from just creating lumped segments using the per-unit values of R-L-G-C. The new model sub-sections might have internal nodes to take into account the frequency dependence of the transmission line parameters. Also, each of the sub-sections is identical in structure but differ in the actual values of the elements depending on the roots of the Padé polynomial.

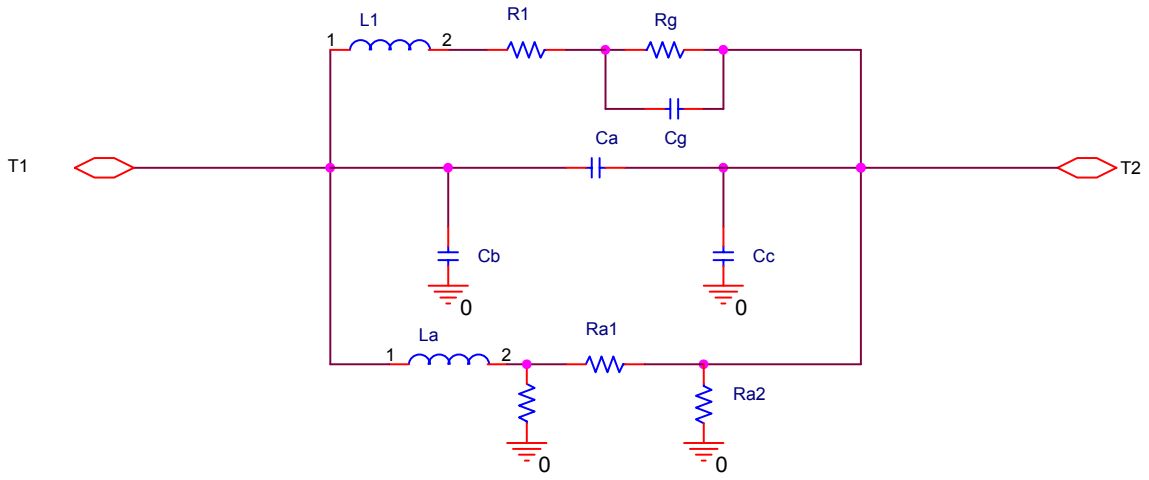

Figure 55: Transmission line sub-section

5.2.1. Cable parameters and approximation

A typical wireline logging cable used for oil logging was used for evaluating the transmission line model and was characterized using short and open-circuit data. The experimentally obtained short and open-circuit data for the cable were converted to the per-unit impedance parameters, namely R-L-G-C. The experimentally obtained per-unit impedances of the cable referred hereafter as Cable-1 are shown in Appendix A. As a first approximation, the per-unit impedance parameters were fitted by constant frequency elements and the fitting is shown in Figure 56 and Figure 57. The constant parameters for this particular cable arrangement were R=22.35 Ω/Kft.; L=0.4 mH/Kft.; G= 0.05 μS/Kft.; C=28.5 nF/Kft. The discrepancies between the fitted and the experimental data at low frequencies are due to suspect data and power line interference. The discrepancies at high frequencies are due to the approximation of constant cable parameters.

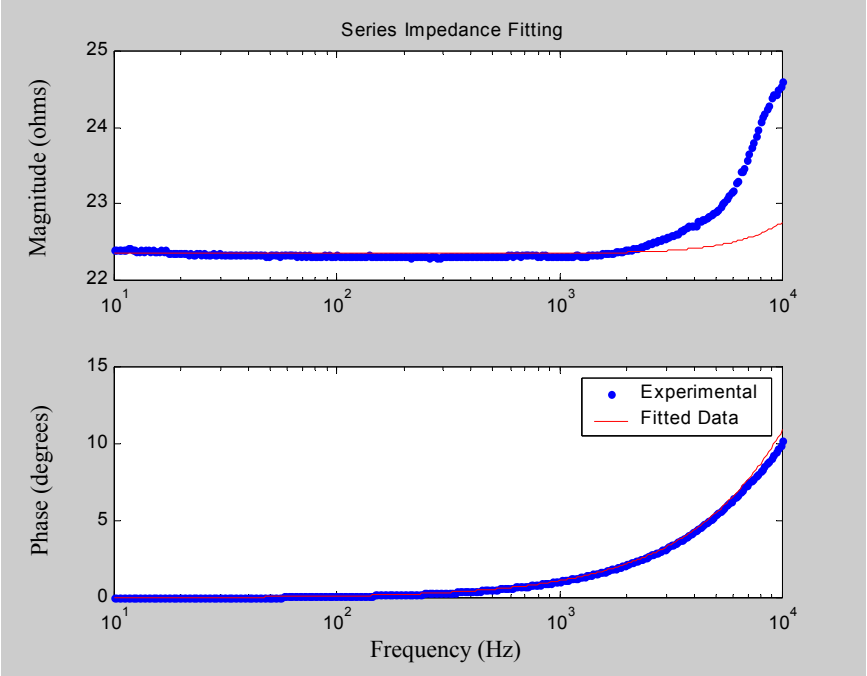

Figure 56: Series Impedance (R+sL) Fitting for Cable-1

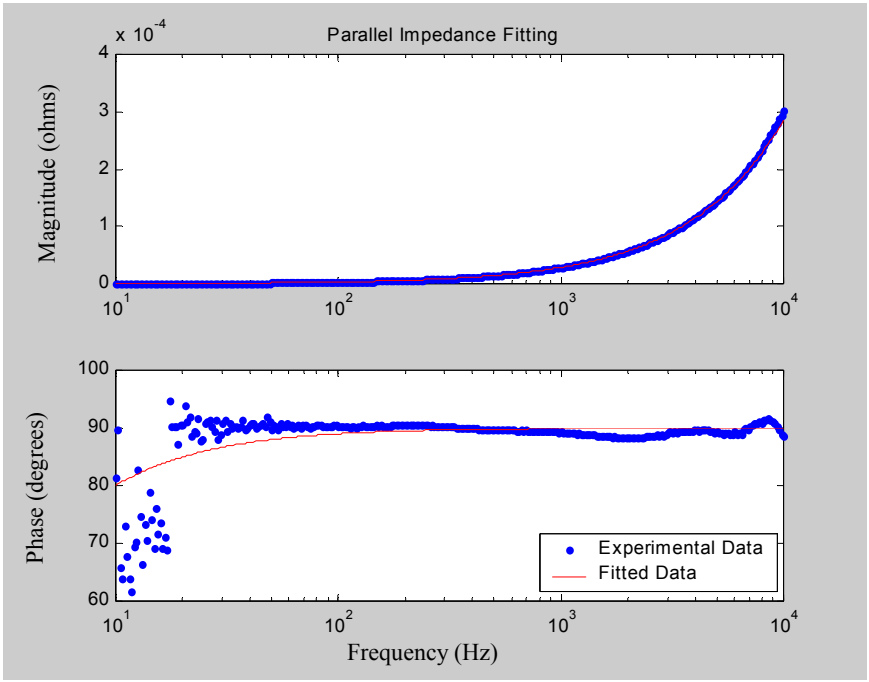

Figure 57: Parallel Impedance (G+sC) Fitting for Cable-1

5.2.2. Simulation comparison with experimental results

The primary application of the cable model developed in the previous section involves the switching of the loads at the remote-end of the cable. With this intent in mind, the cable model was compared with experimental results with a constant voltage at the local-end and the load resistance at the remote-end (other end of the cable) being constantly switched between two different values. The experimental setup shown in Figure 58 consists of a constant DC input voltage of 5V at one end of the cable and a resistive load that switches between a base load of 5.11 kΩ and a switched load of 640 Ω (5.11 kΩ in parallel with 732 Ω) that corresponds approximately to the cable DC resistance of Cable-1. When the heavy load is switched on, the remote-end voltage should reach a steady state voltage close to half the input voltage of 5V (i.e. the system forms a resistive divider with the cable impedance equal to the load impedance).

A comparison of the experimental and simulated remote-end voltage responses obtained using SPICE is shown in Figure 59 and Figure 60. The experimental results show two phenomena during the switching process: one, the delay aspect of the line leading to the almost instantaneous rise or fall in load voltage immediately after the instant of switching (approximately 0.8 V in Figure 59) and two, the energy storage aspect of the line that can be observed in the dynamics of the load voltage in reaching the steady state voltages in approximately 800 μs in Figure 59. It can be noted that the model replicates the experimental waveforms except for high frequency ringing at the switching instants.

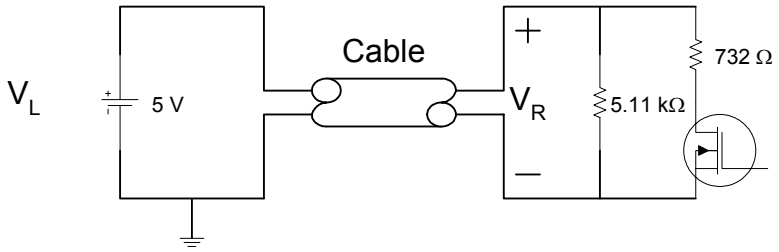

Figure 58: Experimental setup for verifying cable model

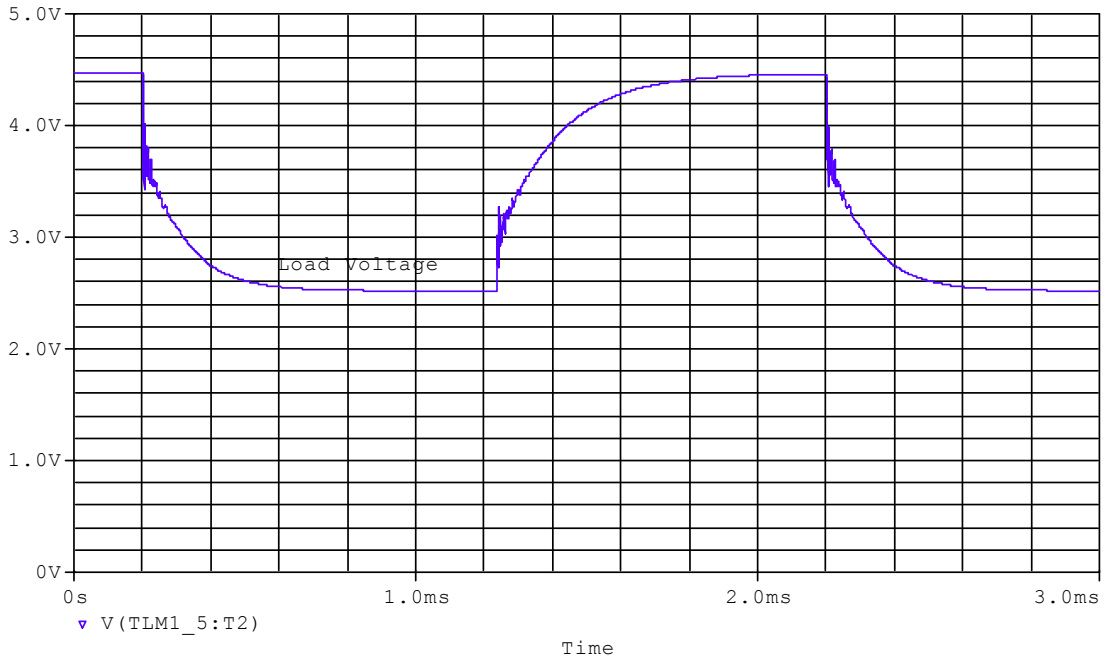

Figure 59: Simulated remote-end voltage response with 5.11 kΩ base load and 640 Ω switched on/off

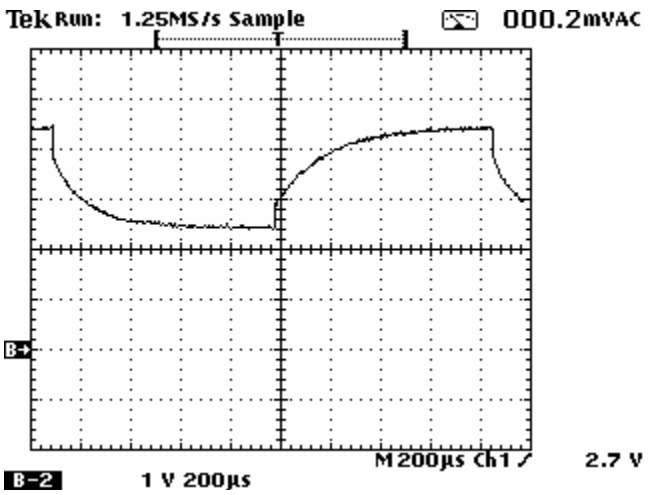

Figure 60: Experimental remote-end voltage response with 5.11 kΩ base load and 640 Ω switched on/off

The experiments were also performed without a base load and a load of 732 Ω periodically switched on or off. In this case, the worst case scenario of an open-circuited transmission line is tested for model accuracy. A comparison of the experimental and

simulated remote-end voltage responses obtained using SPICE is shown in Figure 61 and Figure 62. The circuit model replicates the experimental waveforms except for more pronounced high frequency ringing at the switching instants.

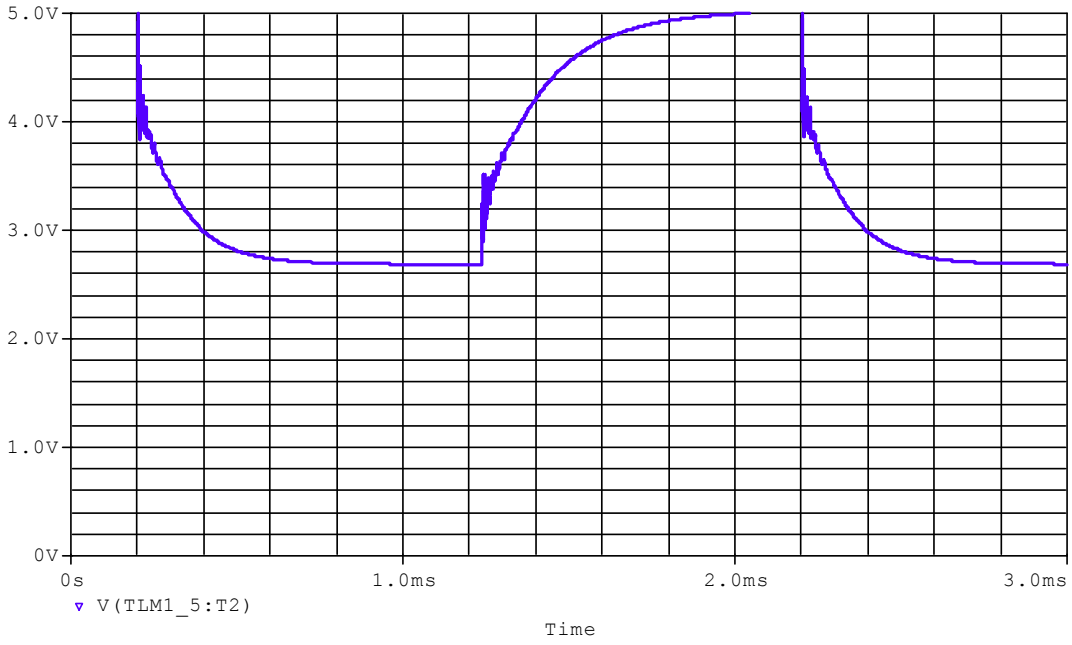

Figure 61: Simulated remote-end voltage response with 732 Ω switched on/off

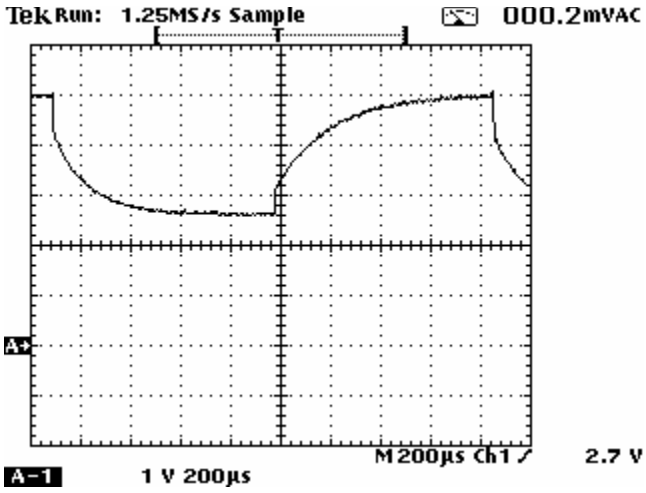

Figure 62: Experimental remote-end voltage response with 732 Ω switched on/off

5.2.3. Inadequacies of this approach

The inadequacies of this approach towards transient simulation mainly stem from the need for increasing number of segments for increased accuracy. The presence of frequency dependent R-L-G-C elements leads to large number of nodes in each segment leading to SPICE convergence issues. It was also observed during the simulations that the high frequency oscillations at the instant of switching could not be removed without reducing the number of segments thereby trading off the accuracy of the simulation. This difficulty is inherent in the modeling of transmission lines by high-order segmented models. Also, a comparison of Figure 59 and Figure 60 shows that the load voltage waveforms differ slightly in the rise and fall times.

Further, the inherent nature of Padé approximations leads to a difficult transformation into the real world of a circuit simulator for the cable (which is our final objective in trying to regulate the remote-end voltage by obtaining an accurate cable model). The presence of negative capacitor elements and the size of the circuit complicate the conversion to an analog circuit simulator for the cable. Note that for increased accuracy, we need to use a large number of segments such as that shown in Figure 55. Even with fast digital signal processors (DSPs), the computations required for good accuracy would be large and also lead to time delays in the control due to the processing time.

5.3. Transfer Function Modeling

A modeling approach based on a s-domain rational approximation of two-port transfer functions is developed in the next section that leads to a simpler model and retains the accuracy of the previous approaches. The exponential in the transmission line solution is computed from the data at each frequency point and the resulting data is approximated by s-domain transfer functions to obtain the new model.

5.3.1. Modeling Approach

A two-port model with Y- elements (shunt-type) can be obtained by reconfiguring the matrix in Equation (31) to the appropriate form as below with the exponential terms pre-calculated through the experimental data:

$$\begin{bmatrix} \mathbf{I}_L(s) \\ \mathbf{I}_R(s) \end{bmatrix} = \begin{bmatrix} Y_{11}(s) & Y_{12}(s) \\ -Y_{12}(s) & -Y_{11}(s) \end{bmatrix} \begin{bmatrix} \mathbf{V}_L(s) \\ \mathbf{V}_R(s) \end{bmatrix} \tag{35}$$

Note that there are only two frequency dependent functions that model the cable completely due to the symmetrical nature of the cable. The frequency dependent admittances can also be obtained from the short and open-circuit impedances of the cable rather than using the per-unit impedances of the cable as:

$$\begin{aligned} Y_{11}(s) &= \frac{1}{Z_{sc}} \\ Y_{12}(s) &= \frac{1}{Z_{sc}} \sqrt{\frac{Z_{oc} - Z_{sc}}{Z_{oc}}} \end{aligned} \tag{36}$$

The Y-parameter functions obtained are then approximated by rational s-domain functions. The only assumption made in the approximation is that only stable poles (left-half plane poles) are allowed. Non-minimum phase zeros (right-half plane zeros), if necessary in the case of phases less than -180°, are also allowed. This ensures the stability of the system and allows ease of modeling time delays inherent in the transmission line equations.

Assume the Y-parameter functions can be approximated as below:

$$\begin{aligned} Y_{11}(s) &= A_1 + \sum_i \frac{B_{1i}}{(s + p_{1i})} \\ Y_{12}(s) &= A_2 + \sum_i \frac{B_{2i}}{(s + p_{2i})} \end{aligned} \tag{37}$$

From this frequency domain representation, a time-domain state-space macro-model for the cable can be obtained easily [33], [36]-[37]. Consider for example, the simple case with Y-parameter functions represented by single poles as shown below:

$$\begin{aligned} Y_{11}(s) &= A_1 + \frac{B_1}{(s + p_1)} \\ Y_{12}(s) &= A_2 + \frac{B_2}{(s + p_2)} \end{aligned} \tag{38}$$

Looking at Equation (35), we can see that the input current (I_L) is obtained by multiplying the input voltage (V_L) by Y_{11} and the output voltage (V_L) by Y_{12}. Now the term, Y_{11} V_L can be represented by a single pole and implemented as a first order differential equation with the input to the state variable being V_L. Doing the same for Y_{12} V_R, we obtain the

model for the input current I_L. Extending the above procedure for the output current I_R, the state space realization with four state variables obtained is shown below:

$$\dot{\mathbf{x}} = \begin{bmatrix} \dot{x}_1 \\ \dot{x}_2 \\ \dot{x}_3 \\ \dot{x}_4 \end{bmatrix} = \begin{bmatrix} -p_1 & 0 & 0 & 0 \\ 0 & -p_2 & 0 & 0 \\ 0 & 0 & -p_1 & 0 \\ 0 & 0 & 0 & -p_2 \end{bmatrix} \begin{bmatrix} x_1 \\ x_2 \\ x_3 \\ x_4 \end{bmatrix} + \begin{bmatrix} 1 & 0 \\ 0 & 1 \\ 0 & 1 \\ 1 & 0 \end{bmatrix} \begin{bmatrix} v_L \\ v_R \end{bmatrix}$$

$$\mathbf{y} = \begin{bmatrix} i_L \\ i_R \end{bmatrix} = \begin{bmatrix} B_1 & B_2 & 0 & 0 \\ 0 & 0 & -B_1 & -B_2 \end{bmatrix} \begin{bmatrix} x_1 \\ x_2 \\ x_3 \\ x_4 \end{bmatrix} + \begin{bmatrix} A_1 & A_2 \\ -A_2 & -A_1 \end{bmatrix} \begin{bmatrix} v_L \\ v_R \end{bmatrix} \tag{39}$$

When the load is connected to the cable at the remote-end, an interconnected system that is dependent on the sub-systems (load and cable) is obtained. The overall system dynamics and also the interconnection relations (if any) need to be obtained for simulation of the system. As explained above, the frequency domain experimental cable data can be converted into a state space model:

$$\text{Cable Model:} \quad \begin{aligned} \dot{\mathbf{x}}_C &= A_C x_C + B_{C1} v_L + B_{C2} v_R \\ \mathbf{y}_C &= \begin{bmatrix} i_L \\ i_R \end{bmatrix} = \begin{bmatrix} C_{C11} x_C + D_{C11} v_L + D_{C12} v_R \\ C_{C21} x_C + D_{C21} v_L + D_{C22} v_R \end{bmatrix} \end{aligned} \tag{40}$$

A state-space model can also be derived for the load and filters on the remote-end with the input to the load as the output voltage of the cable and the load current as an output as below:

$$\text{Load Model:} \quad \begin{aligned} \dot{\mathbf{x}}_L &= A_L x_L + B_L v_R \\ \mathbf{y}_L &= i_R = C_L x_L + D_L v_R \end{aligned} \tag{41}$$

With this load model, the system model can be reformulated with a boundary condition on the load current (i_R) when the system is interconnected (i.e. the load current derived from the cable model must be equal to the load current derived from the load model). The system model for the cable-load interconnected system can now be represented as:

$$\dot{\mathbf{x}} = \begin{bmatrix} \dot{x}_C \\ \dot{x}_L \end{bmatrix} = \begin{bmatrix} A_C & 0 \\ 0 & A_L \end{bmatrix} \begin{bmatrix} x_C \\ x_L \end{bmatrix} + \begin{bmatrix} B_{C1} & B_{C2} \\ 0 & B_L \end{bmatrix} \begin{bmatrix} v_L \\ v_R \end{bmatrix}$$

$$\text{Cable-Load Model: } \mathbf{y} = \begin{bmatrix} i_1 \\ i_2 \end{bmatrix} = \begin{bmatrix} C_{C11}x_C + D_{C11}v_L + D_{C12}v_R \\ C_{C21}x_C + D_{C21}v_L + D_{C22}v_R \end{bmatrix} \tag{42}$$

$$v_R = \left(D_L - D_{C22}\right)^{-1}\left(C_{C21}x_C - C_L x_L + D_{C21}v_L\right)$$

With the above state-space realization, the system can be simulated in MATLAB or any other state-space differential equation solver.

5.3.2. Model parameters and frequency domain rational function approximation

The same wireline logging cable mentioned earlier in the previous method was used for validating the transmission line model and was characterized using short and open-circuit data. The experimentally obtained short and open-circuit data for the cable shown in Appendix A were converted to the model parameters, namely Y_{11} and Y_{12}. $Y_{11}(s)$ and $Y_{12}(s)$ were numerically fitted by pole-zero approximations. Y_{11} was approximated by a 1-pole/1-zero rational function as shown below:

$$Y_{11}(s) = \frac{1}{671.6}\left(\frac{1+\frac{s}{5026.5}}{1+\frac{s}{25761.1}}\right) \tag{43}$$

Note here that $Y_{11}(s)$ is the reciprocal of the short circuit impedance (Z_{sc}) as stated in the previous section leading to the conclusion that we have a cable with a DC resistance of approximately 672 Ω between the ends. Figure 63 compares the numerical fit to the experimental data for $Y_{11}(s)$. The admittance amplitudes are shown in logarithmic scale ($20*\log_{10}$) since the numerical fitting procedure was performed using a log-log-scale. The variation in impedance between low and high frequencies was high leading to errors in the fitting if done using normal scales. The log-log scale reduces the variation in the fitting due to the logarithmic weighting and also gives a better perspective of the transfer functions in terms of poles and zeros.

$Y_{12}(s)$ was approximated by a 7-pole/7-zero rational function shown below:

$$Y_{12}(s) = \frac{-1}{671.6}\left(\frac{1+\frac{s}{188495.6}}{1+\frac{s}{50265.5}}\right)\left(\frac{1-\frac{s}{37699.1}}{1+\frac{s}{37699.1}}\cdot\frac{1-\frac{s}{113097.3}}{1+\frac{s}{113097.3}}\cdot\frac{1-\frac{s}{125663.7}}{1+\frac{s}{125663.7}}\right)\cdot \left(\frac{1-\frac{s}{314159.3}}{1+\frac{s}{314159.3}}\cdot\frac{1-\frac{s}{408407.0}}{1+\frac{s}{408407.0}}\frac{1-\frac{s}{565486.7}}{1+\frac{s}{565486.7}}\right) \quad (44)$$

Figure 64 compares the numerical fit vis-à-vis the experimental data for $Y_{12}(s)$. Notice that the phase of $Y_{12}(s)$ keeps decreasing with frequency indicating the dispersion aspect of the transmission line. Since, the magnitude of $Y_{12}(s)$ seems to indicate a single pole roll-off in the frequencies between 100-10 kHz, $Y_{12}(s)$ was fitted using non-minimum phase zeros (right half plane zeros) and stable poles that cancel out in the magnitude response but lead to a decreasing phase with frequency. Note that this is similar to the approximation of a time delay into a rational function approximation.

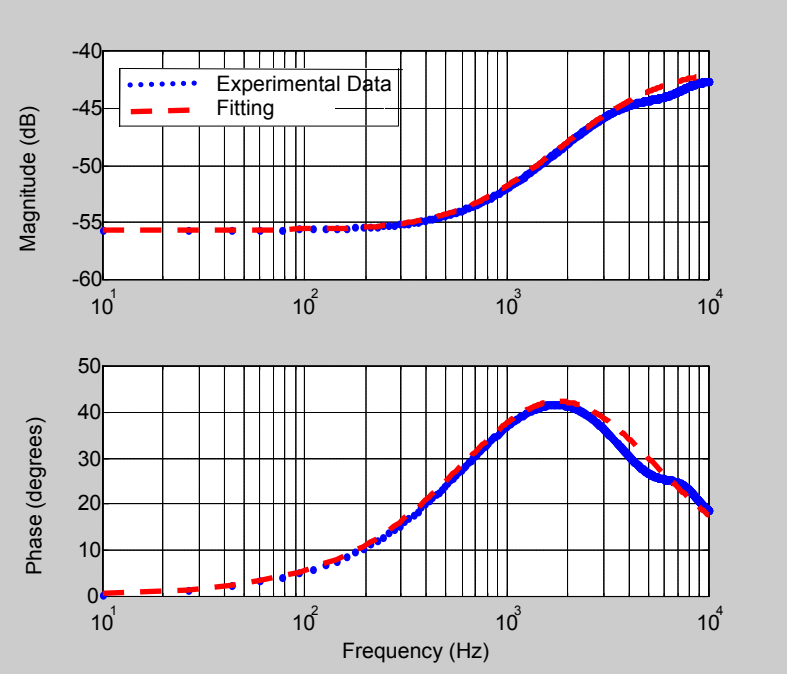

Figure 63: Y_{11} fitting for Cable-1

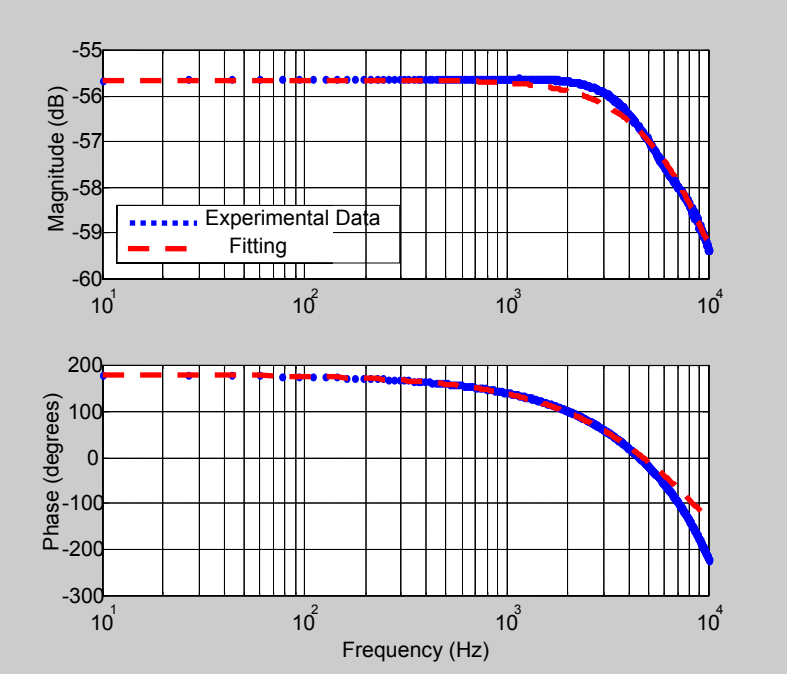

Figure 64: Y_{12} fitting for Cable-1

5.3.3. Comparison of experimental and simulation results

The cable model was compared with experimental results with a constant voltage at the local-end and the load resistance at the remote-end (other end of the cable) being constantly switched between two different values as in the validation for the previous method. The same experimental setup shown in Figure 58 consisting of a constant DC input voltage of 5 V at one end of the cable and a resistive load that switches between a base load of 5.11 kΩ and a switched load of 670 Ω (approximately the cable DC resistance) is also used in this case. When the heavy load is switched on, the remote-end voltage should reach a steady state voltage close to half the input voltage of 5V (i.e. the system forms a resistive divider with the cable impedance equal to the load impedance). A comparison of the experimental and simulated remote-end voltage responses obtained using MATLAB is shown in Figure 65.

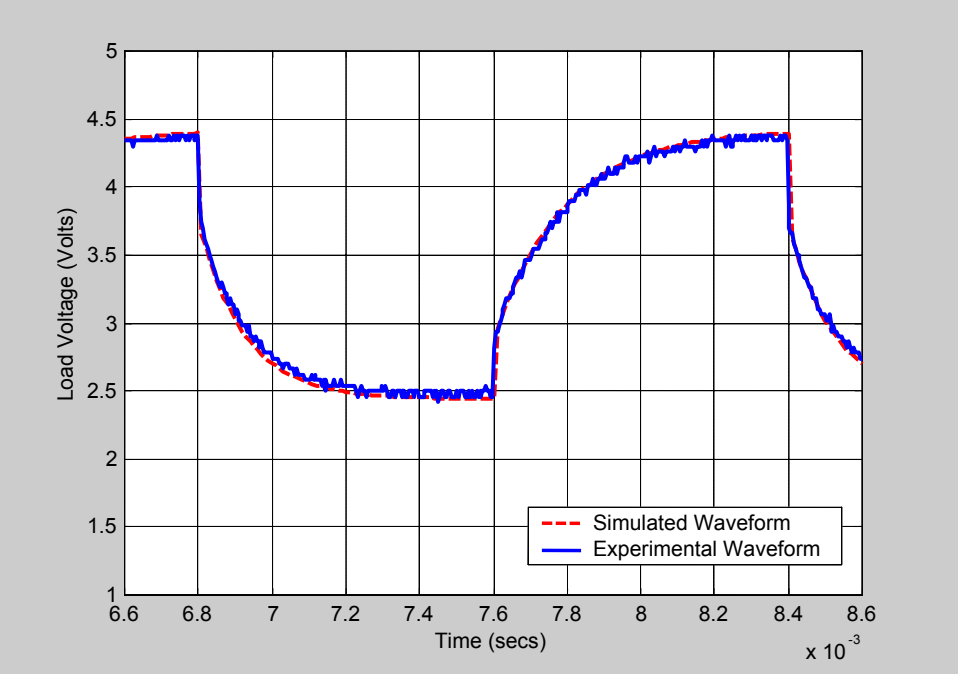

Figure 65: Comparison of experimental and simulated remote-end voltage response

A different wire arrangement in the same cable was also tested. The cable R-L-G-C parameters are provided in Appendix B and the s-domain rational fitting is provided in Appendix C. This wire arrangement of the cable leads to a DC cable resistance of approximately 320 Ω (almost the half the previous case). To differentiate between the two arrangements, this particular wire combination shall be termed as cable-2 while the previously introduced one shall be termed as Cable-1 henceforth.

The experimental setup shown in Figure 58 consisting of a constant DC input voltage of 5 V at one end of the cable and a resistive load that switches between a base load of 5.11 kΩ and a switched load now of only 160 Ω (approximately half the cable DC resistance) is used with Cable-2. When the heavy load is switched on, the remote-end voltage should reach a steady state voltage close to one-third the input voltage of 5V (i.e. the system forms a resistive divider with the cable impedance equal to twice the load impedance and the load impedance). A comparison of the experimental and simulated remote-end voltage responses is shown in Figure 66. In this case too, the experimental and simulated responses agree well with each other.

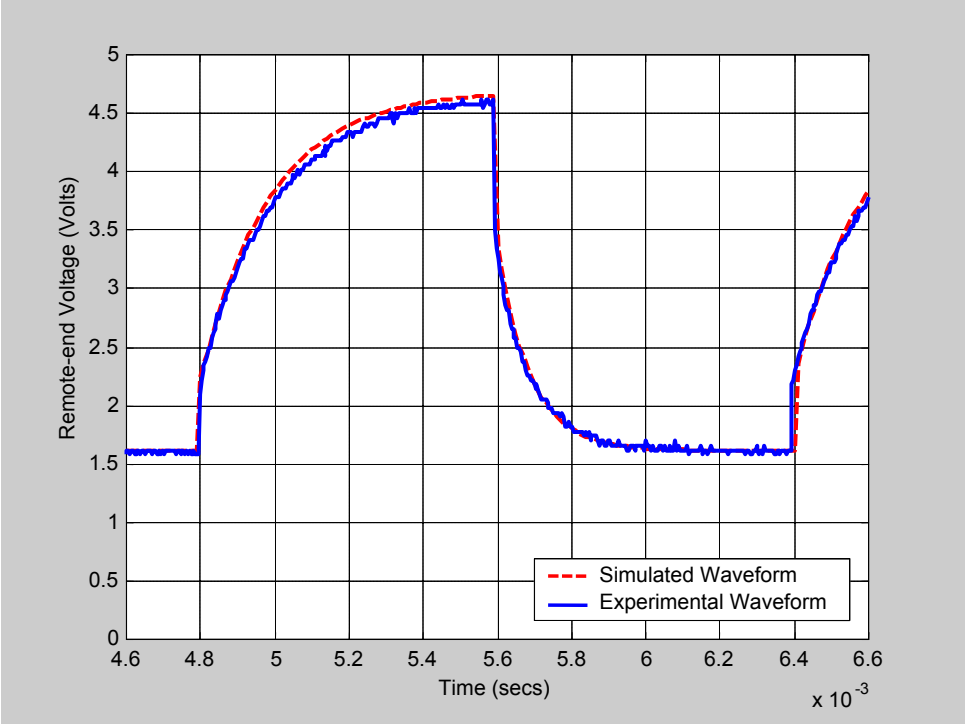

Figure 66: Remote-end voltage response with 5.11 kΩ base load and 160 Ω switched on/off

5.3.4. Simulation Approach – SPICE

For ease of simulation with complicated non-linear loads, a circuit-based approach is more useful than a state space based modeling approach. The use of Laplace domain macro-models in SPICE greatly reduces the modeling effort needed for simulating the system. As was explained in the previous section, Y_{11} and Y_{12} can be approximated by pole-zero s-domain expressions. Let us review now the key modeling equation that forms the basis for the SPICE model:

$$\begin{bmatrix} \mathbf{I}_L(s) \\ \mathbf{I}_R(s) \end{bmatrix} = \begin{bmatrix} Y_{11}(s) & Y_{12}(s) \\ -Y_{12}(s) & -Y_{11}(s) \end{bmatrix} \begin{bmatrix} \mathbf{V}_L(s) \\ \mathbf{V}_R(s) \end{bmatrix} \tag{45}$$

It can be seen that the current at one end of a cable is dependent on the same end voltage through Y_{11} and cross-coupled with the other end voltage through Y_{12}. Also, as was seen in the earlier sub-section, Y_{11} is represented by 1-pole/1-zero transfer function; hence, it can easily be represented by passive resistors and capacitors as is shown in

Figure 67 by R_1- C_1- R_2 and R_3- C_2- R_4 elements. The Y_{12}- transfer function is implemented using the Laplace function of SPICE by A_1, A_2, A_3, and A_4 as can be seen in Figure 67. Y_{11} can also be represented using the Laplace function for uniformity but has the disadvantage of increasing the simulation complexity due to the time-convolution nature of the solution. Hence, Y_{11} is implemented using passive elements and this should be possible in almost all lines as Y_{11} represents the reciprocal of the short-circuit impedance and does not have any delay elements in it.

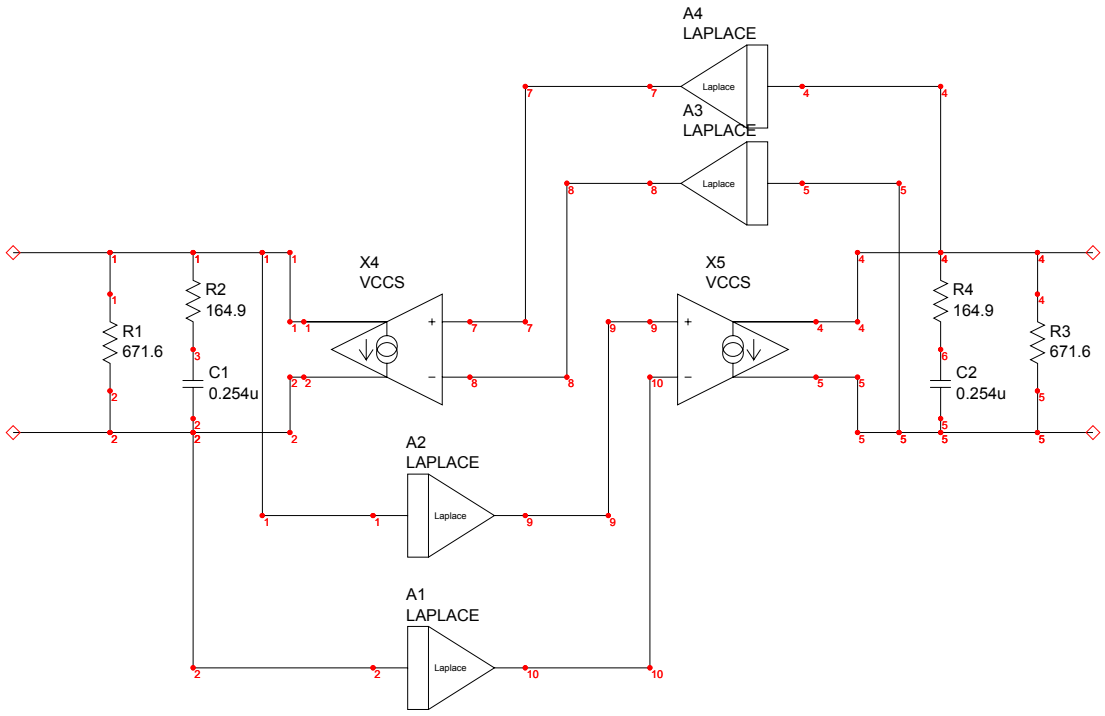

Figure 67: SPICE equivalent cable model for Cable-1

Simulation and experimental comparisons were performed as for the earlier models using the same experimental setup for both Cable-1 and Cable-2. It can be seen from Figure 68 and Figure 69 that the SPICE model accuracy is comparable to the MATLAB simulation response and approximates the experimental waveform well.

The SPICE implementation has the advantage of being user-friendly in terms of adding circuit elements with the cable model (for example complex loads or local-end circuitry) due to the presence of already existing models in SPICE. The SPICE

implementation is based on inverse LAPLACE transforms that necessitate convolutions in time to obtain the response resulting in longer computational time. The MATLAB implementation is based on using the differential equation solver to produce the time domain response from the state space representation and the main advantage of this method is the savings in computational time.

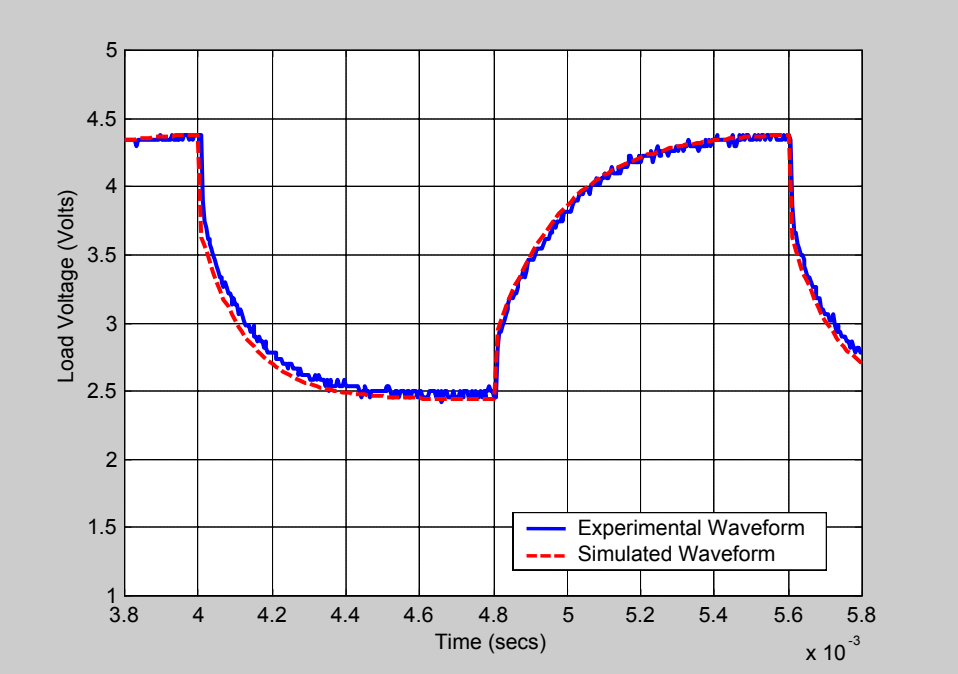

Figure 68: Comparison of SPICE simulation and experimental remote-end voltage response with 5.11 kΩ base load and 640 Ω switched on/off for Cable-1

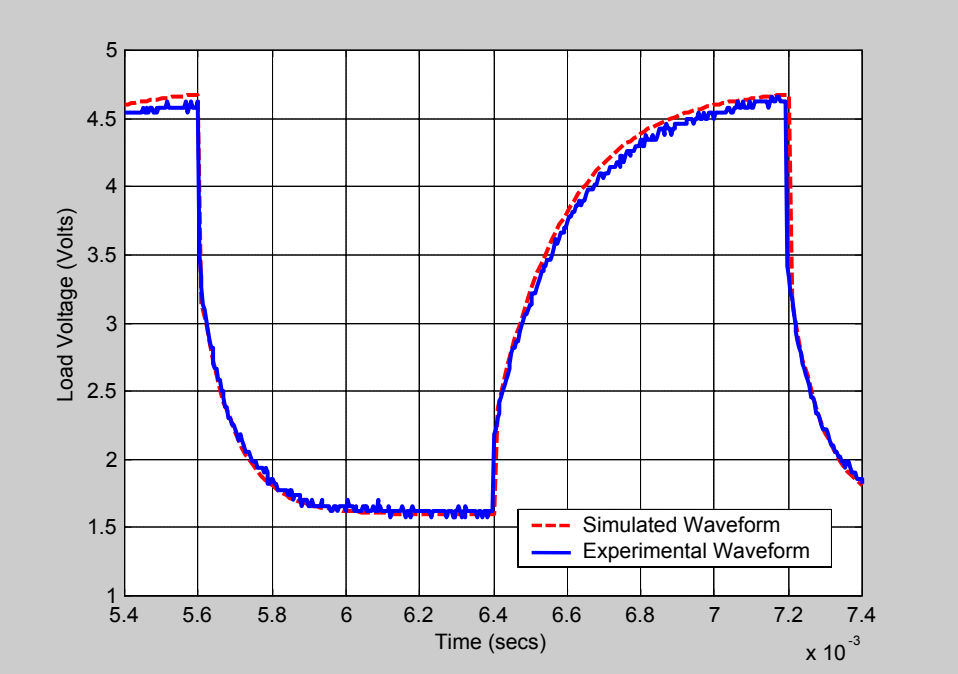

Figure 69: Comparison of SPICE simulation and experimental remote-end voltage response with 5.11 kΩ base load and 160 Ω switched on/off for Cable-2

5.4. Conclusions

In this chapter, existing transmission line models suitable for application in local-end control loops were analyzed. A transmission line model based on Padé approximations was found to give reasonable accurate results but could not be implemented due to model complexity and issues about high frequency transients. A new modeling method based on two-port Y-parameters was developed and implemented both in a state space solver (MATLAB) and a circuit based solver (SPICE). The new model was validated experimentally for two different cable arrangements. The model developed in this chapter forms the basis for controlling the voltage at the remote-end which is explored in the next chapter.

CHAPTER 6

MODEL INVERSION CONTROL FOR REMOTE-END VOLTAGE REGULATION

As mentioned in Chapter 2, the remote-end voltage needs to be regulated to boost the efficiency of the system and reduce the device stresses in the power converters. In this chapter, feed-forward approaches based on model inversion are developed to regulate the remote-end voltage. The feed-forward method requires accurate knowledge of the cable characteristics since the local-end voltage is pre-compensated for the voltage drop in the cable to maintain the remote-end voltage constant. The transmission line models developed in the previous chapter are used to obtain the inverse characteristics of the system and thus compensate for changing load conditions. An algorithm for adaptation of cable model to temperature variations is also developed in this chapter.

6.1. Model inversion perspective

The remote-end voltage, v_R changes whenever there is a load change at the remote-end. The goal is to design a controller that modifies the local-end voltage to maintain a constant level of v_R. The variables available for feedback are the local-end current (i_L) and possibly the remote-end voltage (v_R), although there is considerable delay in measurements of v_R. A block diagram representation of the open loop model inversion approach is shown in Figure 70. Note that the reference to the term open loop does not imply an open loop system but implies that there is no model update. In fact, it will be shown later in this chapter that there are two contributing feedback loops in the system controller.

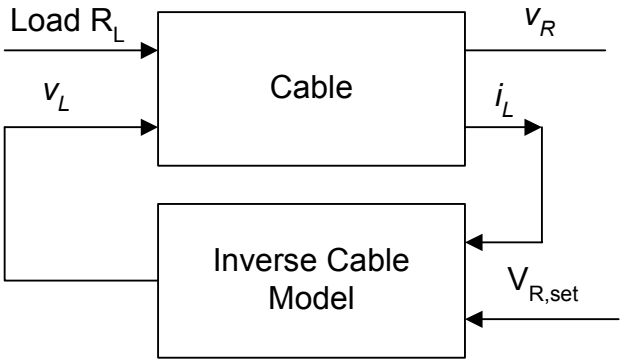

Figure 70: Open loop model inversion approach

The cable and the load at the remote-end can be combined to form a hybrid system P which switches due to changing loads. The output variables V_R and I_L in the Laplace domain can be represented in terms of the local-end voltage (V_L) as:

$$\begin{bmatrix} V_R \\ I_L \end{bmatrix} = \begin{bmatrix} P_1 \\ P_2 \end{bmatrix} V_L \tag{46}$$

where $P=[P_1 \;\; P_2]^T$.

For simplicity, the explicit dependence of the plant matrices P_1 and P_2 on the load parameters is suppressed in the following treatment. It is desirable to modify v_L to keep v_R regulated to a constant value despite the changes in load. A simple block diagram of the desired model inversion feedback is shown in Figure 71 where $G = [G_1 \;\; G_2]$ represents an approximate inverse model of the system and $V_{R,ref}$ is the reference voltage for the remote-end voltage V_R

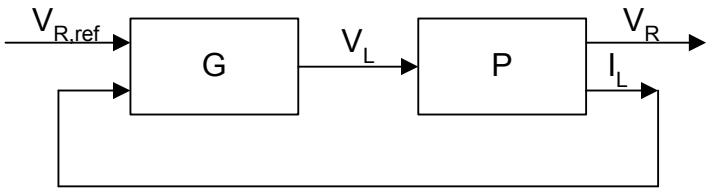

Figure 71: Open loop model inversion approach

The closed loop transfer function for the model inversion system is found to be

$$V_R = \frac{P_1 G_1}{1 - G_2 P_2} V_{R,ref} . \tag{47}$$

With suitable choice of the matrices G_1 and G_2, the closed loop system can be stabilized and the closed loop frequency response maintained close to unity over a finite frequency range. In the case of switching load conditions, the plant P is hybrid making the inverse G hybrid as well. If the exact switching times are not known at the local-end, then a straight-forward model inversion as shown in Figure 71 is not easily achievable.

In the following sections, an open loop model inversion controller based on the transmission line model explained in Chapter 5 and an appropriate choice of the matrices G_1 and G_2 is proposed and verified through simulations and experimentally

6.2. Stable inversion of cable model

As mentioned previously in Chapter 5, the cable model in the frequency domain is given by:

$$\begin{bmatrix} \mathbf{I}_L(s) \\ \mathbf{I}_R(s) \end{bmatrix} = \begin{bmatrix} Y_{11}(s) & Y_{12}(s) \\ -Y_{12}(s) & -Y_{11}(s) \end{bmatrix} \begin{bmatrix} \mathbf{V}_L(s) \\ \mathbf{V}_R(s) \end{bmatrix} \tag{48}$$

In the case of the control of the remote-end voltage, we can have measurements of the local-end voltage and current and a predetermined model for the cable. Rewriting the above equation from a control perspective:

$$\mathbf{V}_R(s) = -\frac{Y_{11}(s)}{Y_{12}(s)} \left(\mathbf{V}_L(s) - \mathbf{I}_L(s) \frac{1}{Y_{11}(s)} \right) \tag{49}$$

The term inside the brackets in the above expression corresponds to the remote-end voltage in a cable with an impedance equal to the short circuit impedance of the cable and no delay effects. The transmission line effect of the cable is represented by the pre-multiplying ($-Y_{11}/Y_{12}$) term. It should be noted that when we approximated $Y_{12}(s)$ during the modeling part, it was necessary to include right half plane zeros to correct the phase at high frequencies. Since in the remote-end voltage estimation we deal with the inverse of Y_{12}, the same model would result in an unstable system. From a practical standpoint ($-Y_{11}/Y_{12}$) represents the attenuation and propagation delay. The phase delay cannot be compensated unless we can anticipate the remote-end load changes, which is practically

infeasible. On the other hand we can try to compensate for the attenuation by fitting the magnitude response of ($-Y_{11}/Y_{12}$) as best as we can (i.e. we drop the right half plane zeroes and corresponding poles from the approximation for Y_{12}). So for example for Cable-2, the approximation for ($-Y_{11}/Y_{12}$) to be used in the control loop can be obtained as (the asterixes indicate that these are approximate models used in the control loop):

$$\left(\frac{-Y_{11}}{Y_{12}}\right)^{*} = \left(\frac{1+\frac{s}{5026.5}}{1+\frac{s}{25761.1}}\right)\left(\frac{1+\frac{s}{31415.9}}{1+\frac{s}{100531}}\right) \tag{50}$$

A frequency domain comparison of the fitted and experimental data for the ($-Y_{11}/Y_{12}$) term is shown in Figure 72. It is also evident from Figure 72 that while the magnitude shows a simple increase with frequency, the phase keeps increasing with frequency (implying the inverse time delay dynamics). So, the approximation in ($-Y_{11}/Y_{12}$) takes into account the attenuation but not the non-causal inverse time delay characteristic which cannot be compensated for.

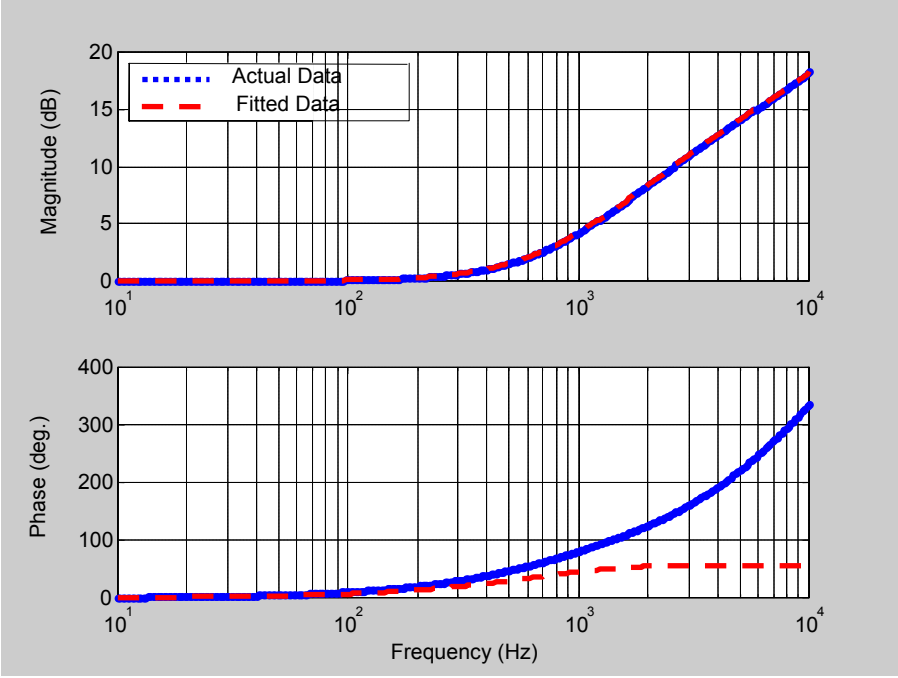

Figure 72: Frequency domain plot of ($-Y_{11}(s)/ Y_{12}(s)$) for Cable-2

6.3. Remote-end voltage controller

As explained in the previous section, the remote-end voltage can be estimated by measuring the local-end voltage and current. The remote-end voltage is then compared with the nominal reference voltage that needs to be maintained at the remote end to generate the error voltage. The error voltage is passed through a proportional integrator (PI) to generate the corresponding reference local-end voltage $V_{L,ref}$. This reference local-end voltage serves as the control voltage to the power converter that outputs the local-end voltage. Figure 73 shows the block diagram representation of the new control strategy.

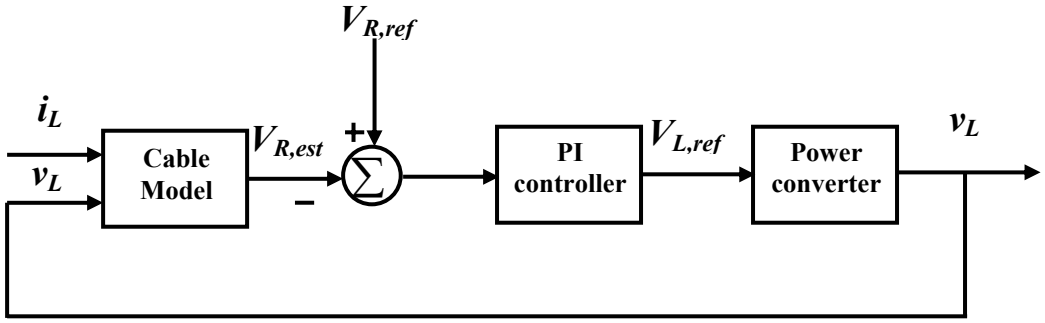

Figure 73: Control strategy

6.4. Remote-end voltage controller stability

In this section we analyze the control stability through linear system analysis. Recall that the currents at the local and remote-ends can be represented in terms of the voltages at both ends of the cable as:

$$\begin{bmatrix} \mathbf{I}_L(s) \\ -\mathbf{I}_R(s) \end{bmatrix} = \begin{bmatrix} Y_{11}(s) & Y_{12}(s) \\ Y_{12}(s) & Y_{11}(s) \end{bmatrix} \begin{bmatrix} \mathbf{V}_L(s) \\ \mathbf{V}_R(s) \end{bmatrix} \tag{51}$$

The load impedance (or admittance $Y_L(s)$) determines the relationship between the voltage and current at the remote-end of the cable as given below:

$$\mathbf{I}_2 = Y_L \mathbf{V}_2 \Rightarrow \mathbf{V}_2 = \frac{-Y_{12}}{Y_{11} + Y_L} \mathbf{V}_1 \tag{52}$$

With this simplification for the load-side relationships, the local-end equations can be simplified to:

$$\mathbf{I}_1 = \left(Y_{11} - \frac{Y_{12}^2}{Y_{11} + Y_L} \right) \mathbf{V}_1 \tag{53}$$

The new remote-end voltage control strategy is based on obtaining an estimate of the remote-end voltage by measuring the local-end voltage and current and using a base model of the transmission line. (The asterixes are meant to indicate that the values are model estimates and not the true values)

$$\mathbf{V}_R^* = \frac{-Y_{11}^*}{Y_{12}^*} \left(\mathbf{V}_L - \frac{\mathbf{I}_R}{Y_{11}^*} \right) \tag{54}$$

The estimate of the remote-end voltage ($\mathbf{V}_R^*$) obtained by the inversion process is compared with the set reference value ($\mathbf{V}_{R,ref}$) and passed through an integrator ($\mathbf{H_I(s)}$) whose output determines the input local-end voltage as:

$$\mathbf{V}_L = \mathbf{V}_{R,ref} + \left(\mathbf{V}_{R,ref} - \mathbf{V}_R^* \right) \mathbf{H}_I \;\; where \;\; \mathbf{H}_I = K_p + \frac{K_i}{s} \tag{55}$$

With the above plant and control equations, the system can be represented by a simple block diagram as shown in Figure 74. It can be easily seen that the closed loop control system leads to two dependent control loops involving the voltage and current measurements and the relative stability of the system cannot be easily analyzed using classical frequency domain approaches.

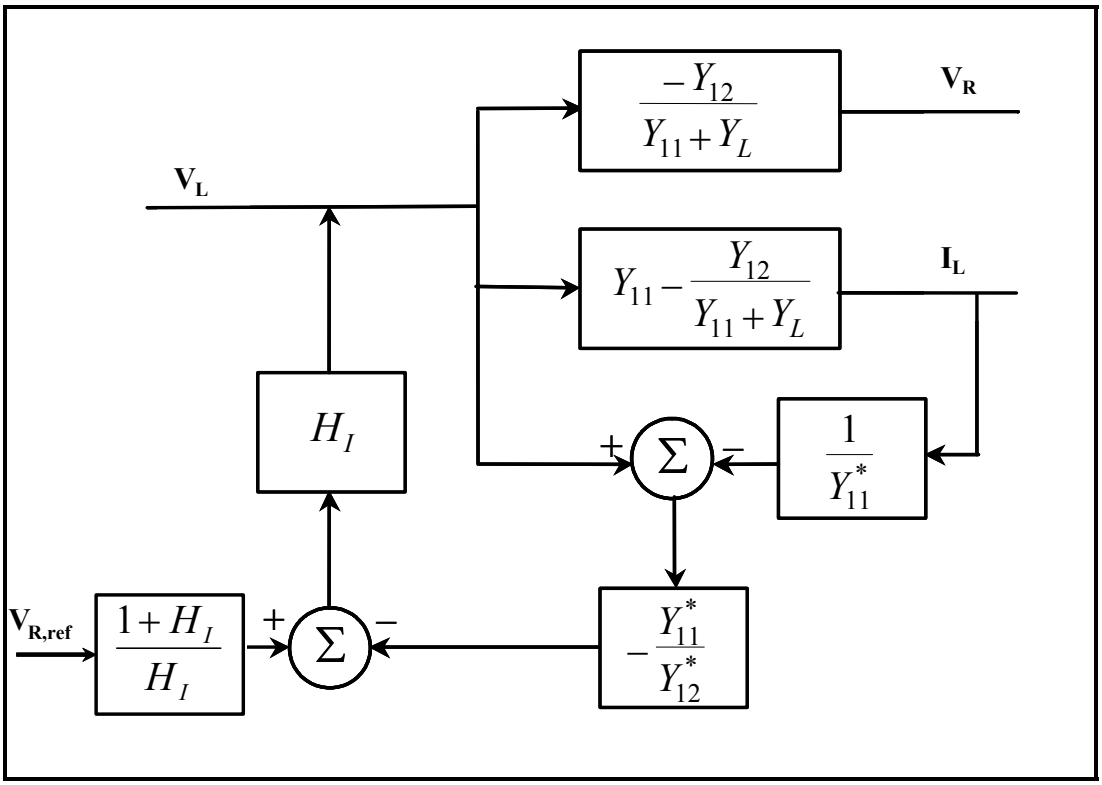

Figure 74: Block diagram representation of closed loop system

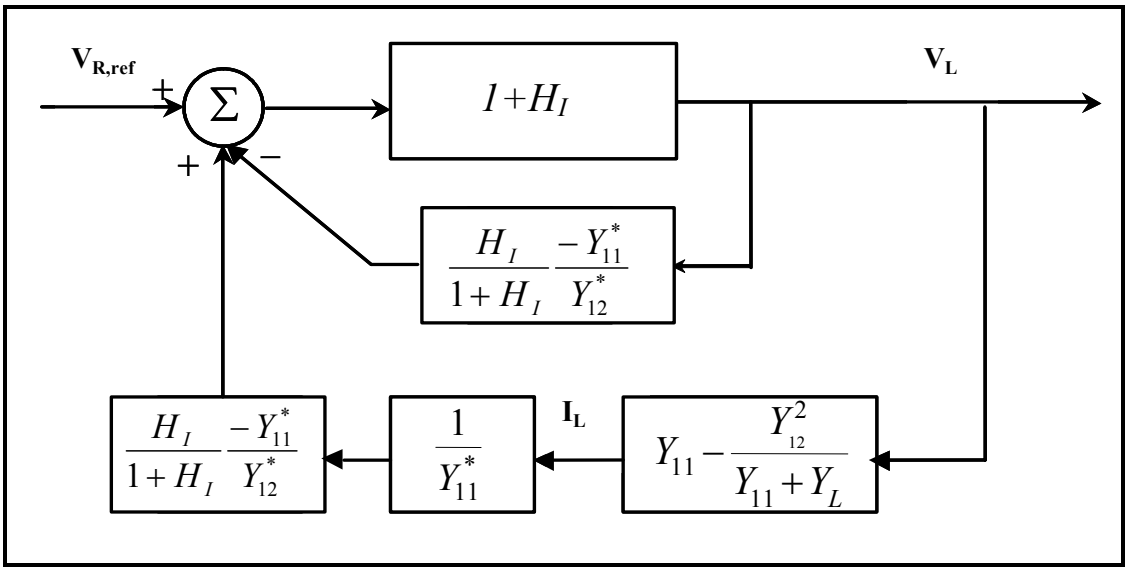

Figure 75: Simplified block diagram representation of closed loop system

For analysis purposes, Figure 74 can be redrawn as shown in Figure 75. With the above representation, it is clear that we have two feedback loops acting in parallel on the reference voltage to produce the input voltage. The input-output relationships of the system can be given as:

$$\begin{aligned} \mathbf{V}_L &= \frac{1+\mathbf{H}_I}{1+\mathbf{T}_c+\mathbf{T}_v}\mathbf{V}_{R,ref} \quad \Rightarrow \quad \mathbf{V}_R = \frac{-Y_{12}}{Y_{11}+Y_L}\frac{1+\mathbf{H}_I}{1+\mathbf{T}_c+\mathbf{T}_v}\mathbf{V}_{R,ref} \\ \mathbf{T}_v &= -\mathbf{H}_I\frac{Y_{11}^*}{Y_{12}^*};\ \mathbf{T}_c = \mathbf{H}_I\left(\frac{1}{Y_{12}^*}\right)\left(Y_{11}-\frac{Y_{12}^2}{Y_{11}+Y_L}\right) \end{aligned} \tag{56}$$

It is clear with this representation that the closed loop system has a single loop with the loop gain given by the sum of the individual current and voltage loop gains as specified above. The stability of the system can be assessed now by usage of Bode or Nyquist plots of the loop gain.

6.5. Simulation approach and results

6.5.1. MATLAB implementation of control strategy

Recall from the previous chapter that the cable-load system for a constant input voltage can be expressed in state-space form as:

$$\begin{aligned} \dot{\mathbf{x}} &= \begin{bmatrix} \dot{x}_C \\ \dot{x}_L \end{bmatrix} = \begin{bmatrix} A_C & 0 \\ 0 & A_L \end{bmatrix}\begin{bmatrix} x_C \\ x_L \end{bmatrix} + \begin{bmatrix} B_{C1} & B_{C2} \\ 0 & B_L \end{bmatrix}\begin{bmatrix} v_L \\ v_R \end{bmatrix} \\ \text{Cable-Load Model: } \mathbf{y} &= \begin{bmatrix} i_L \\ i_R \end{bmatrix} = \begin{bmatrix} C_{C11}x_C + D_{C11}v_L + D_{C12}v_R \\ C_{C21}x_C + D_{C21}v_L + D_{C22}v_R \end{bmatrix} \\ v_R &= \left(D_L - D_{C22}\right)^{-1}\left(C_{C21}x_C - C_L x_L + D_{C21}v_L\right) \end{aligned} \tag{57}$$

To simulate the closed loop system, the remote-end voltage controller model needs to be appended to the cable-load interconnected model. The local-end current i_L and local-end voltage v_L form the input of the compensator model while the output of the compensator is the compensated local-end voltage v_L or, more generically the control input to the local-end power supply. With the assumption that the local-end power supply bandwidth is much higher than the remote-end voltage control circuit, the control voltage only introduces a gain in the feedback loop and can be assumed to be unity without loss of

generality. The feed-forward compensator model can be represented in state space form as:

$$\text{Compensator Model: } \begin{aligned} \dot{\mathbf{x}}_f &= A_f x_f + B_{f1} v_L + B_{f2} i_L + B_{f1} V_{R,ref} \\ \mathbf{y}_f &= v_L = C_f x_f + D_f V_{R,ref} \end{aligned} \tag{58}$$

The closed loop system model can now be obtained by combining the compensator model with the open loop cable-load interconnected model.

$$\dot{\mathbf{x}} = \begin{bmatrix} \dot{x}_C \\ \dot{x}_L \\ \dot{x}_f \end{bmatrix} = \begin{bmatrix} A_C & 0 & 0 \\ 0 & A_L & 0 \\ B_f C_{C11} & 0 & A_f \end{bmatrix} \begin{bmatrix} x_C \\ x_L \\ x_f \end{bmatrix} + \begin{bmatrix} B_{C1} & B_{C2} & 0 \\ 0 & B_L & 0 \\ B_{f1} + B_{f2} D_{C11} & B_{f2} D_{C12} & B_{f3} \end{bmatrix} \begin{bmatrix} v_L \\ v_R \\ V_{R,ref} \end{bmatrix} \tag{59}$$

$$\begin{bmatrix} v_L \\ v_R \end{bmatrix} = \begin{bmatrix} C_f x_f + D_f V_{R,ref} \\ \left(D_L - D_{C22}\right)^{-1} \left(C_{C21} x_C - C_L x_L + D_{C21} \left(C_f x_f + D_f V_{R,ref}\right)\right) \end{bmatrix}$$

The resulting system has a single input $V_{R,ref}$ that sets the remote-end nominal voltage. Note that for simplicity of expressions, the local-end voltage v_L, and the remote-end voltage v_R have not been expanded in the state differential equations.

6.5.2. Simulation results

The compensator model explained in the previous section was implemented in MATLAB in state space format and simulated. Cable-2 was used with the load resistance at the remote-end switched between 5.11 kΩ (almost open circuited) to 340 Ω (approximately matched to the cable resistance corresponding to the maximum power point). Note that in the simulation, the compensator uses a reduced order cable model but a full order model is used to simulate the cable. Figure 76 shows the simulation setup with the remote-end voltage controller.

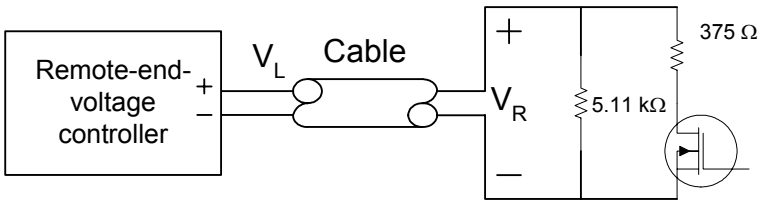

Figure 76: Experimental setup for verifying cable model

A series R-C circuit in parallel with the load at the remote-end was incorporated to dampen the system oscillations when the cable is lightly loaded. The Nyquist plot of the open loop gain of the system without the damping circuit comes close to encircling the –1+j0 point indicating very low stability margins. With the remote-end damping R-C circuit of a 300 Ω resistance in series with a 8.3 μF capacitor the stability margins of the system operated using Cable-2 improve and the system is less under-damped compared to without the damping circuit as can be seen from Figure 77. The loops in the Nyquist plot around the origin are due to the higher order dynamics of the cable. An integrator gain of 4545 (with the proportional gain maintained at 1.0) was used and results in a critical/slightly over-damped system. The optimal integrator gain corresponds to when the integrator zero is placed at around the same frequency of the pole in the short-circuit impedance (i.e. a type of pole-zero canceling effect). The theory behind the optimality of this choice of R-C damping circuit and integrator gain will be explained later in this chapter. The simulation results are shown in Figure 78.

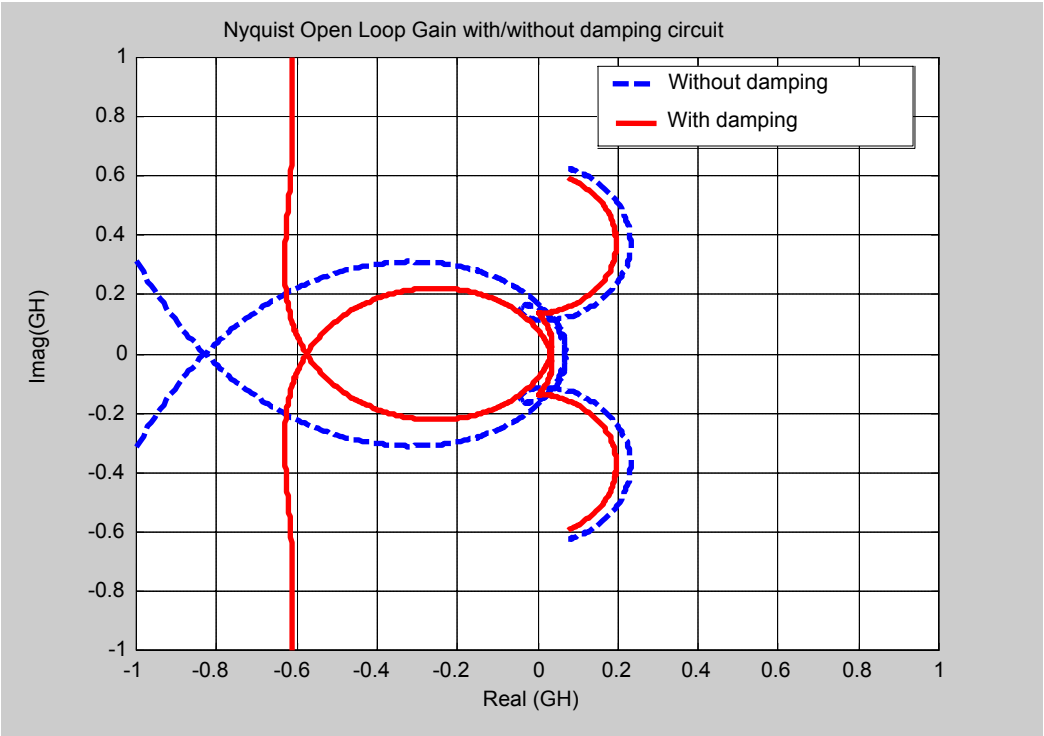

Figure 77: Nyquist plot of open loop gain with/without damping circuit

The estimated remote-end voltage (computed in the controller) approximates the actual remote-end voltage (the output of the cable model) with the inherent transmission line delay in the system. When the light load is only connected, the remote-end voltage is approximately 30 V while the local-end voltage is around 34 V. When the heavy load is connected, the remote-end voltage is regulated at 30 V after a short inevitable transient while the local-end voltage rises to 58 V to compensate for the increased voltage drop across the cable. The transient is due to the time delay inherent in the cable. Approximated by a non-minimum phase model, which imposes bandwidth limitations on the controller, it is clear why the transient is inevitable. Referring back to earlier results with the uncontrolled system in Chapter 5, the system stabilized to the new operating point in approximately 0.8 ms. Moreover, the remote-end voltage was not maintained at the reference voltage but rather changes with the load as seen in Figure 66. With the model inversion controller, we can see from the simulation results that the remote-end voltage is stabilized in approximately 2 ms in both heavy to light load transition and light

to heavy load transition. So in approximately two and a half-times the time constant of the system, the remote-end voltage can be stabilized at its nominal reference voltage.

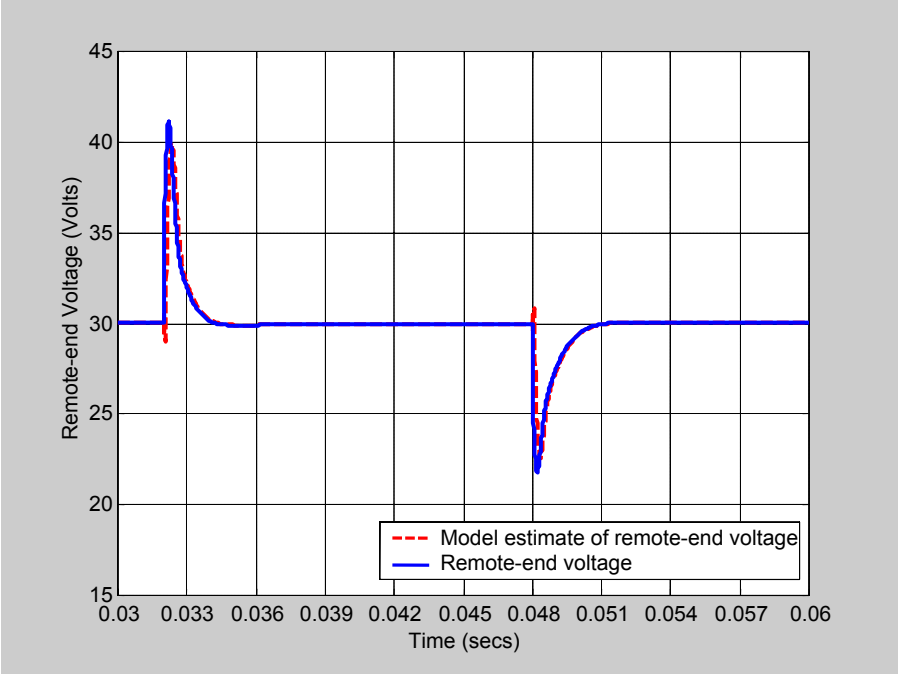

Figure 78: Simulated actual and estimated remote-end voltage responses

6.6. Experimental setup and comparison with simulation results

From the simulated results in the previous section, we can see that a fast control system is possible and were able to observe the time domain response of the system with the new control strategy. The controller at the local-end was implemented and was tested with both the cables to verify the control strategy and the simulation models. The s-domain control loop cable models were practically implemented using op-amps and passive resistors and capacitors. For the experimental design of the control loop, we need to be able to implement $1/Y_{11}$ and $(-Y_{11}/Y_{12})$. Recall for Cable-2 these transfer functions were given by:

$$\frac{1}{Y_{11}^*} = 319.8\left(\frac{1+\frac{s}{25761.1}}{1+\frac{s}{5026.5}}\right) ohm$$
$$\left(\frac{-Y_{11}}{Y_{12}}\right)^* = \left(\frac{1+\frac{s}{5026.5}}{1+\frac{s}{25761.1}}\right)\left(\frac{1+\frac{s}{31415.9}}{1+\frac{s}{100531}}\right) \quad (60)$$

The asterixes indicate that the transfer functions are model approximations and not exact. With the above pole-zero representation, it is easy to implement these transfer functions using operational amplifiers, resistors and capacitors. Typical implementations of the above transfer functions are shown in Figure 79 and Figure 80.

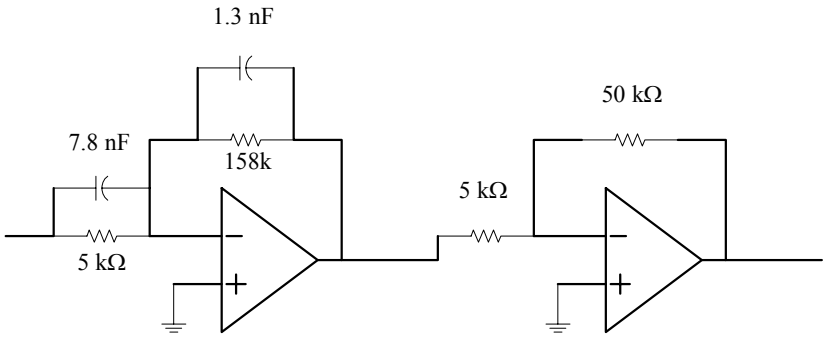

Figure 79: Example implementation of $1/Y_{11}$

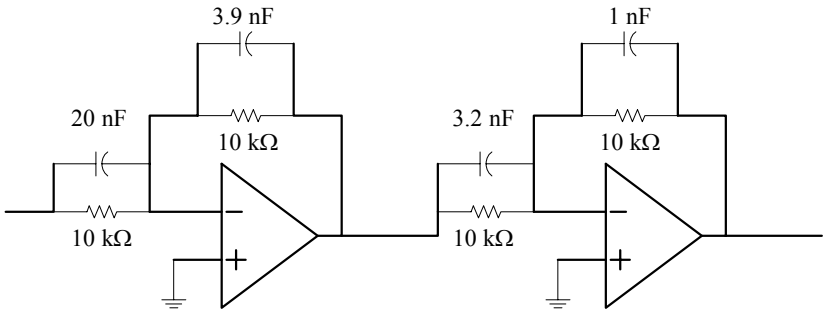

Figure 80: Example implementation of $(-Y_{11}/Y_{12})$

The integrator gain was maintained at 4545 and the experimental setup was tested with the remote-end damping pole components at R=300 Ω and C=8.3 μF. A HP6827A

fixed gain amplifier was used to generate the local end-voltage corresponding to the reference voltage set by the model inversion controller. A block diagram view of the experimental setup is shown in Figure 81.

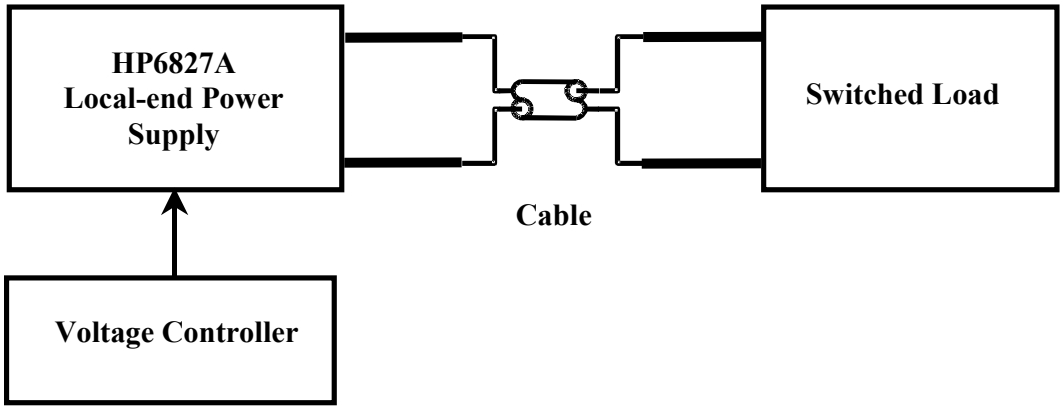

Figure 81: Block diagram of experimental setup with model inversion controller

Figure 82 shows the response of the system with the load switched in and out at a frequency of 250 Hz. The experimental responses are similar to those presented for the simulation results in the previous section. The theoretical responses obtained through MATLAB simulations using the cable model and the experimental responses are compared in Figure 83 and Figure 84. The close matching of the experimental and simulated responses validates the modeling approach and the feasibility of the control strategy.

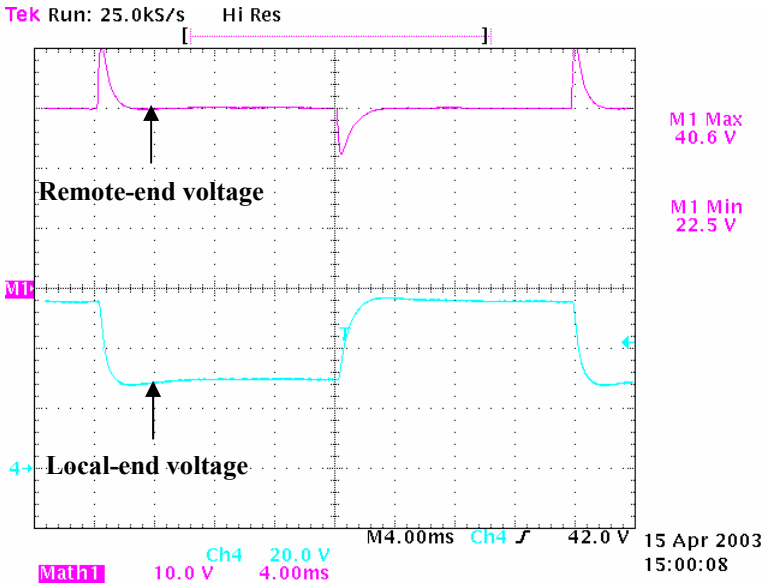

Figure 82: System response for Cable-2

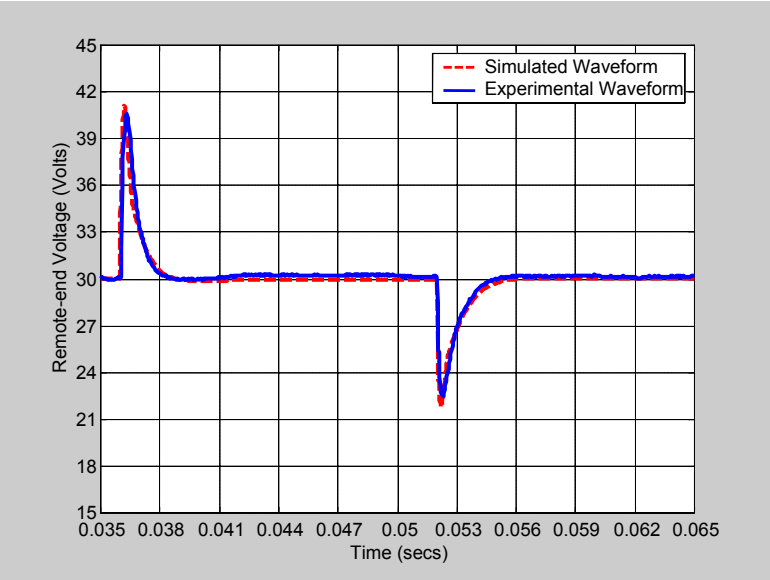

Figure 83: Comparison of remote-end voltage response for Cable-2

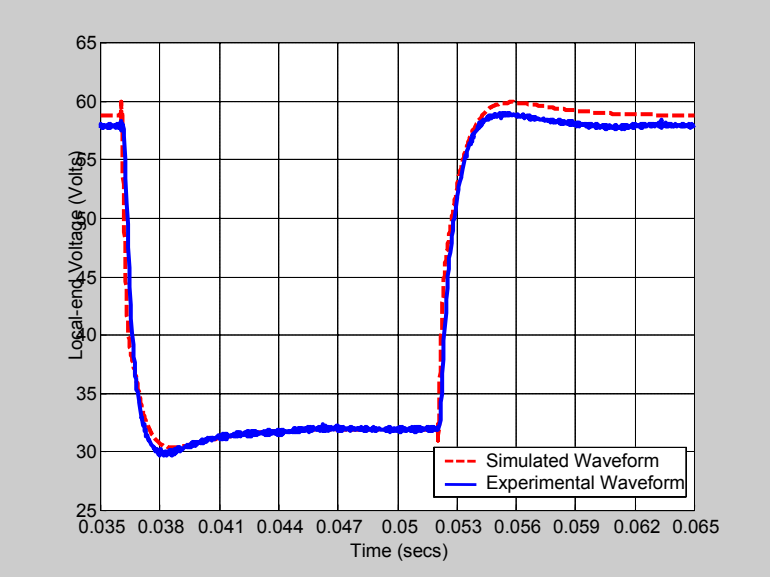

Figure 84: Comparison of local-end voltage response

The experimental tests were also done for Cable-1 with the load in this case switched between 5.11 kΩ and 670 Ω. Recall that the DC resistance of Cable-1 is 670 Ω. Figure 85 shows the response of the system with the load switched in and out at a frequency of 500 Hz. It can be noted that in this case also, the voltage controller maintains the remote-end voltage constant at 30 V except during a 2 ms transient period.

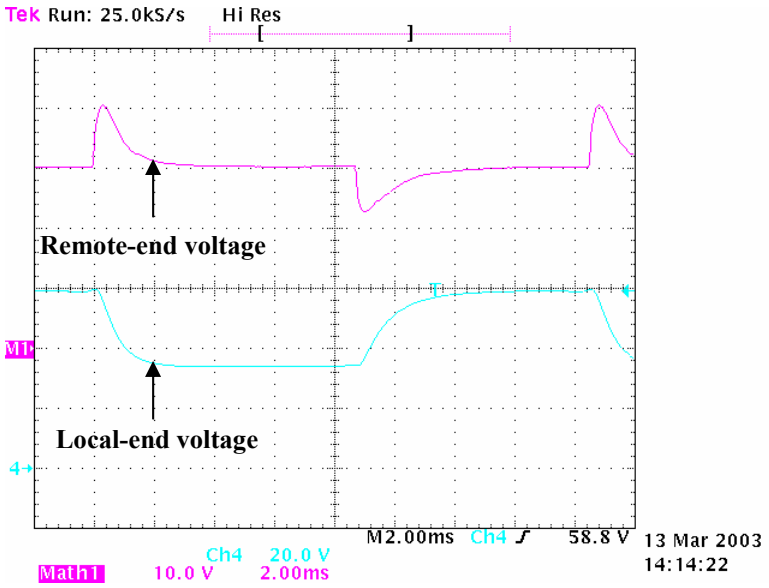

Figure 85: System response for Cable-1

6.7. Control System Issues

6.7.1. Remote-end Damping Circuit

The damping circuit of a series resistor and capacitor Rp-Cp connected in parallel with the load at the remote-end as shown in Figure 86 was used to dampen oscillatory behavior during the heavy to light load transition (i.e. the line is almost open-circuited suddenly). A brief study of the need for this damping circuit was seen in the earlier section. In this section, the optimal choice of Rp-Cp in the damping circuit is explored.

The Rp-Cp damping circuit limits the impedance seen at the remote-end at high frequencies by the cable impedance. The closed loop gain of the remote-end voltage with respect to the reference voltage (refer Chapter 6.4) determines the optimal choice of the Rp-Cp values. Ideally, a maximally flat response is desired for the closed loop gain. The closed loop gain for different damping resistors of 100 Ω, 300 Ω, and 500 Ω with the damping capacitance fixed at 8.3 μF (note that the plots pertain to the high load resistance (light load current) case) for Cable-2 is shown in Figure 87. As can be seen from Figure 87, a damping resistance of 300 Ω (i.e. approximately matched to the line)

provides an optimally flat closed loop gain response. Other damping resistances produce peaking at higher or lower frequencies leading to either under or over-damped responses with step changes in input. The optimal choice of capacitance or damping pole frequency can be obtained by examining the closed loop response for varying capacitor values shown in Figure 88 with the series resistance fixed at approximately the line resistance (300 Ω). Too low a value of capacitance leads to peaking in the closed loop response (see response for Cp=1 μF) while too high a value (see response for Cp=22 μF) only provides marginal improvement over the response for the optimal capacitor value (8.3 μF).

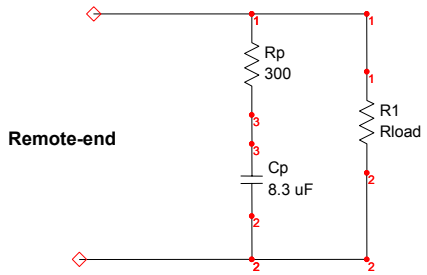

Figure 86: Remote-end damping circuit for Cable-2

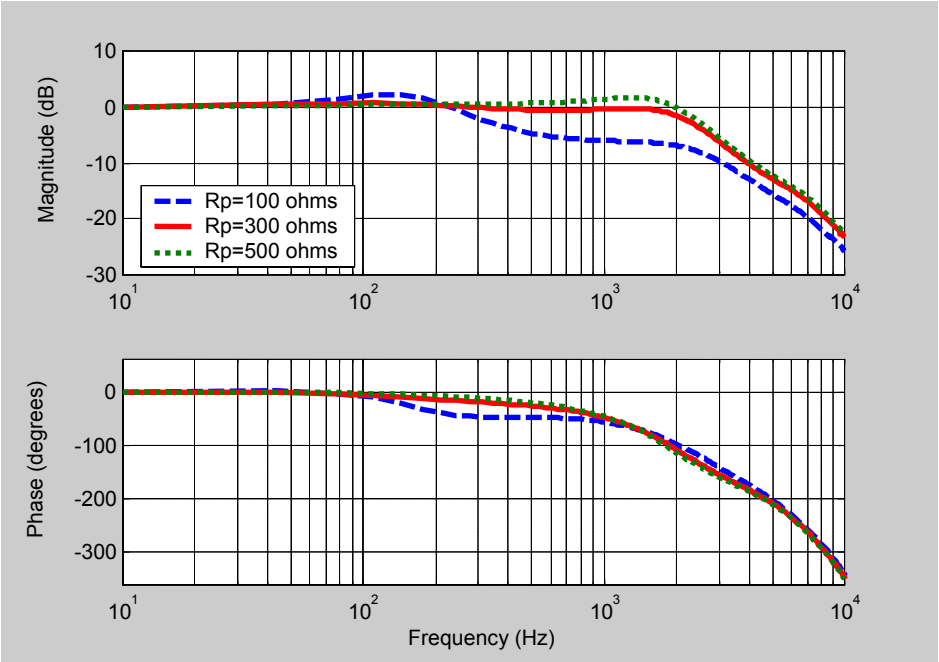

Figure 87: Closed loop gain with varying damping resistor (Cp=8.3 μF)

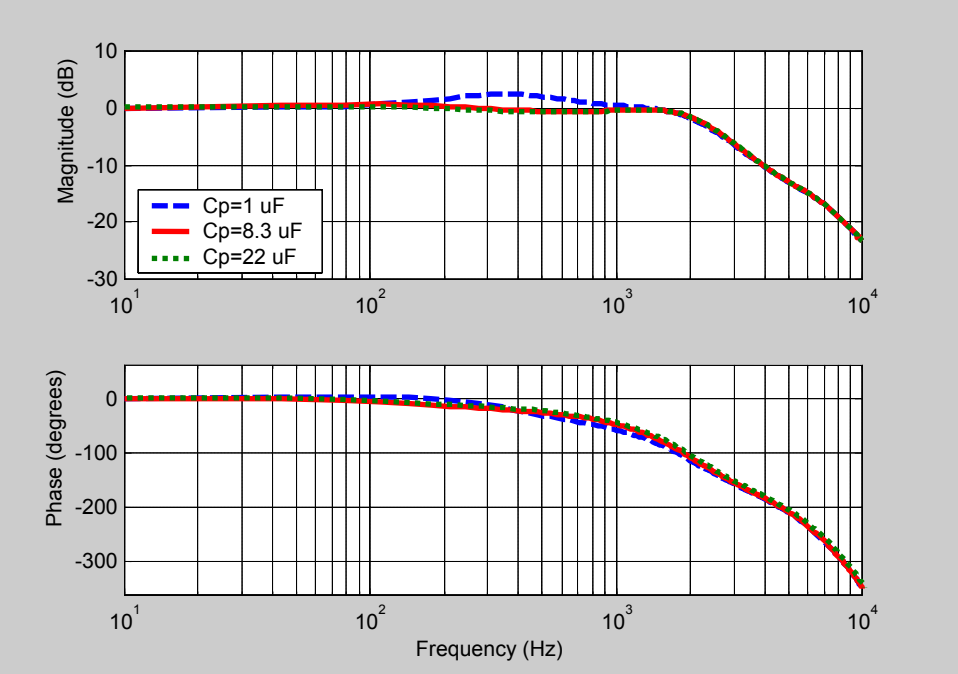

Figure 88: Closed loop gain with varying damping capacitor (Rp=300 Ω)

6.7.2. Impact of Integrator Gain

The integrator gain allows for one degree of freedom in optimizing the system. Too high an integrator gain results in an under-damped system and, in the worst case, an unstable system while too low an integrator gain results in an over-damped system. In both cases, the transient recovery time is increased and does not provide any additional benefit in terms of remote-end voltage transient reduction. For both cables studied, an integrator gain that resulted in a zero approximately in the 750-1000 Hz region was optimum. Recall that the short-circuit impedance of both the cables has a pole around approximately the same frequency. Hence the optimality of the integrator gain can be related to a pole-zero canceling effect obtained when the integrator zero is placed at around the same frequency of the pole in the short-circuit impedance.

Table 3 shows a comparison of the remote-end and local-end voltage transients with changes in integrator gain for a resistive load switched between 340 Ω and 5.11 kΩ using Cable-2. Figure 89, Figure 90, and Figure 91 show the local and remote-end voltage responses as the integrator gain is increased (i.e. over-damped to under-damped system). From the results, it is clear that the placement of the integrator gain close to the

pole frequency of the short-circuit impedance of the cable leads to optimal transient performance of the system. Also, the wide range of integrator gains over which the transient performance is satisfactory (for example in our case: K_i=3125-14706) can be used to accommodate the characteristics of different cables if they are approximately similar.

Table 3: Comparison of transient parameters with integrator gain

Integrator Gain (K_i)	*Head Voltage Peak (%)*	*Source Voltage Valley (%)*	*Transient Recovery Time (ms)*	*Oscillation Mode*
3125	33	3	4	Over-damped
4545	**33**	**3**	**2**	**Critically damped**
14706	33	17	4	Under-damped
21277	33	33	6	Under-damped
37037	-	-	-	Unstable

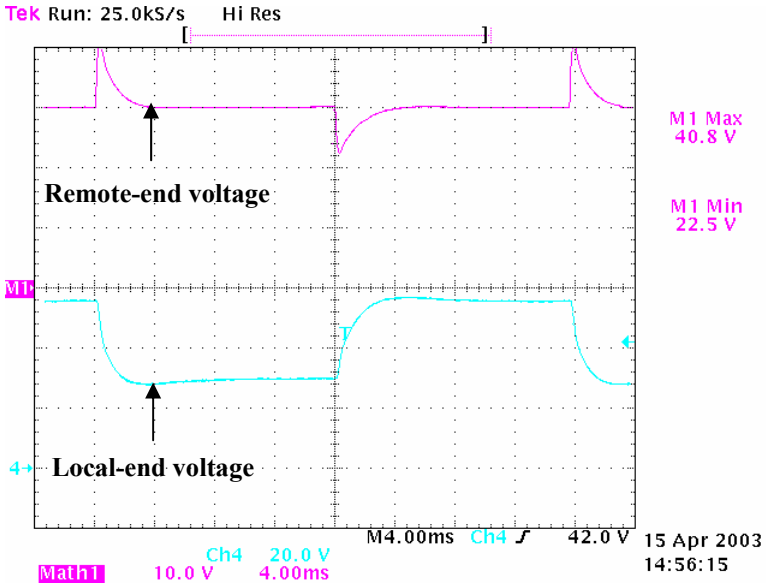

Figure 89: System response with Ki=3125

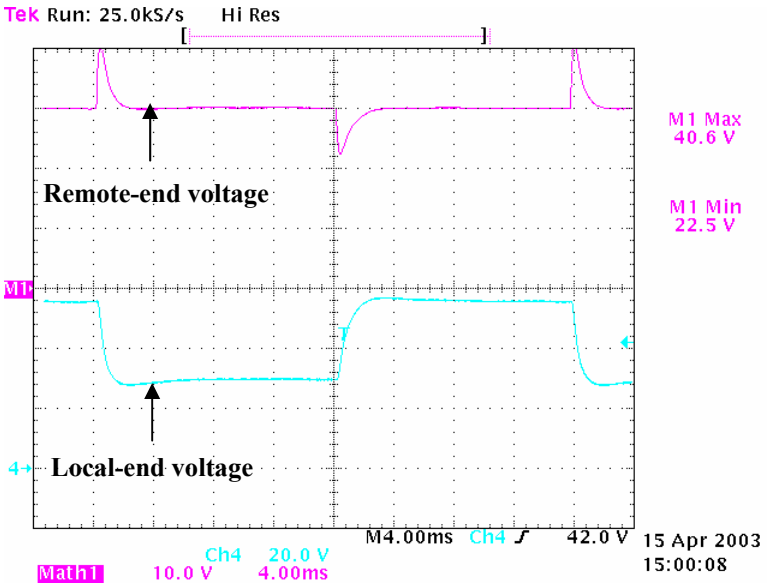

Figure 90: System response with Ki=4545

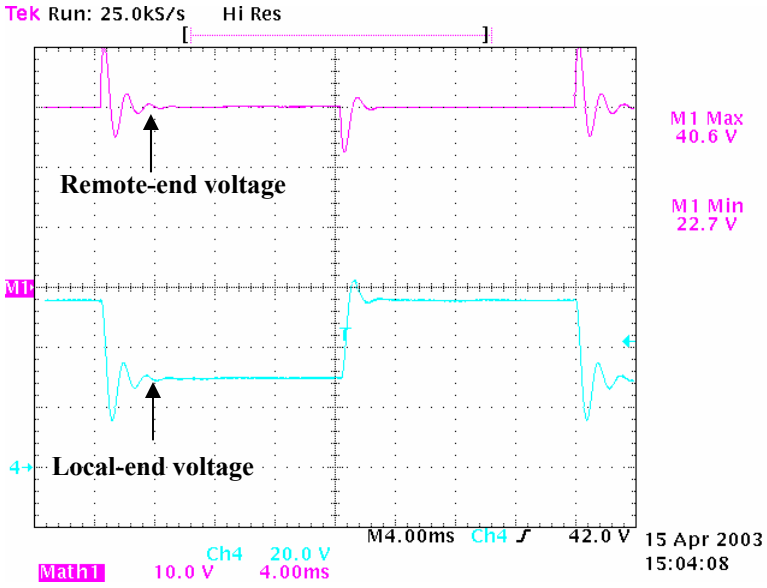

Figure 91: System response with Ki=14706

6.8. Remote-end voltage transient compensation

It was seen in earlier sections that the remote-end voltage has transient over and under-voltages during load changes that cannot be compensated by the local-end control system due to the inherent propagation delay of the transmission line and the bandwidth of the controller. Remote-end voltage transient compensation methods such as bulk capacitances at the remote-end and active clamping solutions are investigated in this section.

6.8.1. Remote-end Bulk Capacitance

A simple first choice for the reduction of transient peak would be the addition of a capacitance at the remote-end in parallel to the load. The capacitor sources or sinks current in the transient period during load changes and reduces the sensitivity of the model inversion control which is based on a measurement of the local-end voltage and current. The remote-end voltage control no longer sees the load current but the sum of the load and capacitor currents. Since the capacitor tries to maintain the remote-end voltage constant, it would have a destabilizing effect on the local-end control system. With this understanding of the effect of large capacitances at the remote-end we can expect a reduction in over and under-voltages and an increase in the settling time after load changes.

To confirm the effect of large capacitances at the remote-end, a resistive load is switched between 350 Ω and 5 kΩ using Cable-2. Figure 92 shows the system response with a large head capacitance of 47 μF connected in parallel with the resistive load. It is clear that over and under-voltages of the order of 30% (refer to Table 3 in Chapter 6.7.2) without a remote-end capacitor are reduced to 10% by the addition of large enough capacitance. But, the transient recovery time increases from 2ms (without remote-end capacitance) to approximately 40 ms (with 47 μF remote-end capacitance).

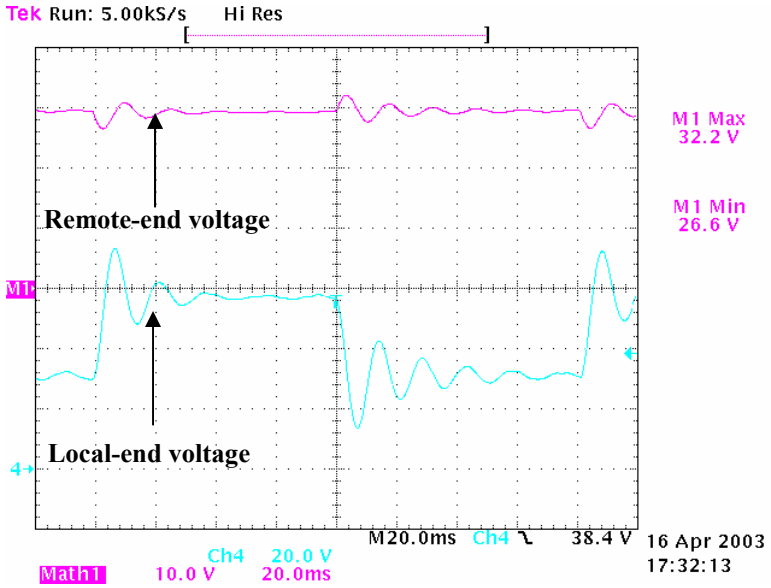

Figure 92: System response with remote-end capacitance of 47 μF

The control loop stability of the system with large capacitances was further investigated due to seemingly "random" occurrences of instability during practical testing. It was possible to stabilize/destabilize the system by varying the estimated cable resistance using a potentiometer with the experimental setup. Consider the open loop gain of the remote-end voltage control as explained earlier in Chapter 6.4:

$$\mathbf{T} = \mathbf{T}_c + \mathbf{T}_v = -\mathbf{H}_I \left(\frac{Y_{11}^*}{Y_{12}^*} - \left(\frac{1}{Y_{12}^*} \right) \left(Y_{11} - \frac{Y_{12}^2}{Y_{11} + Y_L} \right) \right) \tag{61}$$

With a large capacitance C_L in parallel with the load resistance R_L, the load impedance can be written out as:

$$Y_L = \frac{1}{R_L} + sC_L = \frac{1 + sR_L C_L}{R_L} \tag{62}$$

At low frequencies, the transfer functions can be approximated by constant values as:

$$Y_{11} \approx \frac{1}{R_{dc}}; Y_{12} \approx -\frac{1}{R_{dc}}; Y_{11}^* \approx \frac{1}{R_{dc}^*}; Y_{12} \approx -\frac{1}{R_{dc}^*}; \tag{63}$$

where R_{dc} represents the DC resistance of the cable and R_{dc}^* the estimated cable resistance used in the control loop model. With these approximations, the loop gain at low frequencies can be simplified as:

$$\mathbf{T} \approx \left(K_p + \frac{K_i}{s} \right) \left(\frac{R_{dc} - R_{dc}^*}{R_{dc}} + \frac{R_{dc}^* R_L}{R_{dc}^2} \right) \frac{\left(1 + sC_L R_L \frac{R_{dc}\left(R_{dc} - R_{dc}^*\right)}{R_{dc}^2 - R_{dc}R_{dc}^* + R_{dc}^* R_L} \right)}{\left(1 + sC_L R_L\right)} \tag{64}$$

The open loop gain for frequencies greater than the pole and zero frequencies in the above expression with the assumption that the remote-end capacitance is large and the added simplification that the integrator zero is at a much higher frequency can be evaluated as:

$$\mathbf{T} \approx \frac{K_i}{s} \frac{\left(R_{dc} - R_{dc}^*\right)}{R_{dc}} \tag{65}$$

As the estimated cable resistance R_{dc}^* exceeds the actual line resistance R_{dc}, the phase at low frequencies above DC goes below -180° even though the gain is over 0 dB (due to the high integrator gain), thus leading to instability. When the estimated cable resistance is smaller than the actual line resistance, the system is unconditionally stable. The phase margin of the control loop gets degraded though with increased capacitance leading to reduced stability margins (translates in simple terms to severely under-damped behavior). Note that the system can be stabilized by reducing the integrator gain and letting the gain go below 0 dB before the loop gain crosses -180°; but lowering the integrator gain would reduce the speed of the system response leading to a requirement of more current to be delivered or absorbed by the capacitor during the transient.

An experimental verification of the instability phenomenon with large remote-end capacitance was performed with a resistive load switched between 350 Ω and 5 kΩ using Cable-2 with a large remote-end capacitance of 47 μF. The line resistance measured using a voltmeter during this particular experiment was 332 Ω. Figure 93, Figure 94 and Figure 95 show the system response with the estimated resistance at 320 Ω, 330 Ω and 340 Ω. It can be seen that while the system is stable at the lower estimated resistance, the higher estimated resistance leads to control instability validating the analysis performed earlier in this section. The remote-end bulk capacitance not only slows down the transient response of the system but also leads to instability in certain cases. Active clamping methods that alleviate these problems are investigated in the next section.

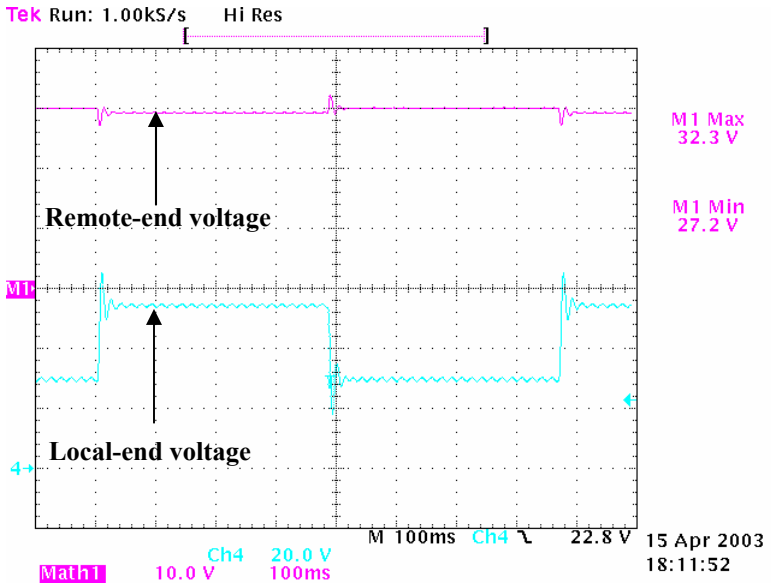

Figure 93: System response with remote-end capacitance of 47 µF and $R_{dc}^{*} < R_{dc}$

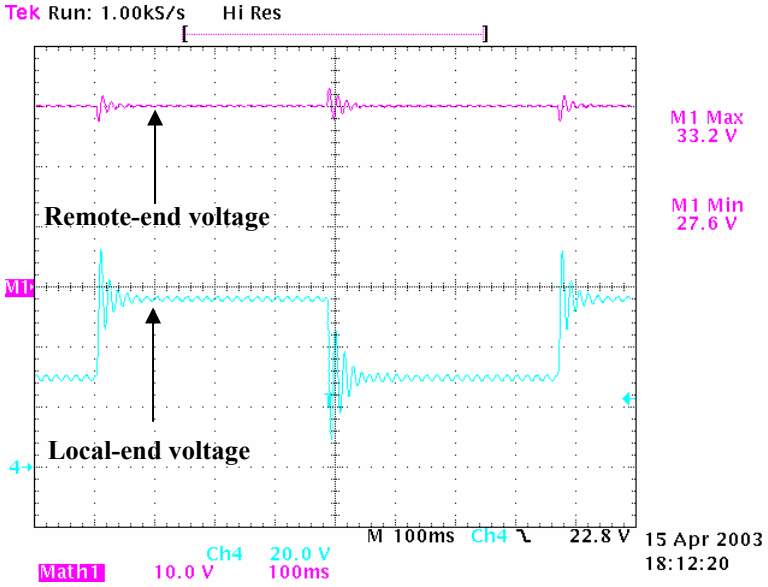

Figure 94: System response with remote-end capacitance of 47 µF and $R_{dc}^{*} \approx R_{dc}$

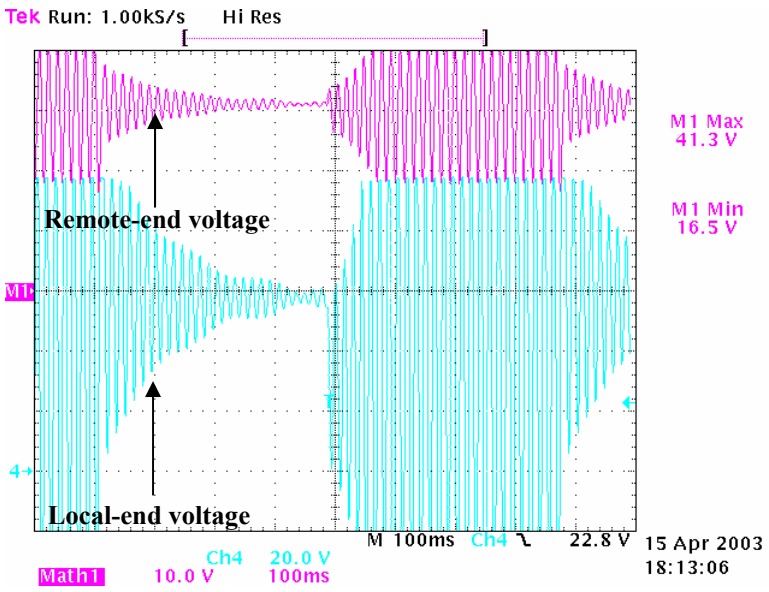

Figure 95: System response with remote-end capacitance of 47 μF and $R_{dc}^{*} > R_{dc}$

6.8.2. Diode-Capacitor Active Voltage Clamping

In the earlier section, we saw the effect of increased remote-end bulk capacitance on system instability though it reduces voltage transient magnitudes. Since at steady state, the remote-end capacitance is not required due to the local-end controller, back-to-back diodes can be used in series with a capacitor to clamp the voltage. In this way, the capacitance is included in the circuit only during transients and does not play a role when the load is constant. Figure 96 shows the clamping unit used in parallel with the load at the remote-end. When the remote-end voltage rises above or falls below the clamp capacitor voltage (which is the nominal remote-end voltage) by the diode conduction voltage (~0.65 V), the corresponding diode D1 or D2 is forward biased and the capacitance clamps the remote-end voltage. With a large capacitance, the remote-end voltage does not rise or fall by more than 0.65 V over the nominal voltage. With lower capacitance, the clamp voltage is not constant and a larger variation on the remote-end voltage is obtained. With appropriate choice of the capacitance, the swings in the remote-end voltage can be restricted to within +/-10%.

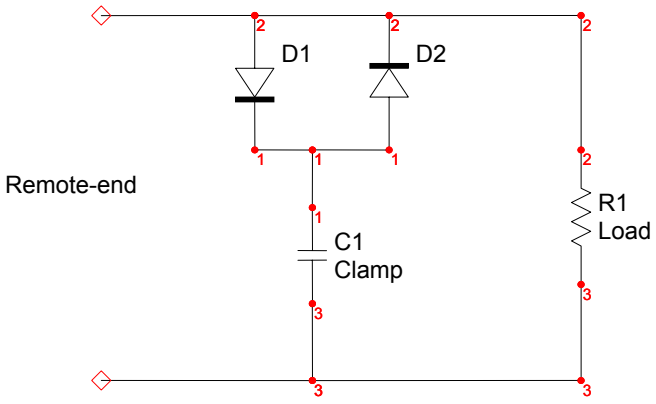

Figure 96: Active diode-capacitor clamp

The capacitor-diode active clamp was tested using Cable-2 for the case of a resistive load switched between 5 kΩ and 350 Ω. The clamp capacitor used was 47 μF. The nominal head voltage was 29.0 V. Figure 97 shows the local-end and remote-end voltage responses with the clamp capacitor connected. Comparing Figure 97 with Figure 92, it can be observed that using the capacitor actively (i.e. with back-to-back diodes) or passively, the same amount of reduction in the magnitude of the transient spikes is obtained; but the active clamp for the same amount of capacitance recovers to the nominal voltage much faster (Note the difference in scales in Figure 92 and Figure 97).

The experimental results indicate the need for simulation models to accurately design for the active clamp capacitor for a particular tolerance level in voltage transients. The nonlinear clamp model was implemented along with the closed loop system model in MATLAB and a simulation comparison of the diode clamping circuit using the cable model was performed using the experimental parameters. Note up to now all models used were linear though we were switching between different linear models corresponding to different loads. Figure 98 and Figure 99 show the remote and local-end voltage responses with the diode clamp for the simulated and experimental systems respectively. The experimental waveforms show that the cable DC resistance was not exactly matched; this was replicated in the simulation waveform by adjusting for the steady state values (note the difference in steady state voltages for the light load and matched load cases).

The spikes in the simulated waveform were due to the simulation of the diodes as on-off models with a forward drop of 0.65 V. An elimination of these spikes would be possible by the usage of better diode models. The simulation responses are similar to the experimental waveforms in terms of the transient voltage reduction provided by the clamp circuit and the settling time thus validating the simulation and design methodologies.

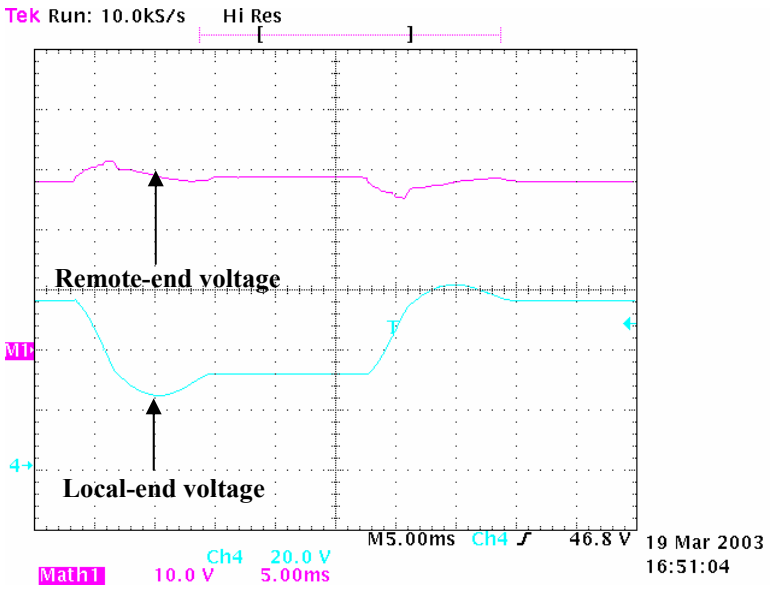

Figure 97: Active diode-capacitor clamp responses

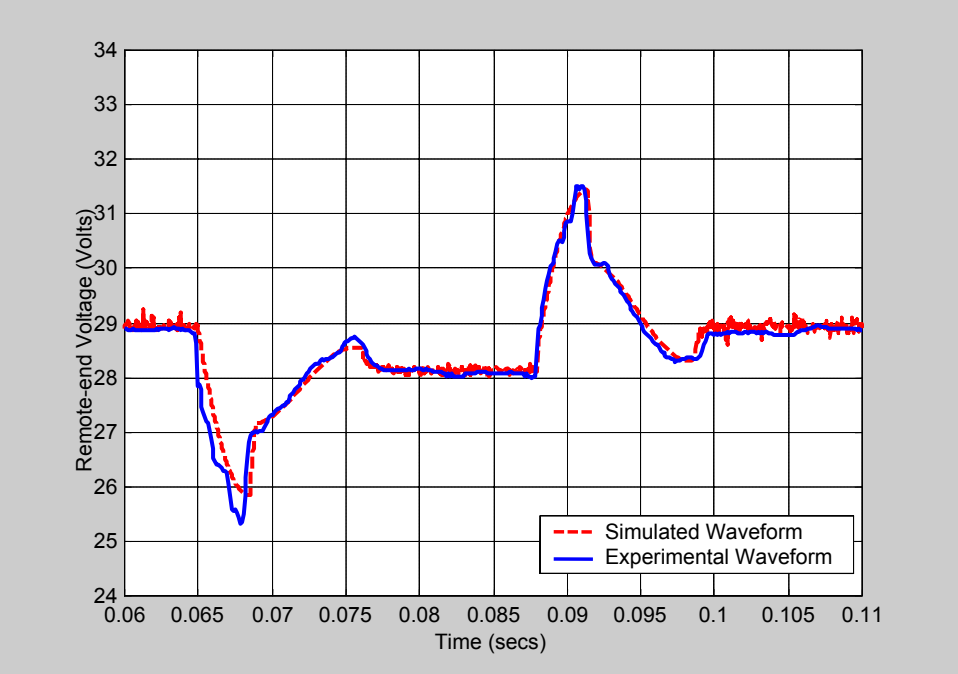

Figure 98: Remote-end voltage response comparison with active diode-capacitor clamp

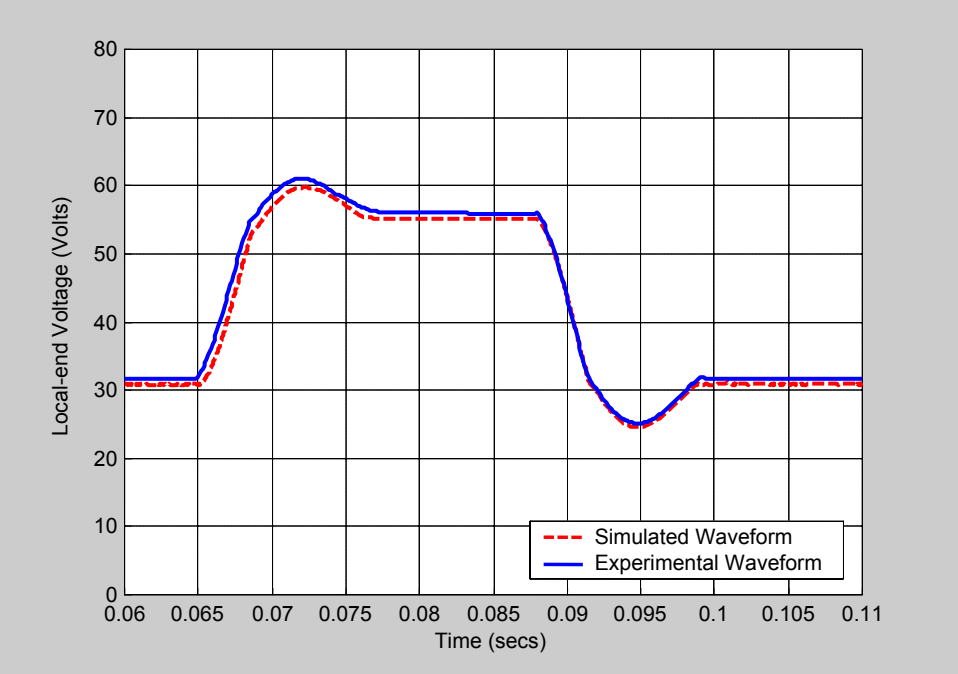

Figure 99: Local-end voltage response comparison with active diode-capacitor clamp

6.8.2.1. Power dissipation in clamping diodes

The power dissipation in the clamping diodes is an important consideration that needs to be evaluated for design purposes. The current supplied by the clamping capacitor during the transient can be approximated by a triangular waveform while the voltage across the diode is constant at its forward voltage (V_D). Hence, the energy dissipated in the diodes can be calculated as:

$$E_D = \frac{1}{2} V_D \Delta I \, t_{clamp} \; ; V_D \approx 0.65V \tag{66}$$

where ΔI is the change in load current and t_{clamp} is the time of clamping diode conduction (approximately 1~2 ms). Assuming that the load is switched from maximum load to no load with a frequency f_S, the ratio of power dissipated in the clamping diodes to the power delivered to the remote-end can be calculated as:

$$\frac{P_D}{P_R} = \frac{\frac{1}{2} V_D \Delta I \, t_{clamp} f_S}{\frac{1}{2}\frac{V_D^2}{R_L}} = \frac{\frac{1}{2} V_D \frac{V_R}{R_L} t_{clamp} f_S}{\frac{1}{2}\frac{V_D^2}{R_L}} = \frac{V_D}{V_R} t_{clamp} f_S \tag{67}$$

The ratio of the power dissipated in the diode to the power delivered is inversely proportional to the remote-end voltage and is directly proportional to the frequency of switching of the load. If the load switching is at low enough frequency compared to the time of diode conduction t_{clamp}, the power dissipated in the diodes is practically negligible at high remote-end voltages.

6.8.2.2. Choice of clamping capacitance

Remote-end voltage transients are influenced by the cable DC resistance and choice of the clamping capacitance. A simulation-based approach was undertaken to determine the influence of the cable resistance value on the capacitance required for regulation within a certain tolerance value of +/- 10 %. Cable-2 was used as the base model and the value of the DC resistance used in the models was changed over the range of 50 to 600 Ω i.e. the transfer functions were retained the same and only the cable resistance was changed. Note that this is not an ideal practical situation since the cable parameters would realistically be different in each case; the test case was only used to

illustrate the impact of the cable resistance on the choice of clamp capacitance and identify possible trends. The load was always switched between open load condition and matched impedance (i.e. the load transitions was between zero power and maximum power). Simulations were run by varying the clamp capacitance for different cable impedances and the remote-end over-voltages were studied. Figure 100 shows a comparison of the clamp capacitances required for cable DC resistances in the range of 50 to 600 Ω.

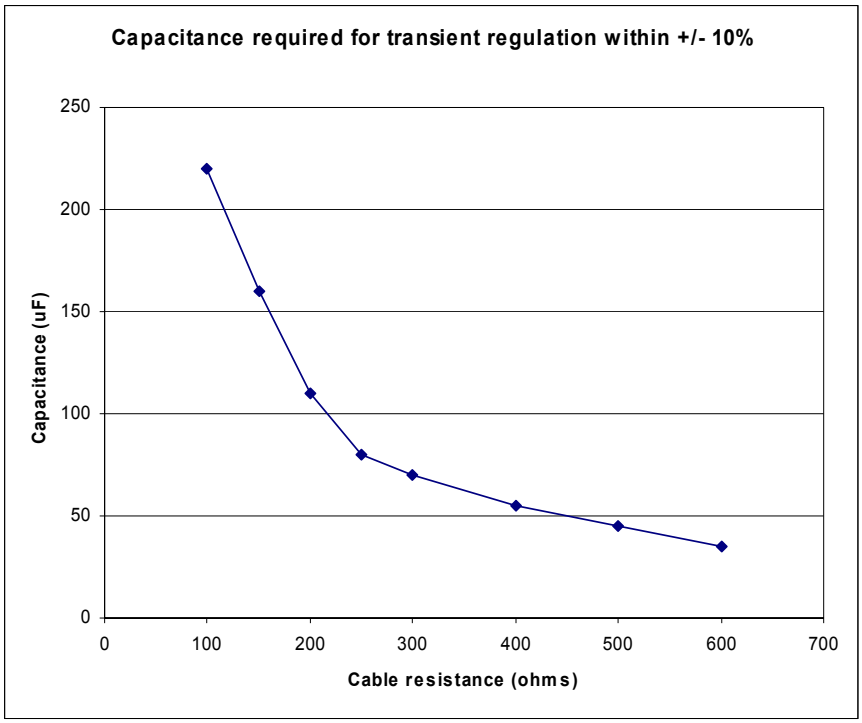

Figure 100: Clamp capacitance requirement with different cable resistances

From Figure 100 we can infer an inverse relationship between the capacitance required and the cable resistance. A simple theoretical model can be used to verify this conclusion. Consider the simple case of the line with a matched load being suddenly open-circuited shown in Figure 101. The local-end supply cannot react due to the transmission line delay, and the entire change in load has to be sustained by the clamp capacitance. So, the capacitance sees no load current (since the load is now open circuited) but has an input current corresponding to the matched load condition (since the

local-end supply has not reacted yet). The dynamics of the capacitor after the load is open circuited (neglecting the diodes in the circuit) can be expressed as:

$$C\frac{dv_R}{dt} \approx I_{matched} \approx \frac{V_R}{R_C} \tag{68}$$

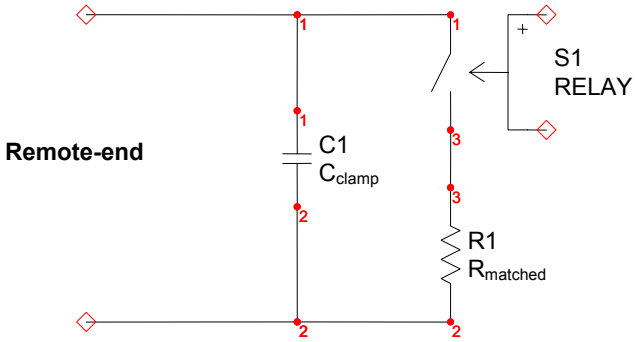

Figure 101: Simple remote-end model for transient calculations

With the assumption that the local-end supply reaction time Δt is approximately constant and independent of the cable resistance, the capacitance required for an allowable over-voltage can be found to be:

$$C_{\min} \approx \frac{V_R \Delta t}{\Delta V_R}\frac{1}{R_C} \tag{69}$$

It is clear from the above expression that we can expect an inverse relationship between the clamping capacitance required and the cable resistance. Note that the capacitance determination was made not on the basis of the same load but for the same matched load condition. Similar conclusions can be reached when the maximum load is applied from an open circuited condition. The amount of capacitance required with reduced cable resistances is high and other dissipative solutions need to be explored.

6.8.3. Zener Diode Voltage Clamping

Using a capacitance, either in passive or active (diode clamp) mode, leads to increased transient recovery time though the magnitude of the transients is reduced. Also, the presence of capacitance can lead to instability of the remote-end voltage. Further as was seen in the previous section, with reduced line impedance the amount of clamp capacitance required for a particular reduction in remote-end over and under-voltages rises sharply. Instead of using capacitors, we could use dissipative solutions such as a zener diode or a MOS-controlled shunt dissipator. The control loop stability should not be hindered in this case and the transient recovery time of the remote-end voltage should be the same as without transient compensation. If the transient time is maintained to be small compared to the frequency of switching of the loads, the power dissipation would be minimal.

The zener clamp was tested for the case of power transmission through Cable-2 with a 34 V zener for a nominal remote-end voltage of 30 V. For a quick reference, Figure 102 shows the remote and local-end voltage waveforms without a zener clamp. Figure 103 shows the system response with the 34 V zener diode clamp. The over-voltage transient is clamped at approximately 34.5 V without much change in the dynamics of the system.

The current supplied by the zener diode during the transient can be approximated by a triangular waveform while the voltage across the zener diode is constant at the clamped voltage. Hence, the energy dissipated in the zener diode can be calculated as:

$$E_Z = \frac{1}{2} V_{clamp} \Delta I \, t_{clamp} \tag{70}$$

where V_{clamp} is the zener clamping voltage, ΔI is the change in load current and t_{clamp} is the time of zener diode conduction (approximately 1~2 ms for Cable-1 and Cable-2). Assuming the clamp voltage is k times the actual remote-end voltage (V_R) and the load is switched from maximum load to no load with a frequency f_S, the ratio of power dissipated in the zener to the power delivered can be calculated as:

$$\frac{P_Z}{P_R} = \frac{\frac{1}{2} V_{clamp} \Delta I \, t_{clamp} \frac{f_S}{2}}{\frac{1}{2}\frac{V_R^2}{R_L}} = \frac{\frac{1}{2} k V_R \frac{V_R}{R_L} t_{clamp} \frac{f_S}{2}}{\frac{1}{2}\frac{V_R^2}{R_L}} = \frac{1}{2} k t_{clamp} f_S \tag{71}$$

The ratio of power dissipated in the zener diode is independent of the remote-end voltage (as long as k the over-voltage factor is maintained constant) and is directly proportional to the frequency of switching of the load. The factor 0.5 is indicative that the clamp works only in the positive direction. If the load switching is at low enough frequency compared to the time of zener conduction t_{clamp}, the power dissipated in the zener is practically negligible. Notice the difference in this efficiency factor between the diode-capacitor clamping where the ratio is inversely proportional to the remote-end voltage. The diode-capacitor clamp is more efficient than the zener diode clamp but the zener clamp has the advantage of faster transient dynamics. Also, a MOSFET controlled shunt regulator that is turned on when the actual remote-end voltage is greater than k times the nominal head voltage could be used in place of the zener diode if power dissipation in the zener diode is an issue at high temperatures.

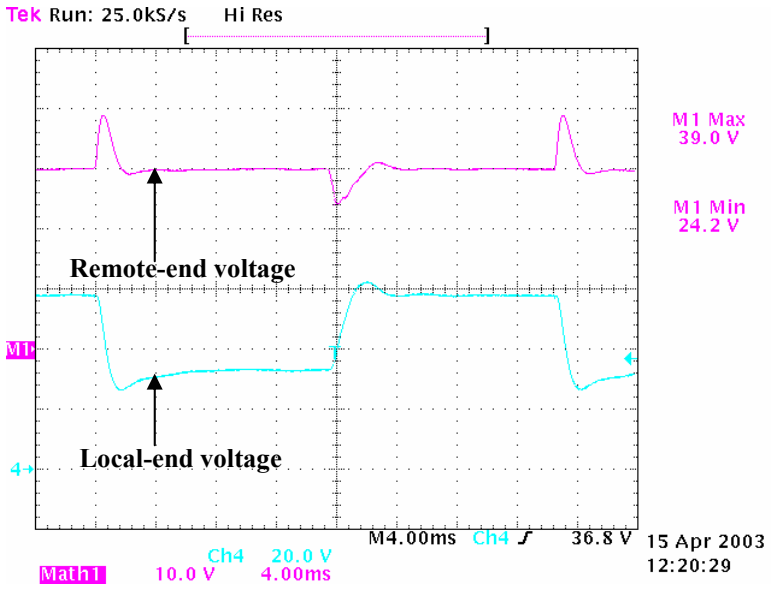

Figure 102: System response without zener diode clamp

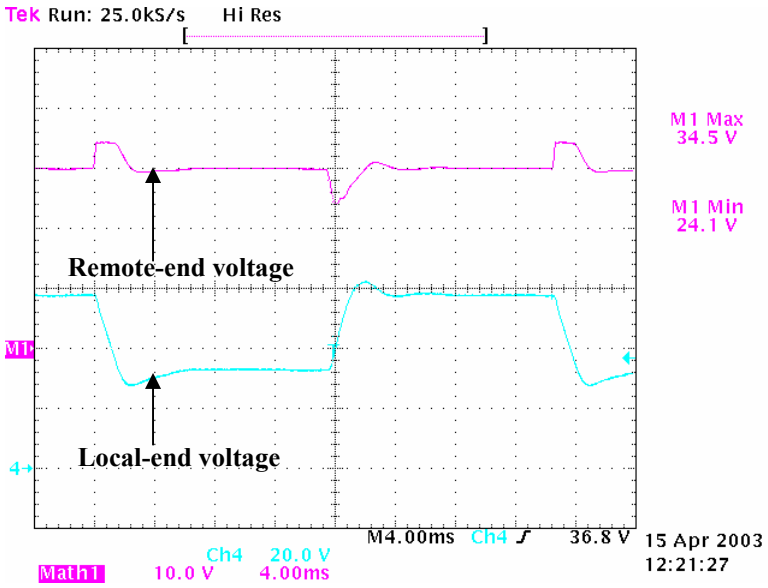

Figure 103: System response with zener diode clamp

6.8.4. Remote-end Current Slew Rate Control

From the previous sections, it is clear that voltage transients cannot be eliminated if the load is abruptly turned on and off. Also, using capacitors or zener diodes to reduce voltage transients result in energy losses during transients. On the other hand, the change in load current can be limited to certain slew rates to maintain the remote-end voltage within +/-10% of nominal voltage without the need for large capacitors. For example, the loads can be ramped up or down by using small DC motors in torque controlled mode at startup. Further, if switching converters with current mode control are used, it is possible to limit the load slew rates of the individual converters to ensure a maximal slew rate at the remote-end. The control loop and the converter output capacitor size would be impacted by a maximal slew rate on the loads and need to be factored in by tool designers. Control analysis and design considerations on load current control are presented below.

As can be seen from Chapter 6.4, the system response to changes in the load resistance is non-linear. On the other hand, the system response would still be linear if a constant current load is switched off and on. So, consider the remote-end voltage

response to changes in the load current. For ease of analysis, Y_L represents the filtering poles at the load end and I_o represents the current load. Recall the relations between the currents and voltages in the cable:

$$\begin{bmatrix} \mathbf{I}_L(s) \\ \mathbf{I}_R(s) \end{bmatrix} = \begin{bmatrix} Y_{11}(s) & Y_{12}(s) \\ -Y_{12}(s) & -Y_{11}(s) \end{bmatrix} \begin{bmatrix} \mathbf{V}_L(s) \\ \mathbf{V}_R(s) \end{bmatrix} \tag{72}$$

The relationship between the voltage and current at the remote-end of the cable can hence be determined as below:

$$\mathbf{I}_R = \mathbf{I}_o + Y_L \mathbf{V}_R \Rightarrow \mathbf{V}_R = \frac{-Y_{12}}{Y_{11}+Y_L}\mathbf{V}_L - \frac{1}{Y_{11}+Y_L}\mathbf{I}_o \tag{73}$$

With this simplification for the load-side relationships, the local-end current equation can be simplified to:

$$\mathbf{I}_L = \left(Y_{11} - \frac{Y_{12}^2}{Y_{11}+Y_L}\right)\mathbf{V}_L - \frac{Y_{12}}{Y_{11}+Y_L}\mathbf{I}_o \tag{74}$$

Since the other aspects of the system are as explained in Chapter 6.4, the closed loop response of the local-end voltage can be given as below:

$$\begin{aligned} \mathbf{V}_L &= \frac{1}{1+\mathbf{T}_c+\mathbf{T}_v}\left((1+\mathbf{H}_I)\mathbf{V}_{R,ref} + \frac{\mathbf{H}_I Y_{12}}{Y_{12}^*(Y_{11}+Y_L)}\mathbf{I}_o\right) \\ \mathbf{T}_v &= -\mathbf{H}_I \frac{Y_{11}^*}{Y_{12}^*} \\ \mathbf{T}_c &= \mathbf{H}_I\left(\frac{1}{Y_{12}^*}\right)\left(Y_{11} - \frac{Y_{12}^2}{Y_{11}+Y_L}\right) \end{aligned} \tag{75}$$

The closed loop remote-end voltage response can be obtained as:

$$\mathbf{V}_R = \left(\frac{-Y_{12}(1+\mathbf{H}_I)}{(Y_{11}+Y_L)(1+\mathbf{T}_c+\mathbf{T}_v)}\right)\mathbf{V}_{R,ref} + \left(\frac{-1}{(Y_{11}+Y_L)} - \frac{Y_{12}^2\mathbf{H}_I}{Y_{12}^*(Y_{11}+Y_L)^2(1+\mathbf{T}_c+\mathbf{T}_v)}\right)\mathbf{I}_o \tag{76}$$

In the case of a well-modeled system, the cable model approximates the control loop model (at least at frequencies below or comparable with the loop bandwidth) *i.e.* $Y_{11}^{*} = Y_{11}$ and $Y_{12}^{*} = Y_{12}$. With this approximation, the system closed loop response can be simplified to be:

$$\mathbf{V}_2 = \left(\frac{\frac{-Y_{12}}{(Y_{11}+Y_L)}(1+\mathbf{H}_I)}{\left(1-\frac{Y_{12}\mathbf{H}_I}{(Y_{11}+Y_L)}\right)} \right) \mathbf{V}_{ref} - \left(\frac{\frac{1}{(Y_{11}+Y_L)}}{\left(1-\frac{Y_{12}\mathbf{H}_I}{(Y_{11}+Y_L)}\right)} \right) \mathbf{I}_o \tag{77}$$

The error in the remote-end voltage can now be defined as:

$$e = \mathbf{V}_R - \mathbf{V}_{R,ref} = \frac{\left(-1-\frac{Y_{12}}{(Y_{11}+Y_L)}\right)\mathbf{V}_{R,ref} - \frac{\mathbf{I}_o}{(Y_{11}+Y_L)}}{\left(1-\frac{Y_{12}\left(K_p+\frac{K_i}{s}\right)}{(Y_{11}+Y_L)}\right)} \tag{78}$$

The static errors resulting from step and ramp excitations of the load current can be determined using Laplace Transform theory [36]-[37]. The filter poles at the load end can be approximated by an open circuit (*i.e.* $Y_L = 0$) and the low frequency values of Y_{11} and Y_{12} by $1/R_{dc}$ and $-1/R_{dc}$ respectively where R_{dc} represents the DC resistance of the cable.

Step Excitation:

$$E_S = \lim_{\substack{s\to 0 \\ I_o = \frac{1}{s}}} (s.e) = -\lim_{s\to 0} \frac{sR_{dc}}{\left(1+\left(K_p+\frac{K_i}{s}\right)\right)} \cdot \frac{1}{s} = 0 \tag{79}$$

Ramp Excitation:

$$E_R = \lim_{\substack{s\to 0 \\ I_o = \frac{1}{s^2}}} (s.e) = -\lim_{s\to 0} \frac{sR_{dc}}{\left(1+\left(K_p+\frac{K_i}{s}\right)\right)} \cdot \frac{1}{s^2} = \frac{-R_{dc}}{K_i} \tag{80}$$

The closed loop circuit was simulated for Cable-1 with the load current ramped up from 1 mA (corresponding to 5.11 $k\Omega$ at the remote-end) to 7.5mA (corresponding to 670 Ω) and vice versa. The remote-end voltage was maintained nominally at 5V with an integrator gain of 6800. From the analysis in the previous section, the ramp error in the remote-end voltage can be assessed as shown below:

$$V_{error} = \pm \frac{R_{dc}}{K_i} \frac{\Delta \mathbf{I}_o}{\Delta \mathbf{t}} \tag{81}$$

The load voltage is maintained within +/-10 % of the nominal voltage i.e. V_{error}=0.5 V. With this in mind, the time over which the load current needs to be ramped up and down can be calculated as:

$$\Delta \mathbf{t} = \frac{R_{dc}}{K_i} \frac{\Delta \mathbf{I}_o}{V_{error}} = \frac{670\Omega}{6800/s} \frac{6.5mA}{0.5V} \approx 1.3ms \tag{82}$$

The time domain waveforms of the simulated load (remote-end) current and voltage are shown in Figure 104 and Figure 105 respectively. From the simulation results, it can be seen that the remote-end voltage increases/decreases by 0.5V over the nominal voltage of 5V. Beyond this point, the local-end voltage control can match the increase/decrease in remote-end current leading to a constant remote-end voltage. Once the remote-end current demand is constant (after the ramp up/down), the local-end controller rapidly brings down the remote-end voltage to the nominal voltage. With this understanding of the control, the maximum load slew rate the system can handle can be given in terms of the system parameters to be:

$$\left(\frac{\Delta \mathbf{I}_o}{\Delta \mathbf{t}} \right)_{\max} = \frac{K_i}{R_{dc}} \Delta V_R \tag{83}$$

where ΔV_R corresponds to the allowable remote-end transient over/under voltage i.e. difference between maximum or minimum remote-end voltage allowed and the nominal remote-end voltage.

From the above discussion it is clear that static error in the remote-end voltage can be eliminated by using an integrator (1/s) term. With the integrator, we have a ramp error in the remote-end voltage that is dependent on the cable resistance, integrator gain and the slew rate of the load. We could try to remove this voltage error by introducing a $1/s^2$ term in the feedback. But, introducing the $1/s^2$ term would imply a 180° phase shift

in the loop gain leading to negligible phase margin at low frequencies and we would not be able to stabilize the system. With this understanding, it is clear that voltage ramp error will always be present and its implications on the slew rate of the load should be kept in mind in the design of the remote-end power converter. Further, slew rate control of the remote-end load currents is the most optimal remote-end voltage transient compensation method without additional components. The only disadvantage of this method is the requirement for slewing the load changes that may not be possible in some high-speed systems.

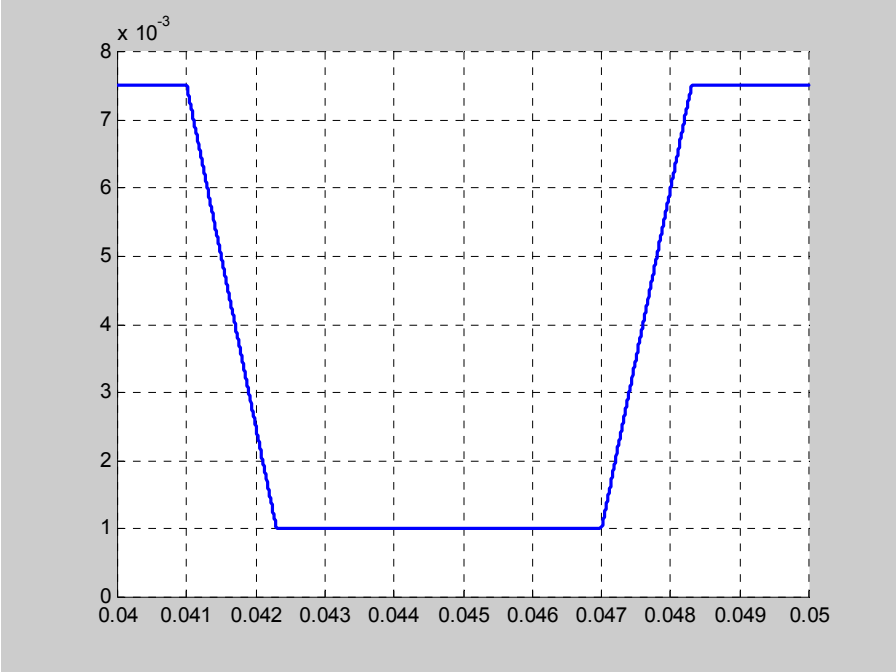

Figure 104: Simulated remote-end current

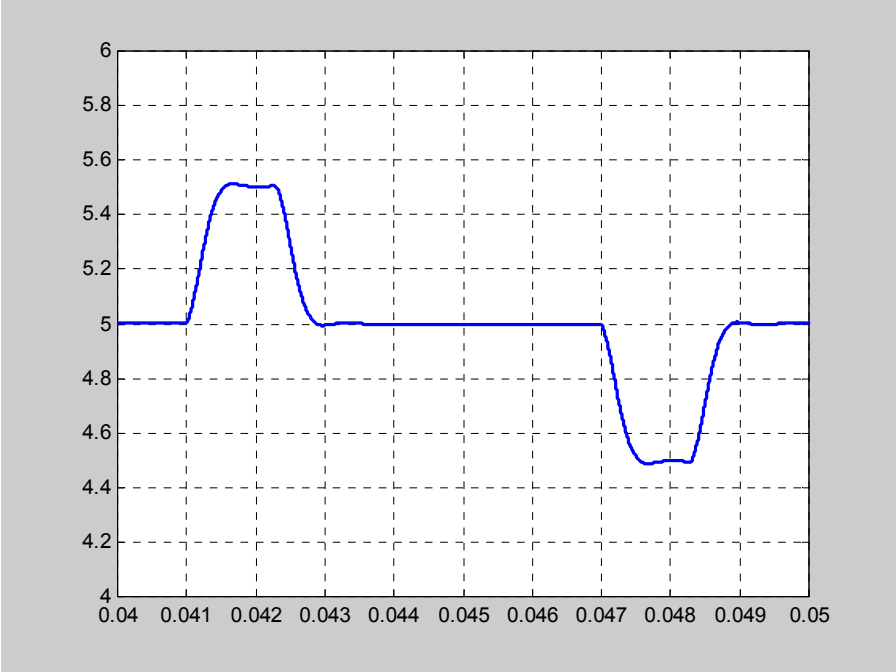

Figure 105: Simulated remote-end voltage

6.9. Global closed loop model inversion controller

The voltage controller as explained in the previous sections is based on knowledge of the cable characteristics. The cable characteristics need to be adaptable for practical implementations requiring usage with different cables and operating conditions (for example at higher temperatures). Feedback of the remote-end voltage and current using a slow telemetry link could be used to update the cable model in the controller thus leading to a closed loop model inversion controller (in this case the term "*closed loop*" refers to a feedback loop that updates the cable model) . A conceptual perspective of the closed loop model inversion controller is shown in Figure 106.

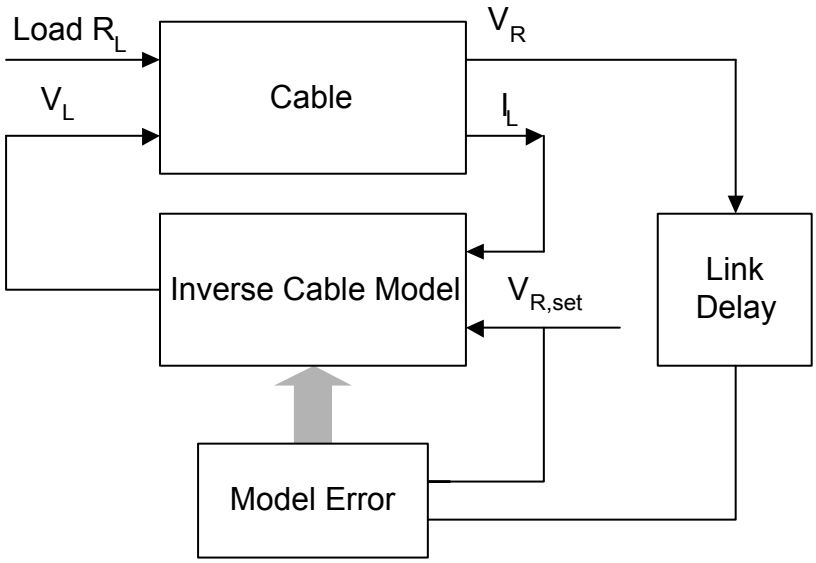

Figure 106: Conceptual model inversion perspective of the adaptive global controller

6.9.1. Adaptation possibilities

The transmission line models used in the feed-forward compensator are frequency dependent; hence, a true model update would require the usage of a frequency perturbation at the local-end and the adaptation of the model through an examination of the particular frequency components in the remote-end voltage and current spectrum. Though this would be possible before the startup of the system, it would be hard to implement this model update algorithm in practice once the system is in operation. In cases where it is not possible to update all the parameters through feedback of the remote-end current and voltage, only the parameters that influence the steady state component (dc component) are updated through the feedback loop. The system is characterized before the start of operation, and the update of the cable model can be limited to updating the DC resistance of the cable as a first approximation. This adaptation rule assumes that the variation of other parameters in the model is independent or slowly varying with respect to time and temperature changes. This model adaptation algorithm shall be studied from a simulation perspective in the next section.

6.9.2. Simulation analysis of control approach

Update of the cable model limited to updating the cable resistance was tested out in simulations where there was a 5% difference between the actual cable characteristics and the cable model. Cable-2 was used in the simulations with the load being switched between 5.11 kΩ and 350 Ω. Before time t=200 ms it can be seen from Figure 107 that the model estimate and the actual remote-end voltage do not coincide leading to the remote-end voltage stabilizing at 27 V instead of 30 V. After the update of the model at t=200ms using the feedback from the telemetry link, the remote-end voltage attains the nominal reference voltage of 30 V and maintains this reference voltage at steady state even after load changes at t=220 ms and t=240 ms. Experimental implementations of the closed-loop model inversion controller would ideally be performed with collaboration with the industry and is recommended as a future research topic.

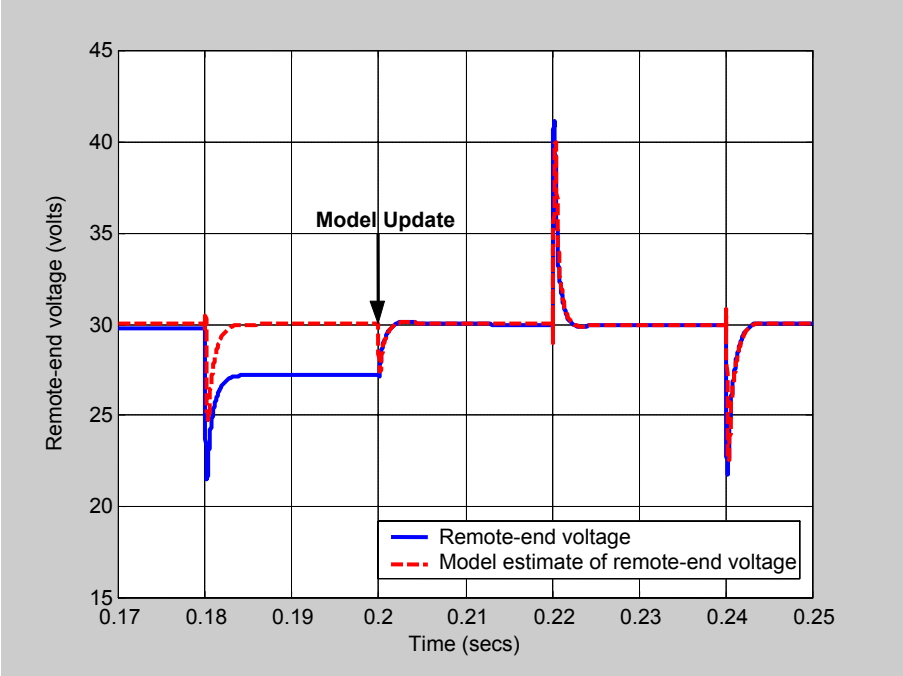

Figure 107: Simulated actual and estimated remote-end voltage responses

6.10. Conclusions

In this chapter, a new remote-end voltage control method based on model inversion was developed. The new remote-end voltage control was validated through simulation and experimental results for the two different cable arrangements. Design solutions were also presented for the optimal choice of parameters in the control. Remote-end voltage transient compensation methods based on capacitive and zener-diode clamps were evaluated. Also, slew rate control of the remote-end load current was studied and found to be the most optimal method for reducing remote-end voltage transients during load changes. To account for variations in cable parameters due to aging and temperature changes, a closed loop model inversion technique was developed. The system level based on updating the system model through measurements of the remote-end voltage obtained through a slow telemetry link was validated through simulations.

CHAPTER 7

SUMMARY AND RECOMMENDATIONS

7.1. Summary and contributions

Efficient power delivery in systems with lossy cables or interconnects is complicated and difficult to achieve. Existing methods for power conversion at the remote-end in these systems are either inefficient or unstable at high loads. Past attempts have primarily assumed that the influence of the resistance of the cables on the power delivered is insignificant compared to the other passive elements. In this work, these systems are analyzed and approaches for increasing the power delivered to the loads at the remote-end are developed. The main aspects and contributions of this work are listed below:

- The present work addresses significant problems existing in power delivery to remote instrumentation such as in oil wells, underwater vehicles, etc. and in distributed systems such as those used in aircrafts and submarines.
- Detailed studies and theoretical analyses of limitations of existing remote power conversion methods for lossy cables have been performed.
- Unreported phenomena such as load cycling and voltage jumps during startup of the system with a switching converter at the remote-end were discovered and validated through theoretical analysis and experimental work.
- The operation of remote instrumentation with existing remote power conversion methods at sub-optimal remote-end voltages (that is at voltages less than half the local-end voltage limit) impacts the maximum power delivered. For this scenario, methods based on state feedback control and parallel operation of linear and switching regulators with integrated control were developed to increase the power delivered to the remote-end while ensuring stable operation.

- The state feedback based voltage follower method increases the power delivered at the cost of output voltage regulation. The control method is simple and does not lead to any additional components in the system.
- The parallel operation of linear and switching regulators with integrated control also increases the power delivered to the remote-end. Though this method has the disadvantage of increased component count, this might be offset to a certain extent by the reduction in the filter elements of the switching regulator due to the inherent ripple cancellation in this method.

- Transmission line models that are accurate and can be implemented in a real-time control loop are essential for regulating the remote-end voltage by controlling the local-end voltage. New transmission line models based on s-domain approximations of transmission line transfer functions that alleviate the deficiencies of existing models were developed and validated experimentally.
- The necessity for system level control of the remote-end voltage for ensuring high efficiency and maximum power transfer was identified. Open loop model inversion controllers were developed to regulate the remote-end voltage against load disturbances. The controllers were extensively analyzed both on theoretical and experimental fronts.
- Irrespective of whether the system is operated at or below the optimal remote-end voltage, system level control is effective at increasing the efficiency of the system and reducing device stresses. Operation of remote instrumentation systems at sub-optimal remote-end voltages necessitates usage of new remote power conversion methods detailed in Chapter 4 with the system level control of the remote-end voltage.
- The remote-end voltage cannot be controlled during a short time determined by the delay in the transmission line. Voltage clamping methods were developed and verified experimentally to prevent over and under-voltages beyond an allowable range (normally +/-10 %). Further, the impact of slew rate control of load changes to reduce transients in remote-end voltage was investigated on a theoretical front and found to be the most effective. This slew rate control of the load could be easily achieved by operating the switching regulators in current mode control.
- To account for variations in cable parameters due to aging and temperature changes, a closed loop model inversion technique was developed. The system-level

global control was based on using remote-end voltage measurements obtained through a slow telemetry link to update the cable model of the open loop model inversion controller. The closed loop model inversion controller was validated through simulations.

7.2. Recommendations for future research

Some recommendations for future research on power delivery to remote instrumentation are listed as follows:

- A practical implementation of the linear regulator switcher parallel combination to operate with different cable lengths and DC resistances necessitates the usage of microcontrollers or digital signal processors (DSP). The microcontroller or DSP would be used to derive the control law for the switching regulator from measurements of the remote-end voltage, remote-end current, output voltage. The switcher is operated under current mode control with the reference current supplied by the microcontroller/DSP using the measurements. The cost of the control unit is low due to the availability of cheap DSPs and the existing availability of all the current and voltage signals (usually used in protection units). Also, the PWM unit for the switching regulator can also be integrated into the DSP functions reducing the number of components in the system. A typical practical implementation for the series regulator and switcher operating in parallel is shown in Figure 108.

- Remote-end voltage control methods based on model inversion are highly dependent on the accuracy of the transmission line models, particularly the cable DC resistance. The cable DC resistances are sensitive to temperature variations and an algorithm was developed in this work to update the cable DC resistance using remote-end voltage measurements obtained through a slow telemetry link. A practical implementation of this algorithm is needed to further understand the adaptation process. This would be best completed with industry collaboration due to the need for access to practical remote instrumentation systems. Also, theoretical approaches on algorithms for cable model-adaptation could be investigated. Algorithms based on recursive estimation could be used to obtain better updates of the cable model.

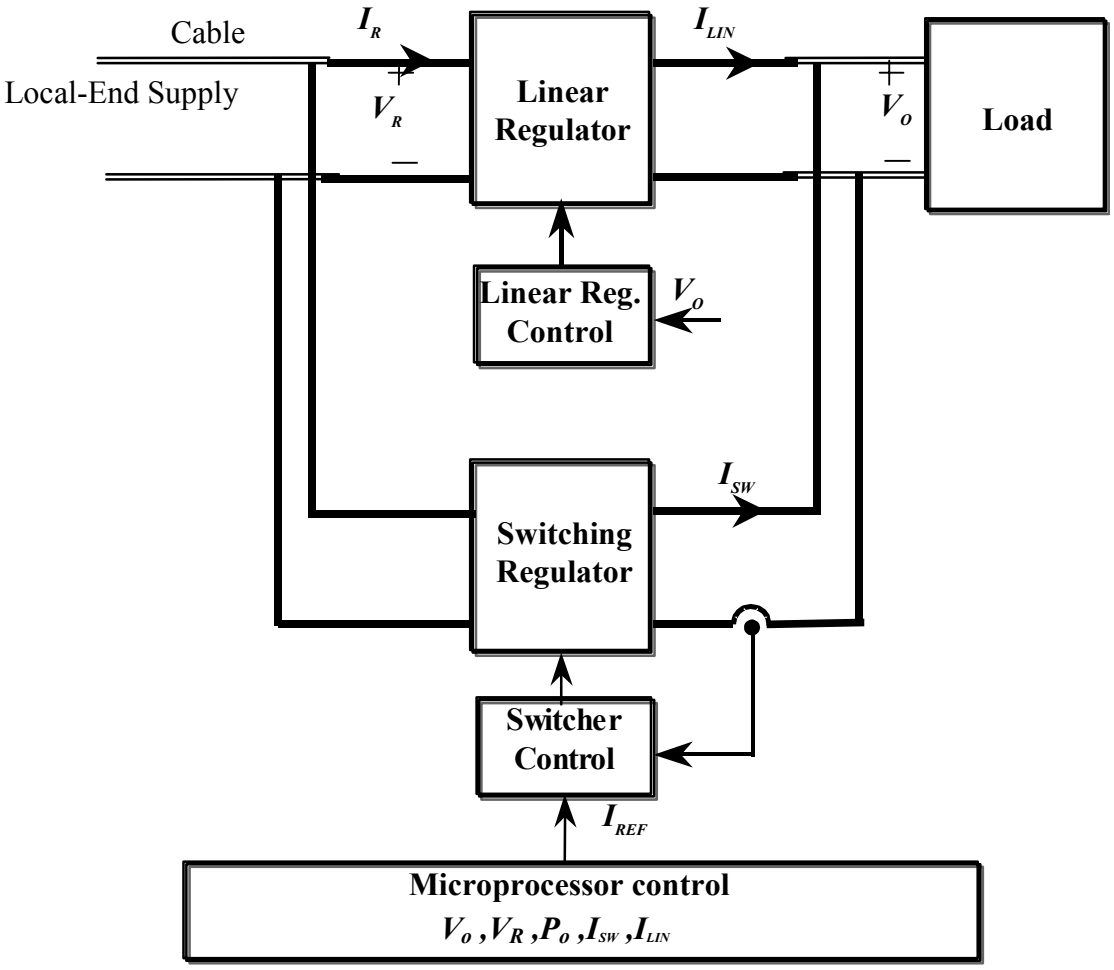

Figure 108: Control method for linear regulator-switcher parallel combination

- Remote-end voltage transient compensation units are required to reduce voltage transients during load changes that cannot be compensated by the model inversion control. The need for remote-end voltage transient compensation circuits would be eliminated if the load currents can be ramped up or down. Simulation results in this work show that if the load is ramped up or down in a certain time span, voltage transients can be reduced to within +/-10 % without the need for additional transient compensation units. An experimental verification of the theoretical analysis and simulation results presented in this work would be of much significance to industry.

APPENDIX A – CABLE PARAMETERS FOR CABLE-1

The cable parameters for Cable-1 are shown in the following figures. The presence of negative conductance values can be attributed to noise pickup from neighboring wires. The characterization of the line was difficult at low frequencies and values below 40 Hz are suspect.

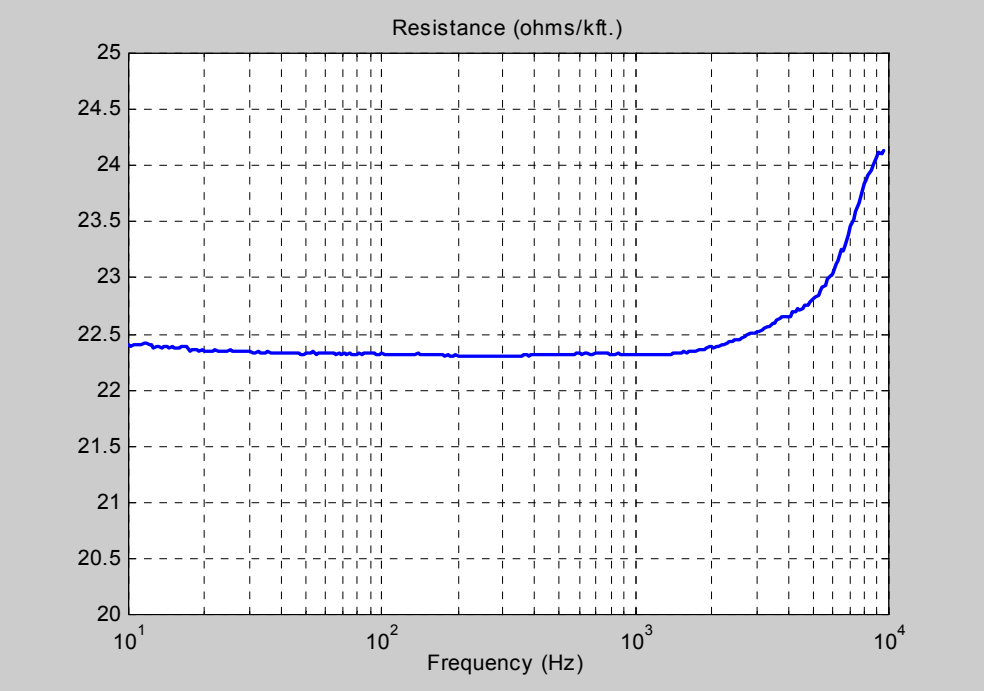

Figure 109: Per-unit resistance for Cable-1 (Ω/ Kft.)

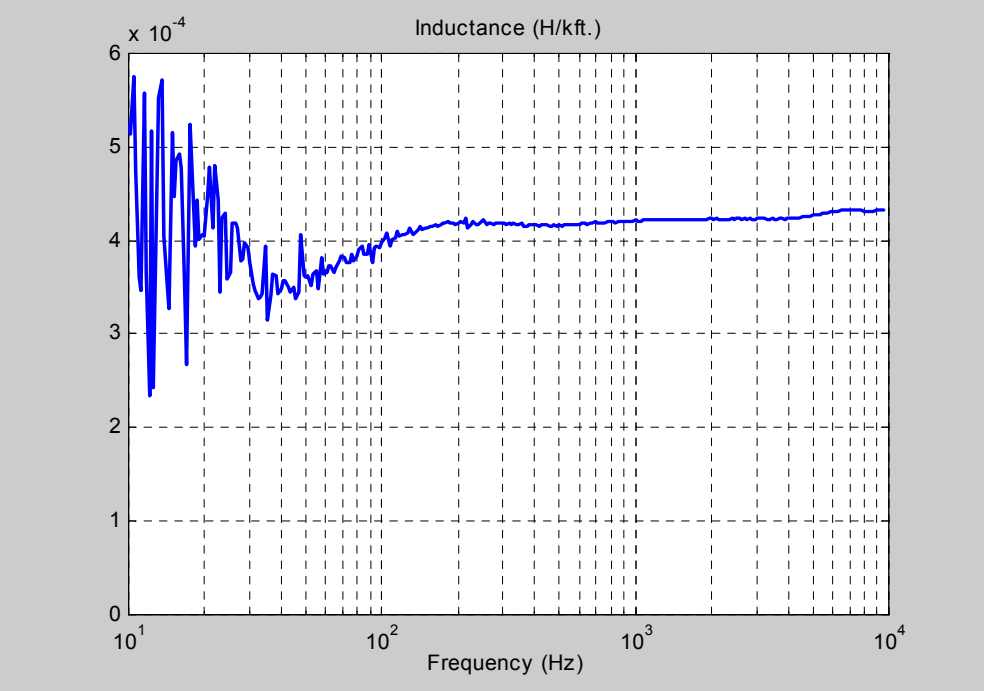

Figure 110: Per-unit inductance for Cable-1 (H/ Kft.)

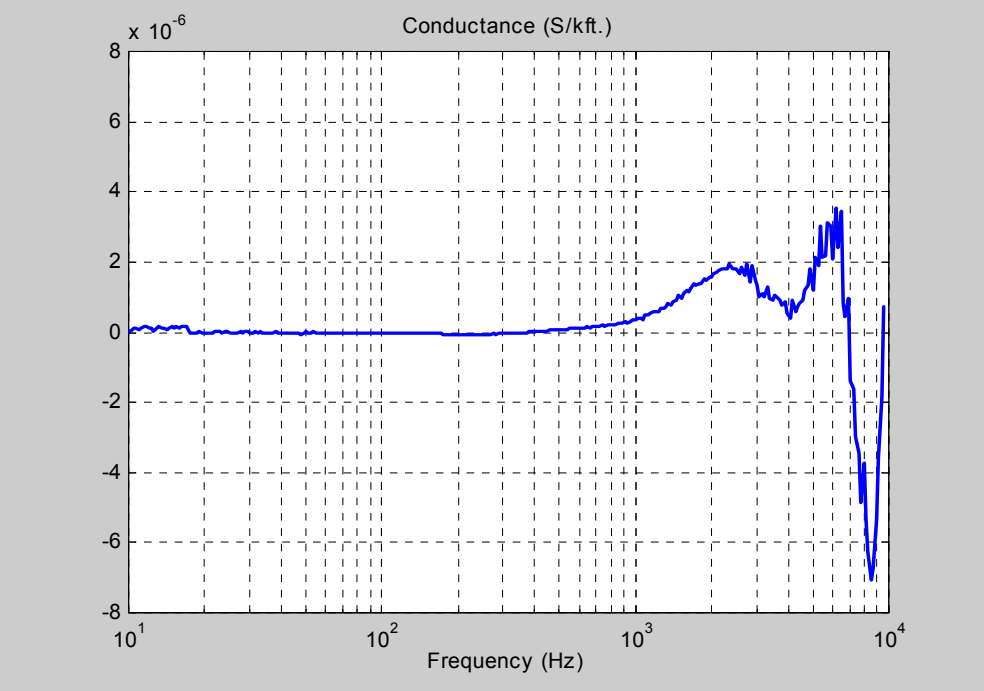

Figure 111: Per-unit conductance for Cable-1 (S/ Kft.)

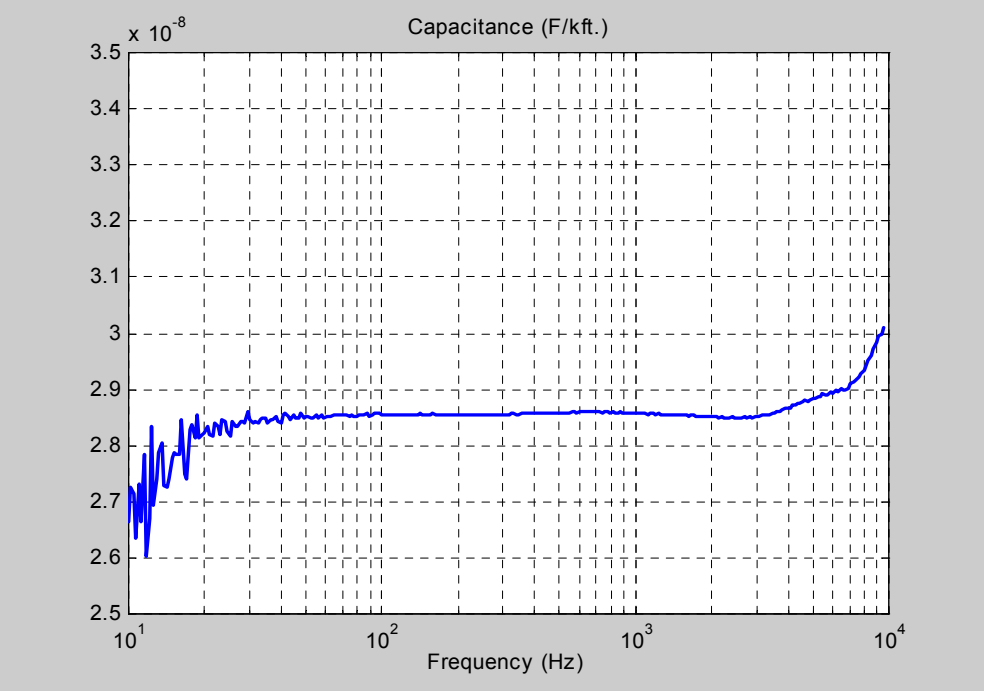

Figure 112: Per-unit capacitance for Cable-1 (F/ Kft.)

APPENDIX B – CABLE PARAMETERS FOR CABLE-2

The cable parameters for Cable-2 are shown in the following figures. The presence of negative conductance values can be attributed to noise pickup from neighboring wires. The characterization of the line was difficult at low frequencies and values below 40 Hz are suspect.

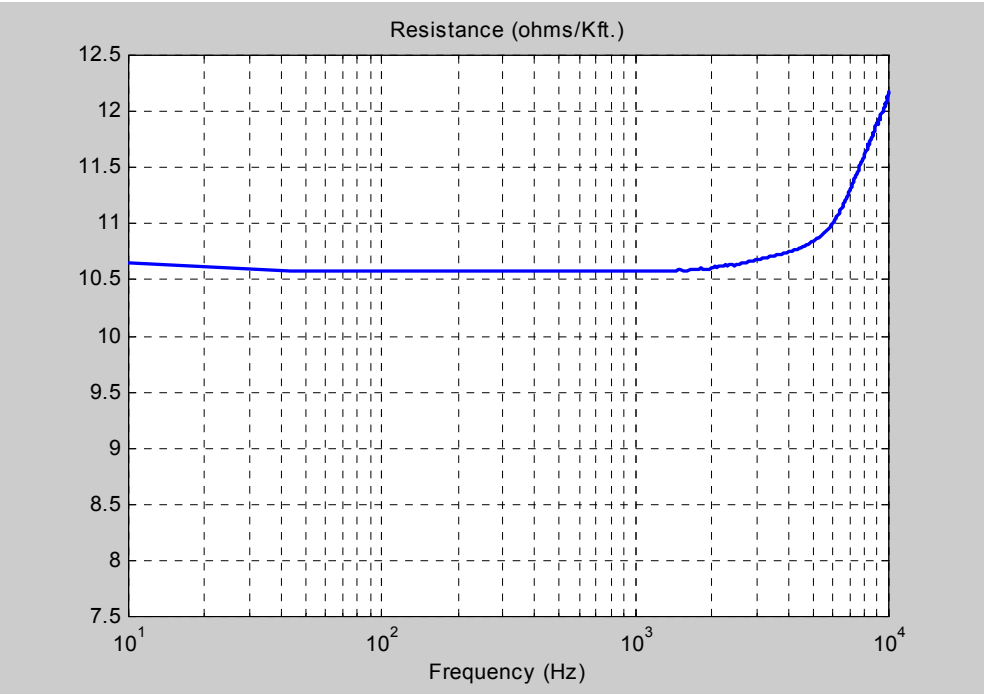

Figure 113: Per-unit resistance for Cable-2 (Ω/ Kft.)

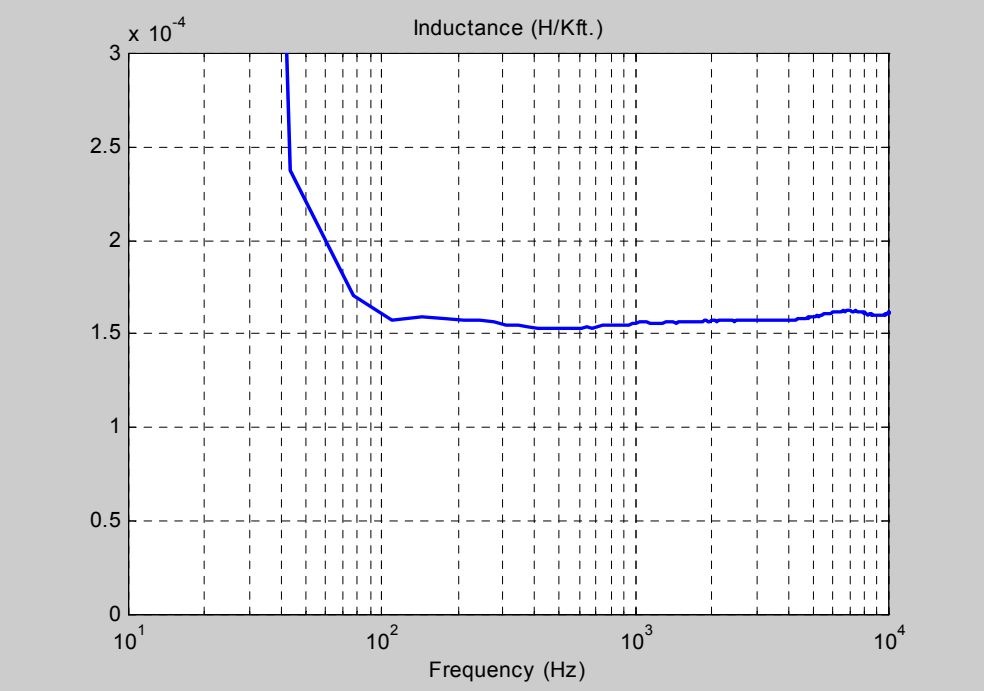

Figure 114: Per-unit inductance for Cable-2 (H/ Kft.)

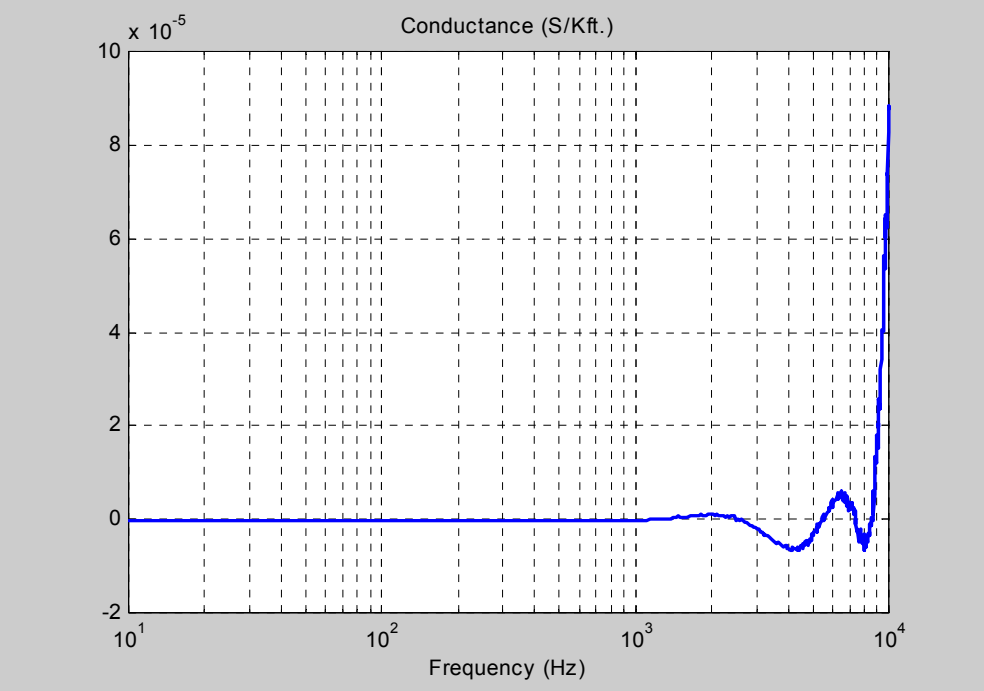

Figure 115: Per-unit conductance for Cable-2 (S/ Kft.)

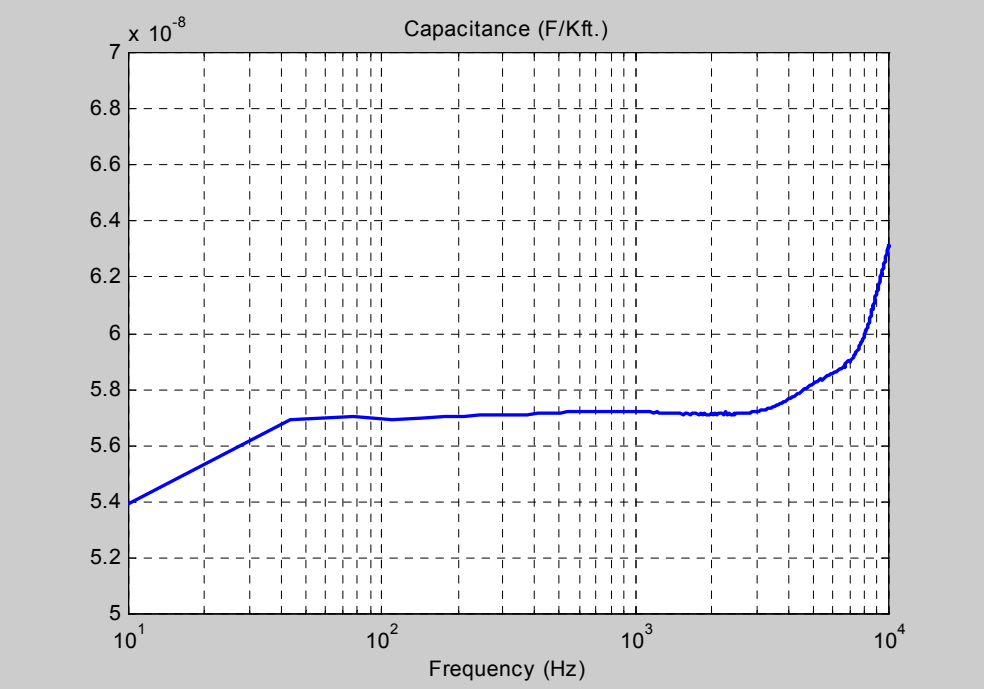

Figure 116: Per-unit capacitance for Cable-2 (F/ Kft.)

APPENDIX C – CABLE PARAMETERS APPROXIMATION FOR CABLE-2

The frequency domain fitting for the transmission line transfer functions corresponding to Cable-2 are shown in this section.

Y_{11} was approximated by a 1-pole/1-zero rational function as shown below:

$$Y_{11}(s) = \frac{1}{319.8}\left(\frac{1+\frac{s}{5026.5}}{1+\frac{s}{25761.1}}\right) \; mho \tag{84}$$

Note here that $Y_{11}(s)$ is the reciprocal of the short circuit impedance (Z_{sc}) as stated in Chapter 5 leading to the conclusion that we have a cable with a resistance of approximately 320Ω between the ends. Figure 117 compares the numerical fit to the experimental data for $Y_{11}(s)$. The admittance amplitudes are shown in dB (20*log10) since the numerical fitting procedure was performed using a log-log-scale. The variation in impedance between low and high frequencies was high leading to errors in the fitting if done using normal scales. The log-log scale reduces the variation in the fitting due to the logarithmic weighting and also gives a better perspective of the transfer functions in terms of poles and zeros. $Y_{12}(s)$ was approximated by a 7-pole/7-zero rational function shown below:

$$Y_{12}(s) = \frac{-1}{319.8}\left(\frac{1+\frac{s}{100531}}{1+\frac{s}{31415.9}}\right)\left(\frac{1-\frac{s}{37699.1}}{1+\frac{s}{37699.1}}\cdot\frac{1-\frac{s}{125663.7}}{1+\frac{s}{125663.7}}\cdot\frac{1-\frac{s}{314159.3}}{1+\frac{s}{314159.3}}\right)\cdot \left(\frac{1-\frac{s}{345575.2}}{1+\frac{s}{345575.2}}\cdot\frac{1-\frac{s}{408407.0}}{1+\frac{s}{408407.0}}\frac{1-\frac{s}{565486.7}}{1+\frac{s}{565486.7}}\right) \; mho \tag{85}$$

Figure 118 compares the numerical fit to the experimental data for $Y_{12}(s)$. Notice that the phase of $Y_{12}(s)$ keeps decreasing with frequency indicating the dispersion aspect of the transmission line. Since, the magnitude of $Y_{12}(s)$ seems to indicate a single pole roll-off in the frequencies between 100-10 kHz, $Y_{12}(s)$ was fitted using non-minimum phase zeros (right half plane zeros) and stable poles that cancel out in the magnitude response but lead to a decreasing phase with frequency. Note that this is similar to the approximation of a time delay into a rational function approximation.

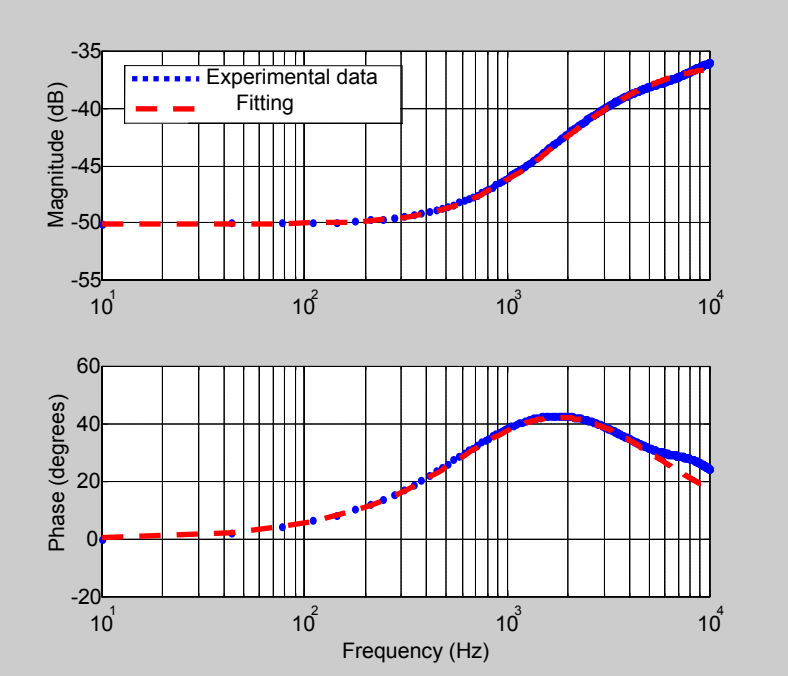

Figure 117: Y_{11} fitting for Cable-2

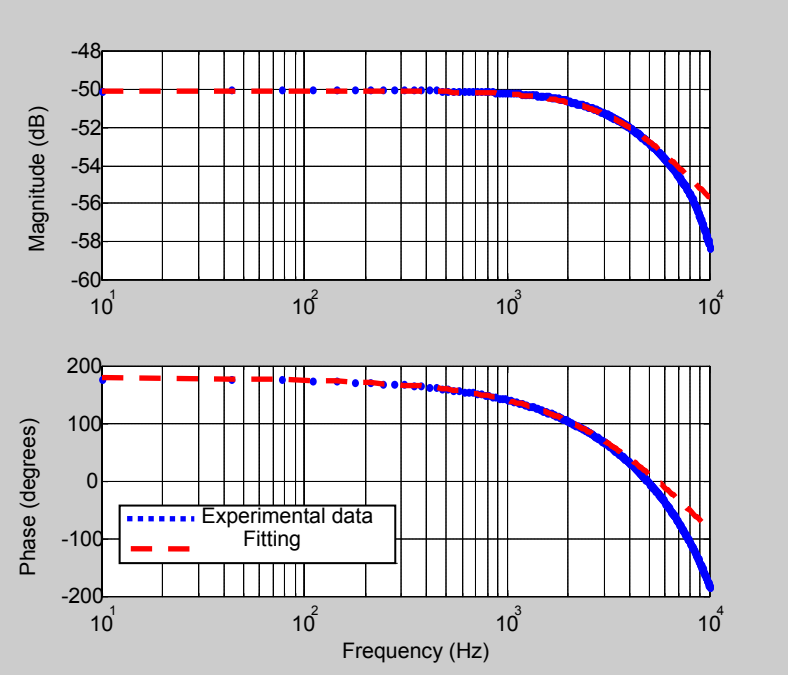

Figure 118: Y_{12} fitting for Cable-2

REFERENCES

[1] W. A. Tabisz, M. M. Jovanovic, and F. C. Lee, "Present and future of distributed power systems," *Proceedings of Applied Power Electronic s* Conference, pp. 11-18, 1992.

[2] A. Emadi, M. Ehsani, "Aircraft power systems: Technology state of the art, and future trends," *IEEE Aerospace and Electronics Magazine*, vol. 15, pp. 28-32, 2000.

[3] K. R. Fowler, Electronic Instrument Design, Oxford University Press, New York, 1996.

[4] R. S. Sherratt, "Use of the LMS adaptive signal processing technique to improve signal data rates from practical oil well logging equipment," International Conference on Simulation, CPN 457, 1998.

[5] L. Feiner, "Power electronics transforms aircraft systems," pp. 166-171.

[6] P. Kundur, Power system stability and control, Mcgraw-Hill, Inc., New York, 1994.

[7] M. Belkhayat, R. Cooley, and A. Witulski, "Large signal stability criteria for distributed systems with constant power load," *Proceedings of Power Electronics Specialists Conference*, pp. 1333-1338, 1990.

[8] V. Rajasekaran, and B. S. Heck, "On stability enhancing control methods in power electronic converters," *Proceedings of Power Electronics Specialists Conference*, 2002.

[9] R. D. Middlebrook, "Design techniques to prevent input-filter oscillations in switched-mode converters," *Proceedings of Solid State Power Conversion*, pp. 1-16, 1978.

[10] Y. Jang, and R. E. Erickson, "Physical origins of input filter interactions," *IEEE Transactons on Power Electronics*, vol. 7, no. 4, pp. 725-733, 1992.

[11] B. H. Cho, J. R. Lee, and F. C. Lee, "Large signal stability of spacecraft power systems," *Proceedings of Power Electronics Specialists Conference*, pp. 289-294, 1987.

[12] M. Belkhayat, R. Cooley, and A. Witulski, "Large signal stability criteria for distributed systems with constant power loads," *Proceedings of Power Electronics Specialists Conference*, pp. 1333-1338, 1995.

[13] K. Schneider, C. Liu, T. McGinnis, B. Howe, H. Kirkham, " Real-time control and protection of the NEPTUNE power system,"

[14] B. M. Howe, H. Kirkham, and V. Vorperian, "Power system considerations for undersea observatories," IEEE Journal of Oceanic Engineering, vol. 27, no. 2, April 2002.

[15] C. W. Taylor, "Line drop compensation, high side voltage control, secondary voltage control – why not control a generator like a static var compensator," *Proceedings of IEEE Power Engineering Society Summer Meeting*, pp. 307-310, 2000.

[16] H. Kitamura, and J. Paserba, "Improvement of voltage stability by the advanced high side voltage control regulator," *Proceedings of IEEE Power Engineering Society Summer Meeting*, pp. 278-284, 2000. SMPS Technology Knowledge Base, Internet URL: www.smpstech.com/latch000.htm

[17] O. J. M. Smith, "Closer control of loops with dead-time," *Chem. Eng. Prog.*, vol. 53, no. 5, pp. 217-219, 1957.

[18] D. M. Schneider, "Control of processes with time delays," *IEEE Transactions on Industrial Applications*, vol. 24, no. 2, pp. 186-191, 1988.

[19] K. Ogata, Modern Control Engineering, 2nd edition, Prentice Hall, New Jersey, 1990.

[20] W. Zhang, and X. Xu, "Simple predictor for processes with time delay," *Proceedings of the American Control Conference*, pp. 822-826, 1999.

[21] J. F. Sifer, S. J. Prouty, and P. H. Mak, "Advanced concepts for launch vehicle control," *IEEE AES Magazine*, pp. 23-29, 1991.

[22] K. S. Rattan, and V. Feliu, "Feedforward control of flexible manipulators," *Proceedings of the IEEE International Conference on Robotics and Automation*, pp. 788-793, 1992.

[23] P. K. Khosla, and T. Kanade, "Experimental evaluation of nonlinear feedback and feed-forward control methods for manipulators," *International Journal of Robotics Research*, vol. 7, no. 1, 1988.

[24] D. G. Taylor and S. Li, "Feed-forward compensation of gantry robots with structural flexibilities," *Proceedings of the 7th Mechatronics Forum International Conference*, Atlanta, GA, September 2000.

[25] O. H. Schade, "Analysis of rectifier operation," *Proceedings of IRE*, pp. 344, vol. 31, 1943.

[26] R. Hernandez, US Patent No. 6,522,119. Power Source Regulator for Wireline Cable System. February 18, 2003.

[27] R. Achar, and M. Nakhla, "Simulation of high-speed interconnects," *Proceedings of the IEEE*, vol. 89, no. 5, pp.693-727, 2001.

[28] A. Dounavis, R. Achar, and M. Nakhla, "Passive closed loop transmission line model for general purpose circuit simulators," *IEEE Transactions on Microwave Theory*, vol. 47, pp. 2450-2459, 1999.

[29] M. Celik, A. C. Cangellaris, and A. Yaghmour, "An all purpose transmission line model for interconnect simulation in SPICE," *IEEE Transactions on Microwave Theory*, pp. 127-138, 1997.

[30] T. Yu and J. R. Marti, "A robust phase-coordinates frequency-dependent underground cable model for the EMTP," *IEEE Transactions on Power Delivery*, vol. 18, 2003.

[31] J. R. Marti, L. Marti, and H. W. Dommel, " Transmission line models for steady-state and transients analysis," *Proceedings of Athens PowerTech*, pp. 744-750, 1993.

[32] C. Dufour, H. Le-Huy, J. Soumagne, and A. Hakimi, "Real-time simulation of power transmission lines using Marti model with optimal fitting on dual-DSP card," *IEEE Transactions on Power Delivery*, vol. 11, no. 1, 1996.

[33] J. Vlach and K. Singhal, *Computer Methods for Circuit Analysis and Design*.

[34] SMPS Knowledge Technology Base, Internet URL: www.smpstech.com.

[35] P. Midya, "Linear switcher combination with novel feedback," *Proceedings of Power Electronics Specialists Conference*, pp. 1425-1429, 2000.

[36] T. Kailath, *Linear Systems*. Toronto: Prentice Hall, 1980.

[37] C. T. Chen, *Linear System Theory and Design*. New York: Holt, Rinehart and Winston, 1984

VITA

Vinod Rajasekaran was born on January 13, 1977 in Madras, India. He attended the Indian Institute of Technology, Madras and received his Bachelor of Technology degree in Electrical Engineering in May, 1998. He received the M. S. degree in Electrical Engineering in May 2000 from the Georgia Institute of Technology in Atlanta, Georgia. He worked as an Engineering Intern at Rockwell Collins Inc. on design and analysis of low voltage power supplies in the summers of 1999 and 2000.He was awarded the Ph. D. degree in Electrical Engineering in December 2003 from the Georgia Institute of Technology in Atlanta, Georgia. During the course of his Ph. D.,Vinod also interned for two semesters with Schlumberger, Inc. where he worked on power delivery to remote instrumentation. While at Georgia Tech, Vinod was employed as a Graduate Research Assistant and worked on impact of electric vehicles, modeling of DC power supplies and power delivery in systems with lossy cables.